UNIVERSIDADE
BEIRA INTERIOR

Aluminum-ion Structural Battery
Proof of Concept

Versão Final Após Defesa

Gonçalo Filipe Trindade da Silva

Dissertação para obtenção do Grau de Mestre em
Engenharia Aeronáutica
(mestrado integrado)

Orientador: Prof. Doutor João Pedro Nunes Pereira
Co-orientador: Prof. Doutor Abílio Manuel Pereira da Silva
Co-orientador: Prof. Doutor Thiago Assis Dutra

Covilhã, novembro 2023

Declaração de Integridade

Eu, Gonçalo Filipe Trindade da Silva, que abaixo assino, estudante com o número de inscrição a41198 de/o Mestrado Integrado em Engenharia Aeronáutica da Faculdade de Engenharia, declaro ter desenvolvido o presente trabalho e elaborado o presente texto em total consonância com o **Código de Integridades da Universidade da Beira Interior**.

Mais concretamente afirmo não ter incorrido em qualquer das variedades de Fraude Académica, e que aqui declaro conhecer, que em particular atendi à exigida referenciação de frases, extratos, imagens e outras formas de trabalho intelectual, e assumindo assim na íntegra as responsabilidades da autoria.

Universidade da Beira Interior, Covilhã, 20/11/2023.

Acknowledgements

I wish to express my profound gratitude to the numerous individuals and institutions whose unwavering support and contributions have been instrumental in the successful completion of this thesis. I am indebted to my esteemed thesis advisors, Prof. Doctor João Pedro Nunes Pereira, Prof. Doctor Abílio Manuel Pereira da Silva and Prof. Doctor Thiago Assis Dutra, for their exceptional guidance, mentorship, and scholarly insights. Their dedication and expertise have been invaluable throughout every stage of my research journey.

I extend my appreciation to the Department of Aerospace Science and Electromechanical Engineering for their support in providing access to essential resources and facilities crucial to the advancement of my research. I would like to acknowledge the unit research, C-MAST for funding my research experience and providing essential favilities. Furthermore I also want to thank Prof. Doctor José Álvaro Nunes Pombo for teaching me and allowing me to use equipment in the electrotechnical laboratory.

To my parents, my deepest gratitude for their unwavering love, encouragement, and understanding during the challenges and demands of my academic journey. Their support has been my cornerstone.

I extend my thanks to my friends for their friendship, encouragement, and the moments of respite they provided during times of academic rigor. Your camaraderie and belief in me have been a source of motivation, especially Sofia for always being there for me and Priscilla for helping me with my thesis.

In conclusion, this research endeavor would not have been possible without the collective contributions and support of these exceptional individuals and institutions. Each played a unique and vital role in shaping this thesis, and for that, I am truly thankful.

Thank you all for being an integral part of this academic journey.

Resumo

Esta dissertação tem por base o desenvolvimento bem-sucedido de uma bateria estrutural de alumínio, que aborda as crescentes preocupações com o aquecimento global e a poluição por meio da exploração de tecnologias mais sustentáveis, em particular veículos elétricos. As baterias estruturais surgiram como soluções potenciais para superar limitações como baixa autonomia e curta distância em veículos elétricos.

Uma revisão abrangente da literatura é conduzida para obter uma compreensão mais profunda desse sistema multifuncional e estabelecer uma base para comparação. Vários projetos de bateria são testados antes de finalizar o projeto escolhido. Descrições detalhadas passo a passo dos processos de fabricação são apresentadas, resultando na produção de várias amostras da bateria estrutural com dimensões de 100 mm por 100 mm.

A pesquisa começa com uma introdução aos componentes de bateria e suas especificações, fornecendo uma base para a seleção da química apropriada. Após analisar as três principais químicas (lítio, sódio e alumínio), uma análise qualitativa leva à escolha da química de alumínio devido ao seu custo mais baixo, maior segurança e amigabilidade ambiental. O reforço de fibra de carbono é selecionado com base no uso predominante de cátodos à base de carbono em baterias de alumínio.

Obteve-se um módulo de Young de $\approx$ 19.1 GPa e uma resistência à flexão de $\approx$ 247.5 MPa. Além disso, a bateria estrutural demonstrou suas capacidades funcionais ao iluminar com sucesso LEDs de cores diferentes, como vermelho, azul e verde. Para além disso revolou uma tensão máxima de 1.65 V e a capacidade de manter a tensão e a resistência interna quando sujeito a uma deflexão de 5 mm.

Esta pesquisa contribui para o avanço das tecnologias sustentáveis de armazenamento de energia e sua aplicação potencial em veículos elétricos. Os resultados destacam o desenvolvimento bem-sucedido de uma bateria estrutural de alumínio com propriedades mecânicas promissoras e desempenho funcional, abrindo caminho para explorações adicionais nesse campo.

Palavras-chave

Baterias de Alumínio, Baterias Estruturais, Sistemas Mutifuncionais, Compósitos de Carbono

Abstract

This thesis focuses on the successful development of an aluminum-ion structural battery, which addresses the growing concerns of global warming and pollution by exploring more sustainable technologies, particularly electric vehicles. Structural batteries have emerged as a potential solution to overcome limitations such as low range and short autonomy in electric vehicles.

The research begins with an introduction to battery components and their specifications, providing a foundation for selecting the appropriate chemistry. After analyzing the three main chemistries (lithium, sodium, and aluminum), a qualitative analysis leads to the selection of aluminum chemistry due to its lower cost, higher safety, and environmental friendliness. Carbon fiber reinforcement is chosen based on the prevalent use of carbon-based cathodes in aluminum-ion batteries.

A comprehensive literature review is conducted to gain a deeper understanding of this multifunctional system and establish a basis for comparison. Several battery designs are tested before finalizing the chosen design. Detailed step-by-step descriptions of the manufacturing processes are presented, resulting in the production of various samples of the structural battery measuring 100 mm by 100 mm.

The achieved results demonstrate a Young's modulus of $\approx$ 19.1 GPa and a flexural strength of $\approx$ 247.5 MPa. Additionally, the structural battery showcased its functional capabilities by successfully illuminating different colored LEDs such as red, blue and green. Furthermore it achieved a max voltage of 1.65 V, and the capability of having constant voltage and internal resistance under a 5 mm deflection.

This research contributes to the advancement of sustainable energy storage technologies and their potential application in electric vehicles. The findings highlight the successful development of an aluminum-ion structural battery with promising mechanical properties and functional performance, paving the way for further exploration in this field.

Keywords

Aluminum-ion Battery, Structural Battery, Multifunctional Systems, Carbon Fiber Reinforced Polymer

Contents

List of Figures

List of Tables

Acronyms and Abbreviations

AAB	Aluminum-Air Battery
ABS	Acrylonitrile Butadiene Styrene
ACARE	Advisory Council for Aviation Research and innovation in Europe
AIB	Aluminum-Ion Battery
AIBN	2,2′-Azobis(2-Methylpropionitrile)
ALMO	$Al_{2/3}Li_{1/3}Mn_2O_4$
ARL	Army Research Laboratory
AISB	Aluminum-Ion Structural Battery
BN	Boron Nitride
BANFs	Branched Aramid NanoFibers
CATL	Contemporary Amperex Technology Limited
CC	Carbon Cloth
CF	Carbon Fiber
CFRP	Carbon Fiber Reinforced Polymer
CMC	Carboxymethyl Cellulose
CNF	Carbon Nanofibers
CNT	Carbon Nanotube
CSC	Carbon Nanotubes-Stringed Metal Sulfides Superstructure
DMF	N,N-Dimethylformamide
E2BADMA	Bisphenol A Ethoxylate Dimethacrylate
EMIMBF4	1-Ethyl-3-Methylimidazolium Tetrafluoroborate
EO	Modified Polyethylene Oxide
EU	European Union
eVTOL	Electric Vertical Take-off and Landing
FLG	Few Layer Graphene
FRP	Fiber Reinforced Polymer
G	Graphene
GDE	Gas Diffusion Electrodes
GF	Graphene Fiber
GHG	Greenhouse Gas Emissions
Gi	Graphite
GMG	Graphene Manufacturing Group
IEA	International Energy Agency
IL	Ionic Liquid
LCA	Lice Cycle Assessment
LCO	Lithium Cobalt Oxide
LFP	Lithium Iron Phosphate
LIB	Lithium-Ion Battery

Acronyms and Abbreviations - Continuation

LiPS	Lithium PolySulfide
LiTFSI	Lithium Bis(Trifluoromethanesulfonyl)imide
LMO	Lithium Manganese Oxide
LTO	Lithium Titanate
MCMB	Mesocarbon Microbeads
MIT	Massachusetts Institute of Technology
MNC	Mesoporous Nitrogen-Containing Carbon
N/D	No Data
NASA	National Aeronautics and Space Administration
NCA	Nickel Cobalt Aluminum Oxide
NCM	Layered Lithium Nickel Cobalt Manganese Oxide
NCNT	N-doped Carbon Nanotube
ND	NanoDice
NHE	Normal Hydrogen Electrode
NIMS	National Institute for Materials Science
NMC	Nickel Manganese Cobalt Oxide
NMP	N-Methylpyrrolidone
NPC	Nitrogen-doped Porous Carbon-fiber
NVP	$Na_3V_2(PO_4)_3$
NVPF	$Na_3V_2(PO_4)_2F_3$
NVPOF	$Na_3V_2(PO_4)_2O_2F$
P(VDF-HFP)	Poly(Vinylidene Fluoride-co-Hexafluoropropylene)
PAN	Polyacrylonitrile
PEGDA	Poly(Ethylene Oxide) Diacrylate
PEGDMA	Poly(Ethylene Glycol) Dimethacrylate
PEO	Poly(Ethyleneoxide)
PLI	Polymer-Lithium Ion
PVA-KOH	Potassium Hydroxide–Poly(Vinyl Alcohol)
PVC	Polyvinyl Chloride
PVDF	Poly(Vinylindene Fluoride)
rGO	Reduced Graphene Oxide
SA	Sodium Alginate
SB	Structural Battery
SBE	Structural Battery Electrolyte
SBR	Styrene-Butadiene Rubber
SEM	Scanning Electron Microscope
SHE	Standard Hydrogen Electrode
SIB	Sodium-Ion Battery

Acronyms and Abbreviations - Continuation

UAV	Unmanned Aerial Vehicle
UBI	Universidade da Beira Interior
US	United States
VOC	Volatile Organic Compounds
[EMIM]Cl	1-Ethyl-3-Methylimidazolium Chloride
[BMIM]Cl	1-Butyl-3-Methylimidazolium Chloride

Symbols

Chemical Symbols

Al	Aluminum
AL_2O_3	Aluminum Oxide
$Al(OH)_3$	Aluminum Hydroxide
$AlCl_3$	Aluminum Chloride
C	Carbon
CH_4	Methane
CO_2	Carbon Dioxide
Co	Cobalt
CoO	Cobalt Oxide
CoNi	Cobalt-Nickle
$CoSe_2$	Cobalt Diselenide
Cu	Copper
CuS	Copper Sulfide
F	Fluorine
Fe	Iron
FeF_2	Iron(II) Fluoride
FeF_3	Ferric Fluoride
FeS_2	Iron Disulfide
H	Hydrogen
Li	Lithium
Li_2S	Dilithium Sulfide
$LiBF_4$	Lithium Tetrafluoroborate
LiCl	Lithium Chloride
$LiCoO_2$	Lithium Cobalt(III) Oxide
$LiF_2BC_2O_4$	Lithium Difluoro(Oxalato)Borate
$LiFePO_4$	Lithium Iron Phosphate
$LiMnO_2$	Lithium Manganese Dioxide
$LiMnPO_4$	Lithium Manganese(II) Phosphate
$LiNi_{0.8}Co_{0.15}Al_{0.05}O_2$	Lithium Nickel Cobalt Aluminum Oxide
$LiNiO_2$	Lithium Nickel Oxide
$LiPF_6$	Lithium Hexafluorophosphate
Mn	Manganese
MnO_2	Manganese Dioxide
$MnSO_4$	Manganese Sulfate
Mo	Molybdenum

Chemical Symbols - Continuation

MoO_2	Molybdenum Dioxide
N	Nitrogen
N_2O	Nitrous Oxide
Na	Sodium
$Na_3V_2(PO_4)_3$	Trisodium Divanadium(III) Tris(Orthophosphate)
Ni	Nickel
NiCad	Nickel-Cadmium
NiS	Nickel Sulfide
NiS_2	Nickel Disulfide
NOx	Nitrogen Oxides
O	Oxygen
P	Phosphorus
Pd	Palladium
Ge	Germanium
S	Sulfur
Sb	Antimony
Se	Selenium
Sn	Tin
SnS_2	Tin Sulfide
$SnSe_2$	Stannic Selenide
TiO_2	Titanium Dioxide
V	Vanadium
VO_2	Vanadium Dioxide
V_2O_5	Vanadium Oxide
W	Tungsten
WS_2	Tungsten Disulfide
Zn	Zinc
$Zn(CF_3SO_3)_2$	Zinc Trifluoromethanesulfonate
$ZnSO_4$	Zinc Sulfate

Other Symbols

Latin Symbols - SI Units

A	Cross-sectional Area	m^2
b	Width	m
d	Deflection	m
E	Young's Modulus	Pa
e	Electron	$-$
h	Height	m
Ir	Current through resistor	A
L	Span	m
m	Mass	kg
n	Number (of)	$-$
P_{max}	Maximum Load	N
Q	Generic Chemical Element	$-$
Ri	Internal Resistance	Ω
t	Slope of the tangent to the initial-line portion of the load-deflection curve	$-$
Vr	Voltage drop across resistor	V

Greek Symbols

ε	Elongation
σ	Tensile Strength
Ω	Ohm

Subscript Symbols

c	Compression/Compressive
CF	Carbon Fiber
LIB	Lithium-Ion Battery
GF	Glass Fiber
SB	Structural Battery

Chapter 1

Introduction

This chapter will present the thesis's focus and scope, with a primary emphasis on the need to transition from combustion-powered vehicles, such as cars, buses, and aircraft, to electric vehicles, and identifying an alternative power source for the latter, with a specific focus on the aeronautic industry. The work objectives will also be outlined, clarifying the focus of each chapter.

1.1 Thesis Focus and Scope

Global warming is currently a major concern for the general public, as the effects of this phenomenon have become increasingly felt in recent years, ranging from extreme heat causing droughts and fires to extreme cold causing numerous deaths and floods worldwide. In response, many governments have implemented measures to mitigate global warming, such as the European Union's (EU) efforts to reduce greenhouse gas emissions (GHG) by at least 55 % by 2030 and achieve climate neutrality by 2050 [1], and the seventeen goals implemented by the United Nations to 2030 for a sustainable development [2].

Carbon dioxide (CO_2), methane (CH_4), nitrous oxide (N_2O), and fluorinated gases are the five major greenhouse gases, with carbon dioxide accounting for 74.4 % of greenhouse gas emissions [3]. Furthermore, the International Energy Agency (IEA) reports that the transport sector alone accounts for 24 % of direct CO_2 emissions from fuel combustion, and projections show that this figure is expected to increase in the coming decades [4, 5]. As a result, to decarbonize the transport sector there needs to be a shift towards electric vehicles. The automotive industry has begun to make this transition, with several major car brands, including Jaguar, Bentley, Mini, and Volvo [6] planning to phase out combustion engines in favor of electric vehicles in the near future.

However, this shift has yet to occur in the aeronautical sector, despite the global demand for air transport increasing at an annual rate of 5 % since 2019, with 151 thousand daily operated flights in 2021 [7, 8]. While this generates economic opportunities for the aeronautical sector, it also aggravates the dependence on fossil fuels, leading to an increase in greenhouse gas and air pollutant emissions, with aviation projected to account for 11 % of global CO_2 emissions in the next two decades [7]. To address this challenge, strategies aimed specifically at the aeronautical sector have been developed, such as the EU ACARE flightpath 2050 strategy [9]. The goals of this strategy are presented in **Table 1.1**.

Table 1.1: Summary of EU ACARE flightpath 2050 strategy.

Environmental factor	EU ACARE flightpath 2050 strategy. (Up to 2050)
Greenhouse gas emissions (GHG)	75 % reduction in CO2 emissions
Nitrogen oxides (NOx)	90 % NOx emissions reduction
Life cycle	Air vehicles are designed and manufactured to be recyclable
Noise	65 % reduction

The transition from conventional aircraft to electric aircraft is a complex undertaking, but it can be achieved with the development of new technology that can overcome the limitations of battery specific energy. Kerosene, the most widely used fuel for aircraft propulsion, boasts a remarkable specific energy of approximately 43 MJ/kg or 12 000 Wh/kg [10]. In contrast, even the best battery cells have a substantially lower specific energy, such as the 500 Wh/kg solid-state cell created by NASA [11] and the 466 Wh/kg lithium-air cell developed by Japan's National Institute for Materials Science (NIMS) [12, 13]. These figures reveal that to achieve a range and endurance comparable to that of conventional aircraft, electric aircraft would require 24 times the mass of batteries relative to kerosene.

The use of batteries as an energy source in electric aircraft results in a significant increase in aircraft weight, necessitating additional space for battery storage. This weight increase has a direct impact on the structural integrity, mass distribution, and aerodynamic efficiency of the aircraft. Moreover, the increase in weight demands more powerful motors that require a corresponding increase in energy availability, which can only be achieved by incorporating more batteries, creating a cycle of challenges.

In spite of the challenges, some aviation companies have initiated projects to develop electric planes or eVTOL urban vehicles. Airbus is one such company, with its eVTOL project [14], and Extra in collaboration with Siemens, who created an electric aerobatic plane [15]. However, the limitations of current battery technology continue to pose significant challenges for these projects, with restricted range and endurance remaining a significant issue.

To overcome these challenges, more efficient and safer batteries must be developed. One potential solution is the use of multifunctional systems and materials. Multifunctional systems and materials, as defined by Thomas et al. [16], are structural configurations and materials that can perform multiple primary functions at the same time. One such multifunctional system that has gained significant attention in recent years is the structural energy storage system. This system includes supercapacitors and batteries that are integrated into the vehicle's structure, or others. The integration of electrical energy storage in structural load paths has been shown to offer significant mass savings for cars, aircraft, and consumer electronics as reported in the literature [17–19]. **Figure 1.1** depicts an overview of some of the batteries that will be covered in the state-of-the-art section.

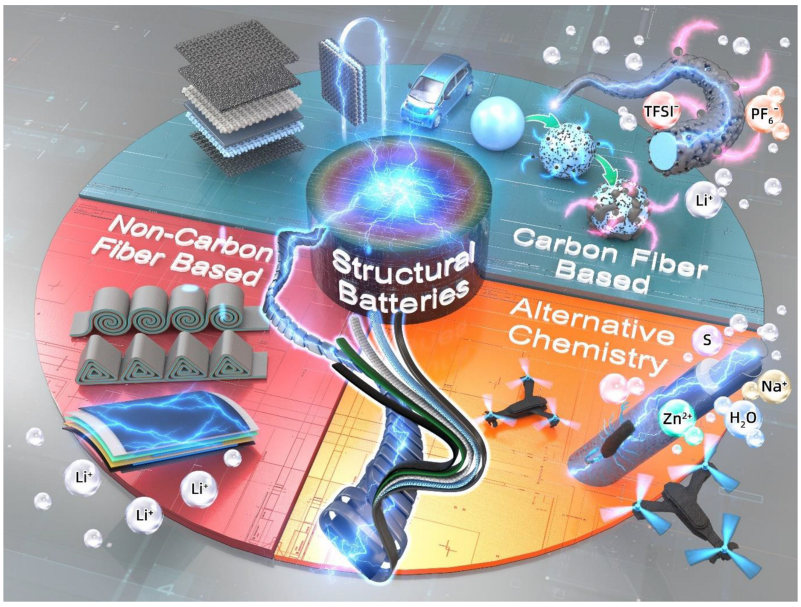

Figure 1.1: A diagram depicting the three major classifications of structural battery composites found in the literature: carbon-fiber based, non-carbon-fiber based, and structural batteries using chemistries other than Li-ion. Reproduced from [20].

The utilization of structural batteries (SB), characterized by increased weight savings and reduced battery storage space requirements, has the potential to overcome the obstacles hindering the development of efficient electric aircraft capable of performing missions equivalent to those of conventional aircraft.

1.2 Objectives

In this thesis, the focus is on the development and analysis of an aluminum-ion structural battery (AISB) and its application to high-load structural components such as the fuselage or wing panels of an aircraft. During the course of this work, no such SB has been reported in the literature. The electrochemical and mechanical performance of the battery will be analyzed. The main objectives of this work are summarized as follows:

- To present the measures that have been taken to mitigate global warming, the need to shift from fossil fuel-powered aircraft to electric aircraft, and how multifunctional systems can help address some of the challenges hindering this transition.
- To define a battery and its main components, such as electrodes, electrolytes, and separators, and to explain their roles in a battery's performance and function.
- To identify the different types of materials used in batteries, their operating differences, advantages, and disadvantages.

- To review previous works on the analysis of structural batteries, and the processes used in their construction and performance analysis.
- To explain the material choice for the development of the aluminum-ion structural battery and the electrochemical and mechanical performance analysis performed.
- To calculate the electrochemical, mechanical, and multifunctional performance of the developed battery.
- To compare and discuss the results obtained with similar works in the field.

1.3 Structure of the Thesis

This thesis consists of five chapters, each of which presents a structured and comprehensive overview of the information contained therein.

The focus and scope of the thesis are introduced in **Chapter 1**, emphasizing the need for new technology in the aeronautical sector. The study's objectives are clearly defined, and the structure of the thesis is outlined.

Chapter 2 provides a comprehensive review of relevant studies related to the thesis's theme. The work's state of the art is established, as are the theoretical and practical scientific foundations that support it. The concept of a battery is introduced, along with a brief overview of its components and specifications. Following that, various types of batteries are discussed, including their materials, advantages and disadvantages of using such materials. In the end, a review of previous work on SBs, manufacturing techniques, and results is presented.

Chapter 3 of this thesis is dedicated to the presentation and analysis of the materials chosen for the construction of the SB. Additionally, the experimental setup and methods for fabricating the SB are also discussed and presented. The methods employed for battery's mechanical and electrochemical characterization are also described in detail.

The study's findings are presented, analyzed, and compared to previous works in **Chapter 4**.

Lastly, in **Chapter 5**, the main conclusions related to the SB are presented, and their potential application in the aeronautical sector is explored. The chapter concludes with a discussion of future work and research possibilities.

Chapter 2

State-of-the-Art

This chapter presents a comprehensive literature review of relevant studies related to the thesis's theme. To facilitate understanding of the experimental results, a concise and clear explanation of the key components of a battery and their relevant specifications is provided first. Following that, a detailed examination of various types of batteries is presented encompassing the materials utilized for cathodes or anodes, the underlying chemical reactions, and the associated benefits and drawbacks. Lastly, a review of previous works on structural batteries, their manufacturing techniques, and the results obtained is presented, offering a thorough examination of the current state of the field.

2.1 Battery Components and Fundamental Concepts

Humanity's demand for energy is increasing on a daily basis, and the majority of the energy consumed, 80 %, is currently derived from fossil fuels. Nuclear energy generates a small portion of energy, 18 %, while only a negligible amount, 2 %, is generated from clean energy sources, primarily batteries [21].

A battery is a type of electrical device that converts chemical energy into electrical energy via an electrochemical reaction. A battery can consist of one or multiple cells, but each cell has two electrodes, a negative electrode, *i. e.* **Anode** and a positive electrode *i. e.* **Cathode**, immersed in an electrolyte solution that allows the flow of ions between the electrodes. The cathode and anode must be physically separated to prevent short-circuiting.

When a load is connected across the electrodes, the flow of ions through the electrolyte results in the flow of electrons, producing an electrical current that can be used to power devices or charge other batteries. In batteries, current collectors exist to facilitate the flow of electrical current from the electrodes to the external circuit. **Figure 2.1** depicts a schematic of a battery with all the components mentioned above.

Alessandro Volta, an Italian physicist, invented the first recognized battery in 1790. Volta's design consisted of copper (Cu) and zinc (Zn) discs stacked on top of one another and separated by a brine-soaked cloth, example of the battery in **Figure 2.2**. Each cell was composed of a Cu and a Zn disc, and the brine produced a voltage of 0.76 V [23]. In this design, the zinc acted as the anode, the copper as the cathode, the cloth as the separator, and the brine as the electrolyte.

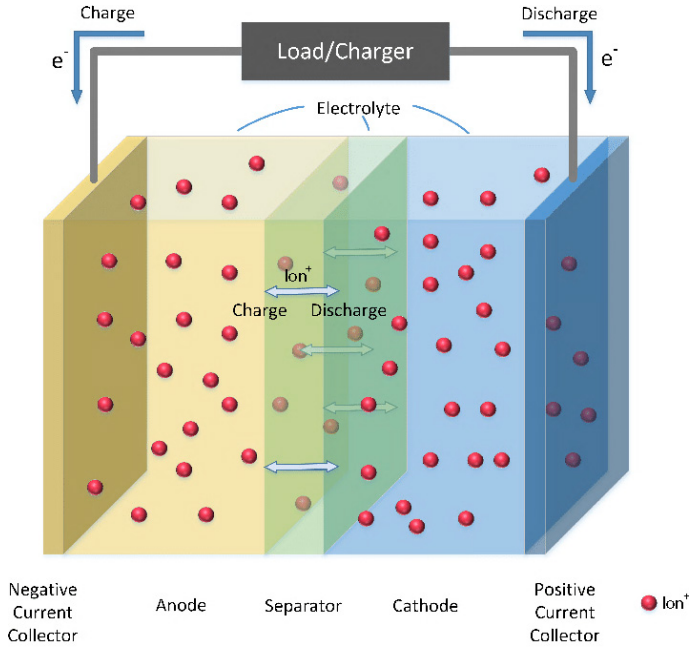

Figure 2.1: A schematic of a battery and its components, as well as the flow of electrons during charge and discharge. Adapted from [22].

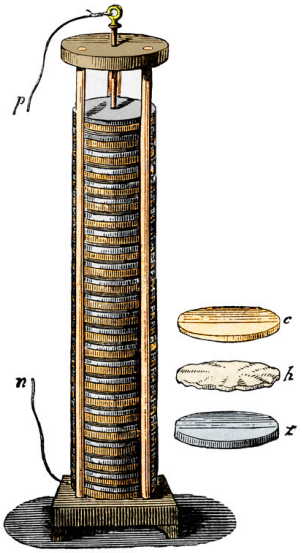

Figure 2.2: Volta's battery is depicted as a drawing, with the discs made of Cu and Zn. Reproduced from [24].

2.1.1 Anode

The anode in a battery serves as the negative or reducing electrode, where oxidation occurs during discharge. Throughout this process, electrons are released and flow through an external circuit to the cathode, which serves as the positive or oxidizing electrode, where reduction occurs through electron gain. In contrast, the anode recovers electrons during

the charging process, resulting in the opposite reaction.

For the anode to effectively contribute to the battery's overall performance, it must possess several key characteristics [25]:

- It must have good conductivity.
- It must have a low reduction potential, meaning that it must be easily oxidized (it must readily release electrons).
- It must be chemically stable.
- It must have high coulombic output.
- It must have the ability to undergo an oxidation-reduction reaction with the cathode.

Equation 2.1 illustrates the oxidation reaction that takes place at the anode during battery discharge, where Q represents the element utilized in the anode, and n denotes the number of electrons transferred.

$$\text{Anode(oxidation):} \quad Q \rightarrow Q^{n+} + ne^{-} \quad (2.1)$$

The most commonly used materials for the anode are Graphite (Gi) and Lithium Titanate (LTO).

2.1.2 Cathode

The cathode of a battery functions as the positive or oxidizing electrode, where electron gain causes reduction. It is the recipient of electrons that are transferred from the anode via an external circuit.

In order to effectively contribute to the overall performance of the battery, the cathode must have several key characteristics [25]:

- It must have good conductivity.
- It must have a high reduction potential, meaning that it must be easily reduced.
- It must be chemically stable.
- It must have the ability to undergo an oxidation-reduction reaction with the anode.

Equation 2.2 depicts the reduction reaction that transpires at the cathode during battery discharge. In this equation, Q represents the element used in the cathode, and n symbolizes the number of electrons involved in the transfer.

$$\text{Cathode(reduction):} \quad Q^{n+} + ne^- \rightarrow Q \quad (2.2)$$

The most commonly used cathode materials are lithium cobalt oxide (LCO), lithium manganese oxide (LMO), nickel manganese cobalt oxide (NMC), nickel cobalt aluminum oxide (NCA) and lithium iron phosphate (LFP).

The performance of commonly utilized cathode and anode materials is depicted in **Figure 2.3**. In terms of anode materials, Gi stands out for its high energy density and costs/Ah, but it comes with reduced safety. On the other hand, LTO performs well overall but has a lower energy density.

Switching to cathode materials, NCA leads in both energy and power density but suffers from safety concerns. In contrast, LFP excels overall but has the lowest energy density performance.

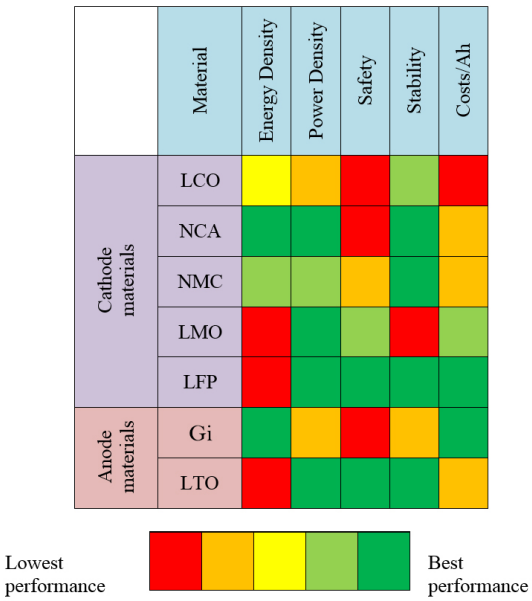

Figure 2.3: The performance of commonly used anode and cathode materials varies significantly. In terms of anodes, graphite stands out as it provides the highest specific energy, while for cathodes, nickel cobalt aluminum oxide takes the lead. Reproduced from [26].

2.1.3 Separator

The separator is another important component. In a battery, the separator acts as a barrier between the anode and cathode, preventing direct contact while still allowing ion flow. Furthermore it also aids in the stability of the battery and the prevention of short circuits.

For a battery to work effectively, the separator must have the following characteristics [27]:

- It must be permeable only to ions, which means that only ions and not electrons can pass through (electrically insulating).
- It must have some porosity in order to contain the electrolyte while allowing the ions to pass through.
- It must be chemically stable against the electrolyte and electrode materials under the highly reactive environments when the battery is fully charged.
- It should be thin enough to support the battery's specific energy and power while also being strong enough to keep the battery stable and prevent short circuits.

Depending on the type of battery, commonly employed separators include microporous membranes made from polyolefin or glass fiber filter paper [28].

2.1.4 Electrolyte

The battery's electrolyte is the final and most crucial component to discuss. The electrolyte is the medium that allows ions to flow between the anode and cathode. The ion transport through the electrolyte allows the battery to produce a flow of electrons through an external circuit, resulting in current.

The electrolyte in a battery must have the following properties [25] in order for it to function:

- It must have strong ion conductivity.
- It must be electronically insulating, which means that electrons cannot pass through it and cause a short circuit.
- It mustn't react with the materials of the electrodes.
- It must not lose its properties as a result of temperature changes.
- It must be chemically stable and not break down over time.

Electrolytes can be classified into two types: liquid electrolytes and solid electrolytes.

Liquid electrolytes contain dissolved salts, acids, or alkalies that are required for ionic conduction in a liquid solution such as water or another solvent, like 1-ethyl-3-methylimidazole chloride ([EMIM]Cl) or Urea [29].

Solid electrolytes, on the other hand, are solid materials that conduct ions. Solid electrolytes have gained popularity in recent years because, when compared to liquid electrolytes, they allow for batteries with higher energy and power density and better thermal stability [30]. Better thermal stability will result in safer batteries [31]. Furthermore, solid state batteries do not require a separator because the solid electrolyte acts as a it.

In **Figure 2.4** the difference between a conventional battery with a liquid electrolyte and a solid state battery with a solid electrolyte is depicted.

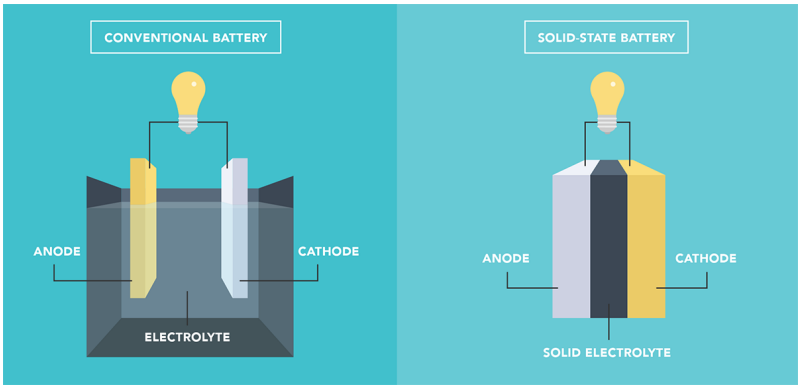

Figure 2.4: Representation of a conventional battery with a liquid electrolyte and a solid state battery with a solid electrolyte. Reproduced from [32].

2.1.5 General Concepts

To improve understanding of the topics that will be presented and the results obtained from the experimental section, we will introduce various specifications and terminologies commonly used in the description of batteries in this subsection [33, 34].

Battery Basics:

- **C- and E- rates** - The concept of C-rate is used in the context of batteries to normalize the discharge current of a battery, given that battery capacity tends to vary between different battery models. The C-rate represents the rate at which a battery is discharged relative to its maximum capacity. For instance, a 1 C rate signifies that the discharge current will discharge the entire battery in one hour. For a battery with a capacity of 50 Ah, if it is discharged at a constant rate of 50 A, it would take one hour to use up all its energy. A discharge rate of 2 C means that the battery will be discharged at a rate twice as fast, requiring only 30 minutes to deplete the battery's full capacity, with a discharge rate of 100 A, which is double the rate of 1 C. In contrast, E-rate is a related concept that represents discharge power, the same battery with 50 Ah of capacity, at a 10 C rate would discharge at a constant power output of 500 watts in 6 minutes
- **Secondary and Primary Batteries** – A primary battery is a non-rechargeable battery. A rechargeable secondary battery is one that can be used again and again.

Battery Technical Specifications:

- **Nominal Voltage** – The battery's reported or reference voltage.

- **Cut-off Voltage** – The minimum allowable voltage, also known as the empty state of the battery, serves as a defining parameter for a battery's capacity.

- **Capacity Retention (for a specific C-rate)** - Capacity retention is a fundamental parameter that refers to the ability of a battery to sustain its original capacity over time and usage, which is a measure of how well a battery can store and discharge energy compared to its initial state. It is worth noting that battery capacity naturally degrades due to chemical reactions and physical changes within the battery's components as a result of repeated charging and discharging cycles, the higher the C-rate the faster the degradation. Therefore, the capacity retention rate of a battery is a crucial factor to consider when evaluating its performance and lifespan.

- **Capacity or Nominal Capacity [Ah] (for a specific C-rate)** - The nominal capacity refers to the total amount of Ah that can be obtained upon discharging a battery at a specific discharge current, expressed in terms of C-rate, from a fully charged state to a defined cut-off voltage. This capacity can be calculated by multiplying the discharge current, by the discharge time, normally in hours, and it decreases as the C-rate increases.

- **Specific Current [A/g] (for a specific C-rate)** - Specific current, also known as normalized current, is an important battery performance parameter. This metric describes the rate at which electrical charge, A, is transferred through the battery per unit mass of battery. The specific current of a battery is an important indicator of its ability to deliver power efficiently and effectively over time. A high specific current can cause rapid capacity loss or degradation, resulting in a decrease in battery performance and lifespan.

- **Specific Capacity [mAh/g]** -The specific capacity of a battery, also known as gravimetric capacity, is a crucial parameter for assessing battery performance, representing the total amount of electrical charge that can be stored in a given mass of the battery. It indicates how long a battery-powered device can operate before requiring a recharge or replacement. Thus, gravimetric capacity serves as a key factor for determining the battery's suitability for a given application.

- **Capacity Density [mAh/cm^3]** - The capacity density of a battery, also referred to as volumetric capacity, is a crucial metric for assessing battery performance, representing the total amount of electrical charge that can be stored in a given volume of the battery. This metric, like specific capacity, determines the duration for which a battery-powered device can function before requiring a recharge or replacement.

- **Energy or Nominal Energy [Wh] (for a specific C-rate)** - The "energy capacity" of a battery is defined as the total number of Watt-hours available during discharge, where the discharge current is specified as a C-rate and the discharge process begins with a full charge and ends at the cut-off voltage. The energy capacity is

calculated by multiplying the discharge power by the discharge time, commonly in hours. As C-rate increases, energy, like capacity, decreases.

- **Specific Energy [Wh/kg]** - The nominal energy per unit mass of the battery, commonly referred to as the gravimetric energy density, is an important feature of the battery's chemistry and packaging. This value, in conjunction with the energy consumption of the vehicle, determines the mass of the battery required to achieve a desired range.

- **Specific Power [W/kg]** - Specific power, or the maximum achievable power per unit mass, is a distinctive feature of battery chemistry and packaging. This characteristic determines the mass of the battery required to meet a specific performance goal.

- **Energy Density [Wh/L]** - The nominal battery energy per unit volume, also known as the volumetric energy density. It is similar to specific energy, but it allows us to know the battery size required to attain the desired range.

- **Power Density [W/L]** - The maximum available power per unit volume. It's similar to specific power, but it refers to how big of a battery is needed to achieve a certain level of performance.

2.2 Types of Batteries

In this section, the distinction between various battery types will be based primarily on two key factors: rechargeability and the materials used. A battery's rechargeability refers to its ability to be recharged and used again after being discharged. The materials and chemical reactions involved, on the other hand, determine the amount of electrical energy that can be stored in a battery and the rate at which it can be released.

The study of these two factors will provide a thorough understanding of the various types of batteries and their distinct characteristics, which are critical for selecting the best battery for a specific application. This distinction is depicted in **Figure 2.5**, which serves as a visual representation of the division between the different types of batteries based on rechargeability and the materials used.

2.2.1 Rechargeability

With regards to rechargeability, as previously noted in **Section 2.1.5**, batteries can be classified as primary or secondary batteries. A battery's rechargeability is an important factor that influences its performance and efficiency.

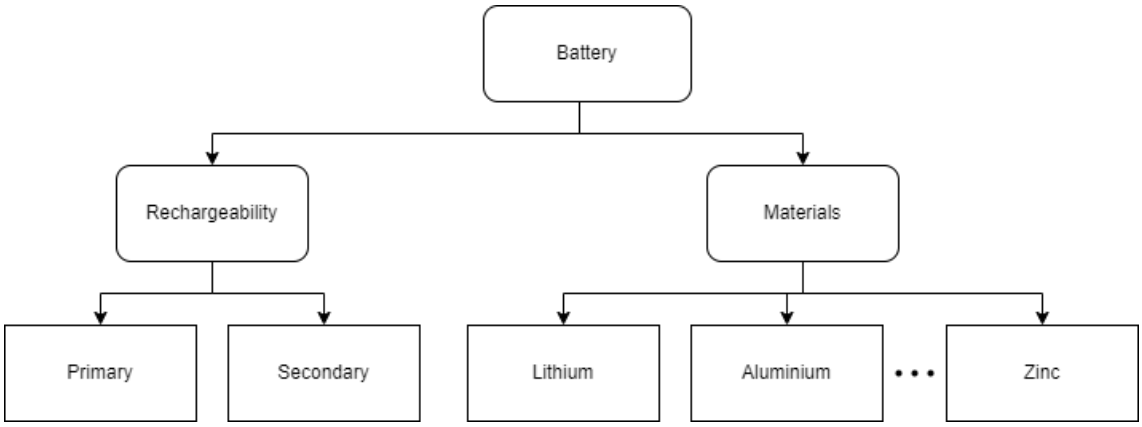

Figure 2.5: Diagram with the division of the batteries based on the rechargeability and materials used.

2.2.1.1 Primary Batteries

Primary batteries, also known as non-rechargeable batteries, can only be used once because the chemical reaction inside them produces a flow of electrons and electric energy until the reaction is completely exhausted, rendering the reaction irreversible.

Zinc-carbon and alkaline batteries are examples of primary batteries [35]. These batteries have both advantages and disadvantages, which are detailed in [36] and [37].

Advantages of Primary Batteries:

- They are user-friendly and do not require recharging.
- They have a low self-discharge rate, which means they can be stored for an extended period of time without losing energy.
- They are cost-effective.
- They possess higher energy capacity than secondary batteries.

Disadvantages of Primary Batteries:

- In the long run, they can be more expensive due to their disposable nature.
- Their one-time use makes them environmentally unfavorable.
- Their C-rate is relatively low.

2.2.1.2 Secondary Batteries

Secondary batteries, also known as rechargeable batteries, are distinguished by their ability to be used repeatedly due to the reversibility of the chemical reaction that occurs within.

The reaction can be reversed by applying an electrical charge to the battery, allowing it to be recharged and used again.

Secondary batteries include lithium-ion (Li-ion), nickel-cadmium (NiCad), and aluminum-ion batteries (Al-ion) [35]. Secondary batteries, like primary batteries, have their own set of advantages and disadvantages [38, 39].

Advantages of Secondary Batteries:

- Cost-effective over time as they can be recharged and utilized multiple times.
- Environmentally sustainable as they can be reused multiple times.
- They have a higher power density than primary batteries.
- Their C-rate is very high.

Disadvantages of Secondary Batteries:

- Lower gravimetric energy density compared to primary batteries.
- High self-discharge rate, resulting in a shorter storage life compared to primary batteries.
- Higher upfront costs.

2.2.2 Materials

There are numerous battery types that are differentiated based on the materials utilized in their construction [35, 40].This section will concentrate on three main battery types: lithium, aluminum, and sodium.

Lithium-ion batteries (LIBs) deserve attention because they are widely used in the field of electric vehicles due to their higher gravimetric energy density when compared to other batteries. A comparison of the gravimetric energy density of various battery types is portrayed in **Figure 2.6**. The study of LIBs is critical for understanding the current state-of-the-art in energy storage and serves as a foundation for evaluating new and emerging battery technologies.

Aluminum batteries and sodium-ion batteries (SIBs) have received significant attention in recent years as promising alternatives to LIBs, prompting companies such as Graphene Manufacturing Group (GMG) [42] and Contemporary Amperex Technology Limited (CATL) [43] to invest in their development. The introduction of these newer battery types has the potential to have a significant impact on the field of energy storage and to provide innovative solutions for energy storage requirements. Given the importance of this subject, a thorough examination of aluminum batteries and SIBs is required.

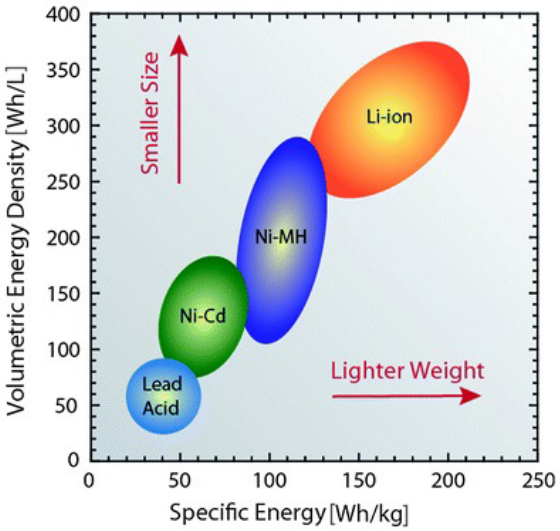

Figure 2.6: Comparison of the gravimetric and volumetric energy of different batteries. Adapted from [41].

Although there are other alternatives to LIBs such as zinc-air batteries and magnesium batteries, they will not be discussed here due to their less extensive research compared to the others. Besides that, zinc is not very abundant on Earth's crust, with only 0.0078 % availability, which is similar to that of lithium.

2.2.2.1 Lithium Batteries

As mentioned previously because of their high specific energy when compared to other available batteries, LIBs are one of the most widely used power sources for electric vehicles.

The positive electrode of LIBs is composed of various materials, including transitional metal oxides ($LiCoO_2$, $LiNiO_2$, $LiNi_{0.8}Co_{0.15}Al_{0.05}O_2$, $LiMnO_2$), polyanion compounds ($LiFePO_4$, $LiMnPO_4$), fluorine and chlorine compounds (FeF_3, FeF_2,LiCl), sulfur and lithium sulfide(S, Li_2S), and even more [44].

Furthermore, the negative electrode of LIBs can be made of carbonaceous materials, lithium titanium oxide or others [44]. An electrolyte and separator complete the battery's structure. However, the theoretical gravimetric energy density of LIBs is limited to a range of 380-460 Wh/kg [45], which is insufficient to meet all of the energy requirements of electric vehicles. To address this limitation, several new alternatives to LIBs have emerged, including lithium-air, Li-S, Li-CuF_2, Li-FeF_3, and more, all with a theoretical gravimetric energy density exceeding 1 000 Wh/kg [46].

Nevertheless, the safety concerns associated with LIBs are considerable due to the flammability of their electrolyte. What's more, rising demand for lithium, combined with scarcity and the negative environmental impact of its extraction [47, 48], has resulted in a signifi-

cant increase in its price, as shown in **Figure 2.7**. As a result, in recent years, alternative battery technologies that are both safe and environmentally sustainable, such as SIBs and aluminum batteries, have garnered attention.

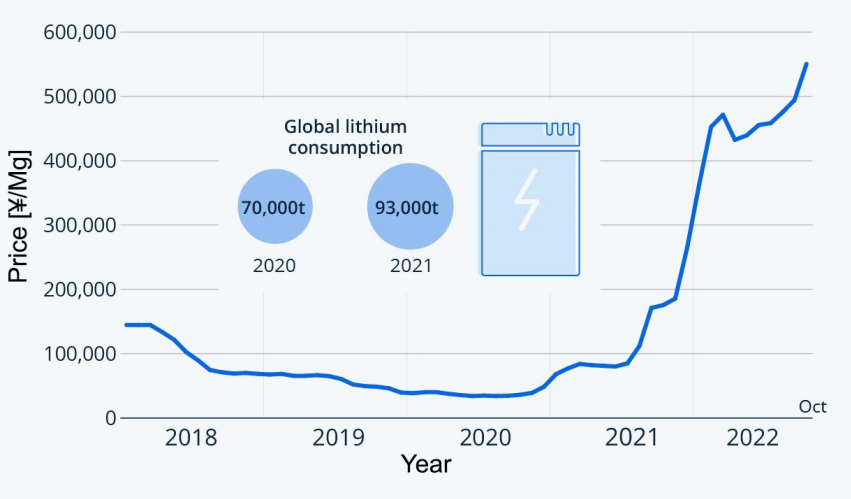

Figure 2.7: Monthly average price of lithium carbonate traded in china from Jan 2018 to Oct 2022. Adapted from [49].

Table 2.1 serves as a comprehensive summary of the alternative options to LIBs that have been previously discussed. The first battery included is a typical commercial LIB, with the practical specific energy represented by the market average of current LIBs. The following battery (Li//S), is a Li-S battery with one of the highest theoretical specific energy values among the examples in **Table 2.1**. In practice, however, this value has yet to be realized.

The third battery (Li//$Fe_{0.9}Co_{0.1}OF$) in **Table 2.1** is a Li-FeF_3 battery that has already achieved half of its theoretical gravimetric energy density. Similarly, the fifth battery (Li//H/CuF_2/SA), a Li-CuF_2 battery, has also reached half of its theoretical specific energy, resulting in a specific energy of 1,000 Wh/kg - more than three times the value of current LIBs.

Despite having the highest theoretical specific energy, lithium-air batteries, specifically the fourth battery (Li//C), have not been the focus of much research recently. The practical value obtained, as shown in **Table 2.1**, is quite low. The last battery listed is the solid-state Li-NMC battery (Li/G//$LiNi_{0.8}Mn_{0.1}Co_{0.1}O_2$) with two electrolytes. Despite the lack of information, it appears to have more potential than commercial LIBs.

In conclusion, the comprehensive summary presented in **Table 2.1** highlights the potential of alternative lithium batteries to address the persistent challenge of low specific energy in LIBs.

Table 2.1: A summary of the findings of recent lithium battery studies.

Full battery	Theoretical Specific Energy [Wh/kg][1]	Pratical Specific Energy [Wh/kg]	Ref.
Commercial	460	300	[50]
Li//S	2 600	589	[51, 52]
Li//$Fe_{0.9}Co_{0.1}OF$	1 922	1 000	[53]
Li//C (Lithium-air)	13 000	466	[13, 54]
Li//H/CuF_2/SA	1 874	1 009	[55]
Li/G//$LiNi_{0.8}Mn_{0.1}Co_{0.1}O2$	N/D[2]	500	[11]

[1] Highest value found on literature.
[2] No Data.

2.2.2.2 Aluminum Batteries

Aluminum batteries, one of the previously mentioned alternatives, have garnered significant attention due to several advantages they offer over LIBs. One such advantage is the abundance of aluminum in the Earth's crust, more than 1 000 times as much as lithium, as possible to see in **Figure 2.8**. This abundance results in a lower cost, currently estimated at $ 2 300 per tonne [56], and a simpler and more environmentally friendly extraction process, ensuring a strong supply in the face of high demand. In contrast, lithium is relatively rare and expensive. Additionally, the recycling process of used aluminum is well developed, further enhancing the sustainability of this technology.

Furthermore, unlike lithium, aluminum has the ability to exchange three electrons during the electrochemical process, as represented by **Equation 2.3**.

$$Al \rightarrow Al^{3+} + 3e^{-} \quad (2.3)$$

This property allows for four times the volumetric capacity of lithium (8.0 vs. 2.0 Ah/cm^3), while gravimetric capacities are comparable (3 000 vs. 3 800 mAh/g) [57]. Leisegang *et al.* [57], also suggest that using the same volume of a battery based on an aluminum-metal negative electrode, a car could potentially have two to six times the range compared to commercial LIBs, assuming a liquid-electrolyte-type as well as a solid state LIB with operating voltages of 3 V and a solid state aluminum-ion battery (AIB) with 1.7 V.

All of the aforementioned information related to the gravimetric and volumetric capacity of aluminum batteries is illustrated in **Figure 2.8**.

In summary, aluminum batteries hold great potential as an alternative to LIBs, with their abundance, recyclability, and high energy density, making them an excellent choice for sustainable energy storage solutions

Aluminum batteries are classified into two main groups: aluminum-air batteries (AABs) and AIBs.

Among these, **aluminum-air batteries** are noteworthy for their potential for high volt-

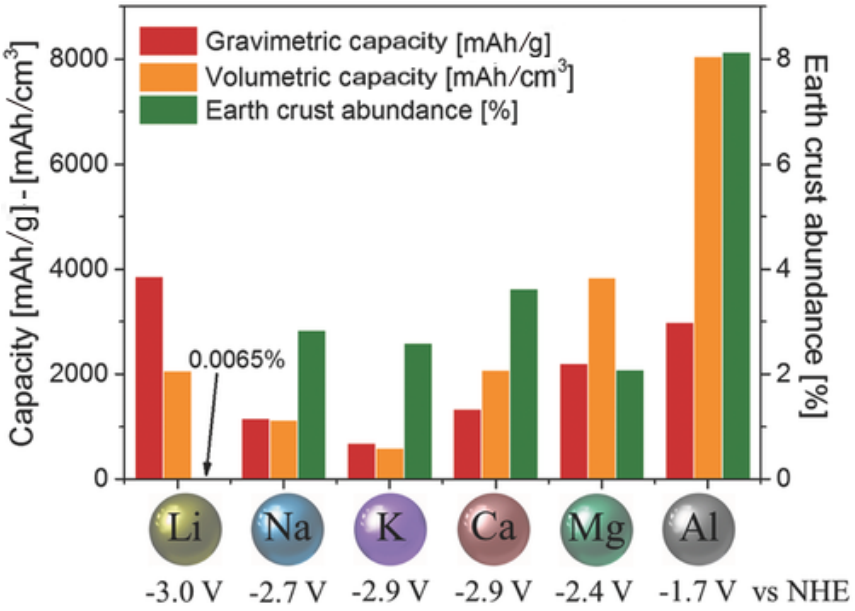

Figure 2.8: Comparison of gravimetric and volumetric capacities, standard reduction potential vs normal hydrogen electrode, and Earth's crust abundance of metal anodes used or proposed for use in electrochemical storage systems. Adapted from [58].

age and gravimetric energy density, with theoretical values of 2.7 V and 8 100 Wh/kg, respectively [59], approaching the specific energy of kerosene. However, these values have yet to be realized in practice. Recent studies and their results are summarized in **Table 2.2**.

Table 2.2: A summary of the findings of recent AAB studies.

Full battery	Specific Capacity [mAh/g]	Specific Energy [Wh/kg]	Ref.
Al//Pd/C	2 750	2 900	[60]
Al//C	1 391	2 086	[61]
Al//CoNi@NCNTs/CC	1 029	1 399	[62]
Al//GDEs/CoO	2 564	2 102	[63]
AL//Ni/C	2 264	3 238	[64]
Al//GDEs/Ni	2 271	3 106	[65]

Upon analyzing the data presented in **Table 2.2**, it becomes evident that although not yet fully developed, AABs display significantly higher specific energy than LIBs. In specific, AABs exhibit between 5 to 10 times higher specific energy than commercial LIBs, resulting in a proportional increase in autonomy. However, it is important to note that there is still ample room for improvement, as none of the studies referenced in **Table 2.2** have achieved even half of the theoretical specific energy values.

Moreover, **Table 2.2** reveals that the nominal voltage of AABs is considerably lower than that of LIBs, measuring at less than 2 V due to the low reduction potential of aluminum, as observed in **Figure 2.8**.

Calculation of nominal voltage is possible through division of specific energy by specific

capacity. This is because specific energy can be approximately calculated by multiplying specific capacity by nominal voltage. **Equation 2.4** exemplifies such a calculation.

$$Specific\,Energy\,[Wh/kg] = Specific\,Capacity\,[mAh/g] \times Nominal\,Voltage\,[V] \quad (2.4)$$

An aluminum-air battery typically consists of an aluminum anode, an air cathode, a separator, and an aqueous electrolyte, typically sodium hydroxide (NaOH), potassium hydroxide (KOH), or sodium chloride (NaCl) [57]. While these batteries have the potential to provide high energy density, they are limited to being primary batteries because the chemical reaction causes severe corrosion on the aluminum anode, resulting in the formation of Al_2O_3 and $Al(OH)_3$ layers on the anode surface [61]. Consequently, the aluminum anode must be replaced after each discharge cycle. However, several studies have explored the possibility of making these batteries rechargeable by using non-aqueous electrolytes, such as ionic liquids (IL) [66, 67].

After analyzing the AABs, it can be concluded that these batteries are a viable alternative to LIBs based on the results presented in **Table 2.2**. This is particularly significant as AABs can potentially resolve the low specific energy issues that plague LIBs and the high cost of materials used.

Aluminum-ion batteries, on the other hand, are a type of secondary battery that, unlike primary batteries, can be recharged, making them more cost-effective and environmentally friendly.

The typical components of an AIB include an aluminum anode, a cathode, a separator, and an electrolyte. The cathode material may vary and include carbon-based (graphite, graphene, carbon paper), metal oxide-based (MoO_2, VO_2, V_2O_5, TiO_2), or sulfur-based (FeS_2, SnS_2, NiS, CuS, WS_2) cathodes [29, 68, 69]. The electrolyte composition can be IL, aqueous solutions, organic solvents, high-temperature molten salts, gels, or solids [29]. As shown in **Figure 2.9**, reports based on IL electrolytes account for the majority of all electrolytes used in AIBs, indicating the importance of IL electrolytes in AIBs.

Even though they have the advantage of being secondary batteries, AIBs have a lower theoretical gravimetric energy density than AABs, which can affect their overall performance. According to research, AIBs have a theoretical gravimetric energy density of around 1 000 - 1 500 Wh/kg [70–73], which is still higher than that of LIBs.

Despite having a higher theoretical gravimetric energy density, in pratice the results on average are lower than LIBs, **Table 2.3** summarizes recent studies on AIBs.

Based on the information presented in **Table 2.3**, it is evident that cathodes composed solely of carbon-based materials in AIBs exhibit superior capacity retention rates, particularly at higher C-rates, when compared to cathodes made from other materials as well

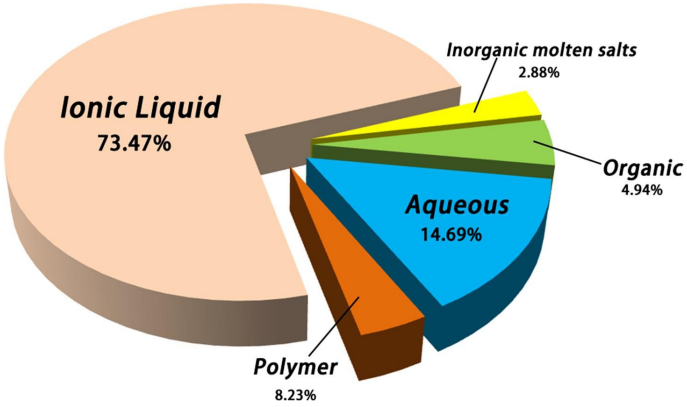

Figure 2.9: Proportion of publications of different electrolytes used in aluminum rechargeable batteries. Reproduced from [29].

Table 2.3: A summary of the findings of recent AIB studies.

Full battery	Specific Energy [Wh/kg][1]	Capacity Retention	Ref.
Al//G/TiO_2	146.3	~ 67 % after 100 cycles at 1 A/g	[74]
AL//ALMO	183	~ 64 % after 1 000 cycles at 0.1 A/g	[75]
Al//FLG	200	~ 100 % after 1 000 cycles at 3 A/g	[76]
Al//NiS_2	204	~ 100 % after 2 000 cycles at 2 A/g	[77]
Al//G/SnS_2	241	~ 18 % after 1 000 cycles at 0.2 A/g	[78]
Al//G	310	N/D	[79]

[1] Highest value reported.

as LIBs. LIBs typically have a lifespan of approximately 500 to 1 000 cycles [80] before reaching the end of their operational life, at which point their capacity has degraded to 80 % [81] of their original capacity. Notably, a battery developed by Chen *et al.* [82] was able to achieve a remarkable capacity retention of nearly 100 % after 250 000 cycles at 100 A/g (~830 C).

Moreover, AIBs have lower discharge/recharge times owing to their high specific currents, which results in increased specific power [29, 76, 77, 82–84]. For instance, the battery of Chen *et al.* was capable of providing a specific power of 175 000 Wh/kg and a charging time of just 1.1 seconds.

Finally, based on the analysis of AIBs and the results presented in **Table 2.3**, it is clear that these batteries are approaching the specific energy of commercial LIBs while offering several advantages. AIBs have a longer lifespan than LIBs and can be charged and discharged more quickly, along with the higher specific power. Moreover, they are more environmentally friendly and have a lower cost, making them a desirable alternative.

As observed in the two types of aluminum batteries previously discussed, IL are frequently employed. The primary reason for using IL in aluminum batteries is to prevent the corrosion of the aluminum anode. However, using IL as an electrolyte offers numerous benefits over commonly used electrolytes, as reported in various studies [29, 85, 86].

To begin with, they have a high thermal stability, allowing them to be employed in high-temperature applications without disintegrating or evaporating. They have a broad electrochemical stability window, which allows them to be used in high-voltage applications without disintegrating or evaporating. Furthermore, they are safer to handle and transport than other solvents because they do not easily evaporate, have low volatility, and produce substantial amounts of volatile organic compounds (VOCs). Additionally, because to their low vapor pressure, they are difficult to ignite, making them safer.

Despite these advantages, ionic liquids also have some disadvantages [86], including higher cost and higher viscosity, which may affect their performance in battery applications. However, the unique properties of ionic liquids make them a promising candidate for improving the efficiency and safety of aluminum batteries.

2.2.2.3 Sodium Batteries

Sodium-ion batteries are rechargeable batteries that use sodium ions as charge carriers to store energy. Like aluminum batteries the biggest advantage SIBs have over LIBs is the abundance of sodium on the crust of earth, as portrayed in **Figure 2.8**. **Figure 2.10**, illustrates a comparison of Na-ion over Li-ion.

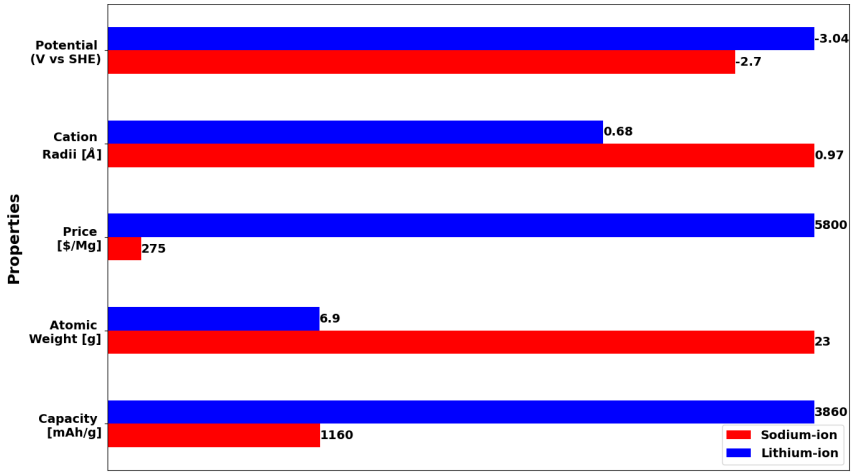

Figure 2.10: Analyzing the characteristics, advantages, and drawbacks of Na-ion and Li-ion Batteries. This price is not up to date as it is constantly changing. Reproduced from [21].

It is clear from **Figure 2.10** that sodium and lithium have comparable reduction potentials (V vs SHE), with sodium having a slightly lower potential (-2.7 V vs -3.0 V). Although sodium ions are larger, they have similar cation radii to lithium ions, but lithium has three times the capacity. It's worth noting that sodium ions have a much higher atomic weight than lithium ions. However, it's interesting to note that the price of sodium per ton is more than 20 times lower than that of lithium, showing why SIBs are potentially more cost-effective alternative to LIBs.

Moreover, Peters *et al.* [87] conducted a comprehensive life cycle assessment (LCA) study of a representative SIB and compared its environmental performance with existing studies on LIBs. The findings are summarized in **Figure 2.11**, where GWP represents global warming potential, FDP represents fossil depletion potential, MEP represents marine eutrophication potential, FEP represents freshwater eutrophication potential, HTP represents human toxicity potential, and TAP represents terrestrial acidification potential.

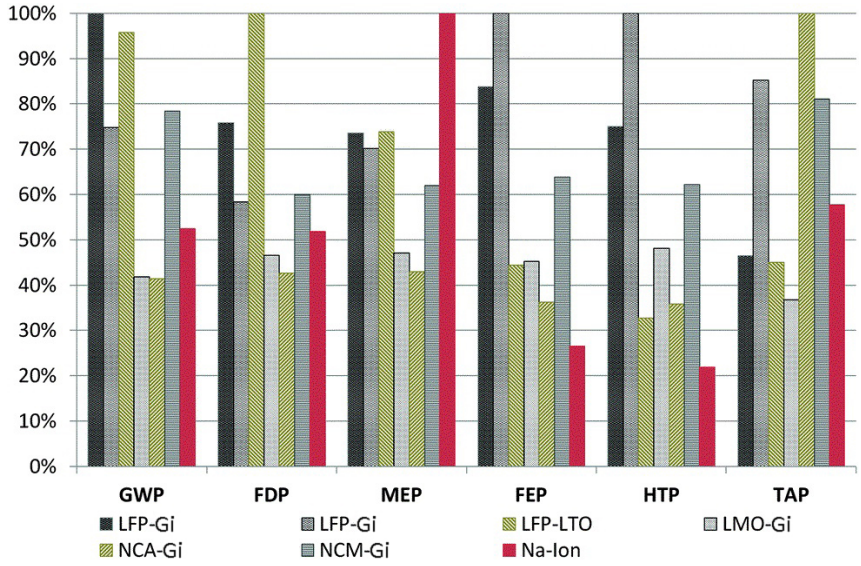

Figure 2.11: Each assessed category's relative contribution to environmental impacts per kWh of storage capacity. LFP = lithium iron phosphate, LTO = lithium titanate, LMO = lithium manganese oxide spinel, NCA = layered lithium nickel cobalt aluminum oxide, NCM = layered lithium nickel cobalt manganese oxide, and Gi = graphite. Reproduced from [87].

According to **Figure 2.11**, the evaluated SIB exhibits lower environmental impact in terms of effects on global warming, human toxicity, freshwater contamination, soil acidification, and fossil depletion, despite the fact that its battery chemistry is at a significantly lower technical development stage than commercially available LIBs.

Sodium-ion batteries, like the batteries mentioned earlier, are made up of several components, including a positive electrode made of sodium-layered oxides, 3D polyanion oxides, and organic materials, a negative electrode made of carbonaceous materials, metal oxides, organic materials, and phosphorous materials, an electrolyte, and a separator [88]. These components collaborate to ensure that SIBs operate efficiently and reliably.

The cell chemistry of SIBs closely resembles that of LIBs [89], eliminating the need to reinvent the wheel. The materials and processes used in LIBs, can be adapted for use in SIBs.

Furthermore, SIBs have a higher theoretical gravimetric energy density than LIBs, 500 - 1 000 Wh/kg [90–92] depending on the material for the electrodes used. However these currently have lower gravimetric energy density than LIBs. **Table 2.4** summarizes a num-

ber of studies and their findings on SIBs.

Table 2.4: A summary of the findings of recent SIB studies.

Full battery	Specific Energy [Wh/kg][1]	Specific Power [W/kg]	Ref.
S@CoS_2-IL//$Na_{0.44}MnO_2$	103	N/D	[93]
S@MNC-600//$Na_{0.44}MnO_2$	110.6	N/D	[94]
$CoSe_2$-CNS//NVPOF	115	194	[95]
1.5-ZnS@CNFs-800//NVP	156.9	690	[96]
GeS_2//NVPOF	213	221	[97]
$SnSe_2$/NPC//NVPF	583	256	[98]

[1] Highest value reported.

According to **Table 2.4**, the majority of the studies cited did not achieve even half of the specific energy of commercial LIBs. However, the last battery on **Table 2.4** shows that SIBs can potentially have higher specific energy than LIBs, because it achieved 583 Wh/kg while LIBs only achieved 460 Wh/kg. Furthermore, due to faster discharge and charge rates, SIBs have the potential to achieve higher specific power. For example, the last battery ($SnSe_2$/NPC//NVPF) on **Table 2.4** can be charged/discharged in 11.9 seconds and possesses a specific power of 36,000 W/kg while its specific energy is limited to 119 Wh/kg [98]. The second to last battery (GeS_2//NVPOF), on the other hand, can deliver a specific power of 4 448 W/kg at a specific energy of 149 Wh/kg [97].

Table 2.4 also demonstrates the significant impact of electrode materials on gravimetric density, with some achieving nearly 600 Wh/kg, while others not even reaching 150 Wh/kg.

Lastly, as evidenced by the results in **Table 2.4**, SIBs have the potential to outperform LIBs in terms of performance. SIBs have a lower environmental impact, a lower cost, faster charge and recharge times, and the potential for higher specific power.

All the works previously cited were used to create the following figures, namely, **Figure 2.12** and **Figure 2.13**, and to draw conclusions.

Based on the data presented in **Figure 2.12**, it is apparent that among the AIBs and SIBs discussed in this work, SIBs are the systems with the highest specific energy. However, on average, AIBs demonstrate better performance (214 vs 212.8 Wh/kg), with a specific energy already approaching that of commercial LIBs (214 vs 300 Wh/kg), despite being a relatively new area of research.

Moreover, the works referenced in this study suggest that AIBs exhibit better capacity retention and the potential for higher specific power than SIBs.

According to the data presented in **Figure 2.13**, it is clear why new alternatives to lithium-ion batteries have emerged to replace them, as they are approaching their theoretical maximum specific energy, already achieving 65 % of it. It is also evident that two of the lithium alternatives, namely Li-FeF_3 and Li-CuF_2 batteries, have already achieved more than 50 % of their theoretical specific energy. However, Li-air batteries have only reached 4 % due

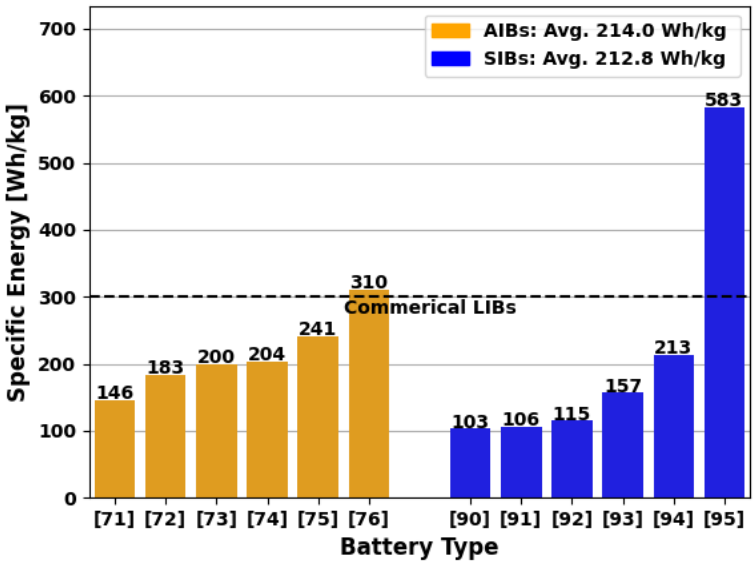

Figure 2.12: Comparison of AIBs and SIBs in terms of specific energy with commercial LIBs.

to the limited research conducted on them.

Furthermore, from **Figure 2.13**, AABs demonstrate the highest practical specific energy, even though they have only achieved 31 % of their potential. On the other hand, AIBs have reached 14 %, indicating that there is still a lot of room for improvement. The same can be said for SIBs, which have achieved 21 %. It is worth noting that AIBs have a higher theoretical potential than SIBs.

This review highlights that there is still a lot of potential for improvement in battery technology, with new advancements emerging regularly. Looking towards the future, there is a need for energy storage devices that are safer, greener, and more efficient, especially as they are increasingly used to power electric vehicles, UAVs, high altitude satellites, and electric planes. One promising approach to achieving these goals is through the use of multifunctional systems and materials [99].

In this context, the concept of batteries, which are capable of storing electric energy while also carrying mechanical loads, *i.e.* **structural batteries**, is a highly attractive application of multifunctionality.

2.3 Structural Batteries

As mentioned in the previous section, structural batteries are designed to possess both electrochemical energy and mechanical load-bearing capabilities, allowing them to reduce the amount of conventional structural materials required by devices and the weight. Two

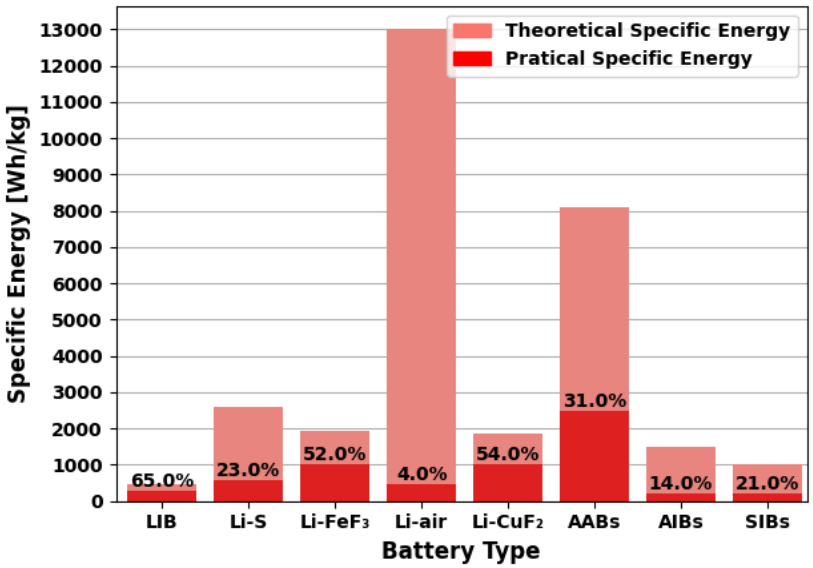

Figure 2.13: Comparison of different types of batteries based on the specific energy achieved in relation to its theoretical potential.

main approaches have been developed for the design of structural batteries: **decoupled** and **coupled** designs.

In the decoupled approach, the structural framework is bifurcated into two distinct components: the electrochemical component, responsible for energy storage, and the mechanical bearing or structural component, accountable for carrying loads *i.e.*, multifunctional system, wherein a battery is embedded within composite laminates or sandwich panels comprising materials like CF or others [100–106]. On the other hand, the coupled approach entails the integration of functions at the material level, *i.e.*, a multifunctional material. For instance, the active material is coated onto CF, allowing it to serve the dual purpose of energy storage and load support. Additionally, the matrix material can function as both an electrolyte and a structural binder for the fibers [107–119]. Consequently, the electrochemical components not only facilitate energy storage but also contribute to the load-bearing capabilities of the structure itself. In this manner, they can be seamlessly integrated into a structural component or even serve as the structural component itself to attain the require rigidity to function as a structure.

Considering the aforementioned, it is vital to remember that in coupled SBs, many of the electrochemical and mechanical outcomes concern the reinforced electrochemical components alone, rather than their integration inside a structural component. Therefore, it should be acknowledged that the majority of these components lack the rigidity and stiffness required to function as independent structures. When interpreting the results, this factor must be considered.

Before continuing, it's important to note that a composite material is composed of multi-

ple micro-components that work synergistically, even though they differ in physical form and/or chemical composition. Typically, these materials comprise two distinct phases with a matrix phase surrounding a reinforcement phase. This enables the beneficial properties of both materials to be effectively utilized. Matrices can be made from a variety of materials, including metallic, polymeric, or ceramic materials. In the case of polymeric materials, different types of resins, such as epoxy, phenolic, polyester, or vinyl ester, can be used as the matrix. Reinforcements typically come in the form of fibers, crystal particles, filaments, or whiskers.

Hopkins *et al.* [120] conducted a meta-analysis of reported structural batteries and found that decoupled structural batteries, in general, achieve higher elastic modulus and higher specific energy when compared to their coupled counterparts. The researchers suggested that this is because load-bearing components are positioned on the outermost surfaces of the decoupled batteries, resulting in higher flexural rigidity. On the other hand, coupled structural batteries tend to perform poorly due to their use of structural electrolytes that reduce ionic conductivity and/or carbon-fiber current collectors that have high ohmic resistances.

Moreover, the researchers concluded that structural battery research should concentrate on batteries with none or minimum thermal runaway. AABs that use aqueous electrolytes or AIBs that use ionic liquids with high thermal stability are examples of such batteries.

Figure 2.14 provides a summary of the findings of Hopkins *et al.*, indicating that decoupled structural batteries outperform coupled batteries. However, it is worth noting that none of the structural batteries referenced in the study achieved the specific energy of the 18650 Li-ion battery presented in the figure. Furthermore, the figure illustrates that there is a trade-off between specific energy and elastic modulus, suggesting that an increase in one will lead to a decrease in the other. These findings suggest that more research is needed to optimize the performance of structural batteries, with a particular focus on balancing the trade-off between specific energy and elastic modulus.

In envisioning a structural battery, the combination of LIB technology and a CF composite laminate is the most commonly utilized technology. Carbon fibers have been found to serve both as an excellent reinforcement material and as a negative electrode in an LIB [121]. However, to achieve good mechanical performance, the fibers must be integrated into a solid matrix material that evenly distributes the mechanical load, unlike in conventional LIBs where the electrolyte is in a liquid form. There is often a trade-off between ion conduction and mechanical stability, and this is demonstrated in **Figure 2.14**. A new type of electrolyte material, the structural battery electrolyte (SBE), has recently been developed to facilitate this process [122].

Batteries can be further classified based on the chemistry used, such as LIBs or non-LIBs, due to their popularity in structural battery applications, as well as the reinforcement technique used, such as mainly CF reinforcement or non-CF reinforcement, due to

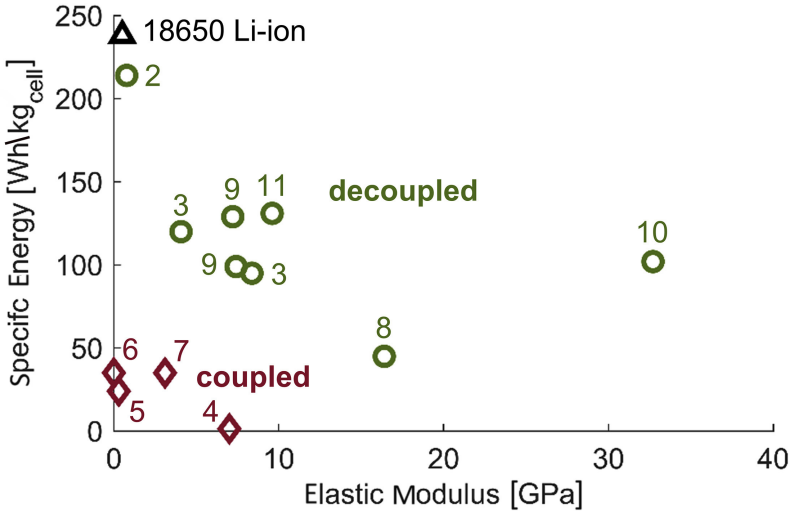

Figure 2.14: Cell-level specific-energy values versus corresponding Young's modulus of reported structural batteries, numbered by their references. Reproduced from [120].

their widespread use for reinforcing SBs. In this case, the term "reinforcement" encompasses not only the materials utilized to strengthen the electrodes, but also the composite structures of both decoupled SBs and coupled SBs that provide stiffness and strength to function as standalone structures.

2.3.1 Multifunctional Performance

The primary goal of a structural battery is to enable weight reduction in vehicles compared to the same vehicle with separate structure and battery components, thereby improving performance. In addition to the increase in efficiency and range mentioned earlier, the reduction in weight can also lead to improved handling and maneuverability, as well as a reduction in noise and vibration.

Johannisson *et al.* [17] modeled a structural battery to evaluate its potential for mass savings, proposing **Equation 2.5** to assess multifunctional performance, specifically mass savings. Additionally, the team analyzed the impact of individual parameters such as the volume fraction of fibers in the anode, cathode, and separator, electrolyte thickness, carbon fiber area density, and ionic conductivity of SBE on the structural battery's mass.

$$m_{SB} < m_{CF} + m_{LIB} \quad (2.5)$$

In **Equation 2.5**, m_{SB} is the mass of the structural battery, m_{CF} represents the conventional CF composite plate's mass, and m_{LIB} denotes the standard LIB's mass. The equation reveals that structural batteries must weigh less than both the monofunctional plate and the battery combined to outperform them.

This model ensures that the structural battery has the same mechanical stiffness for a given load case as the conventional CF composite plate. Furthermore, the structural battery and standard LIB store the same amount of electrical energy, as depicted in **Figure 2.15a**. The battery model's components include CF for the anode, CF coated with active materials ($LiFePO_4$) for the cathode, a glass fiber (GF) separator, and SBE for the electrolyte, with additional materials employed to enhance performance. Their stacking sequence can be seen in **Figure 2.15b**.

(a)

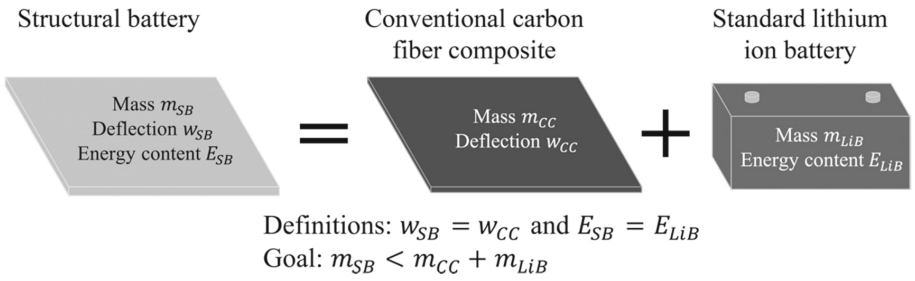

(b)

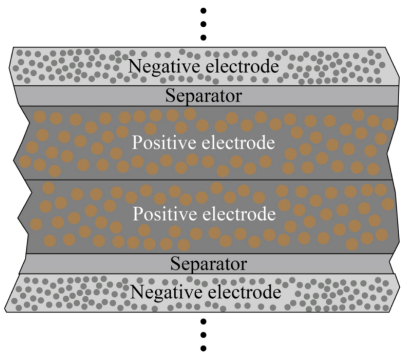

Figure 2.15: (a) Schematic representation of the modelled systems. (b) Layup of cell in the stacked structural battery. Reproduced from [17].

Initially, the structural battery failed to achieve any mass savings and instead increased by 5 %, but Johannisson *et al.* discovered the optimal parameter values to achieve mass savings, as calculated by **Equation 2.6**, obtaining a specific energy of 110 Wh/kg.

$$Mass\ Savings_{\%} = \frac{m_{CF} + m_{LIB} - m_{SB}}{m_{CF} + m_{LIB}} \times 100 \quad (2.6)$$

One of the case studies involved modeling an aircraft interior panel. By utilizing the structural battery model, the team achieved a total mass savings of 67 % compared to a conventional interior panel of an aircraft. However, if compared to a CF interior panel with the same material properties as the presented model, the mass savings were only 4 %. These outcomes are noteworthy since every decrease in aircraft mass results in increased efficiency and reduced fuel consumption in the aeronautic sector, with a decrease of approximately 8 to 17 kg in fuel for every 100 kg [123]. A detailed presentation of these

findings and additional information can be found in **Figure 2.16**.

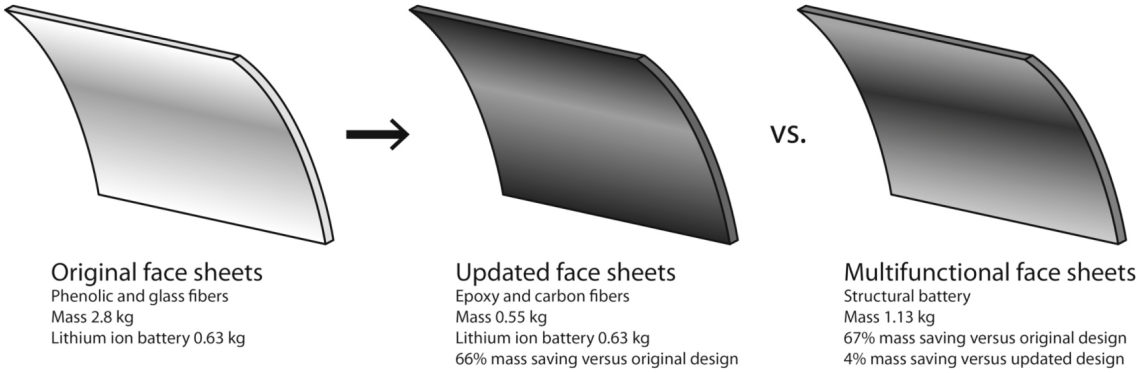

Figure 2.16: The schematic and results of using structural batteries in aircraft interior panels. The panel's original face sheets are made of glass fiber phenolic prepreg, which has been improved with carbon fiber and epoxy face sheets. These updated face sheets are compared to structural battery face sheets, as well as corresponding lithium ion battery. Reproduced from [17].

Johannisson *et al.* [17] evaluated the use of an SB in an electric car roof as another case study. The mass reduction achieved in this case was much greater than in the case of the aircraft interior panel, because the roof of a car does not need to support heavy loads, but rather must be strong enough to withstand pressure on its surface without permanent deformation. This enabled the use of an SB with a different layout than the one used in the previous case study. The findings of this case study, as well as additional information, are presented in **Figure 2.17**.

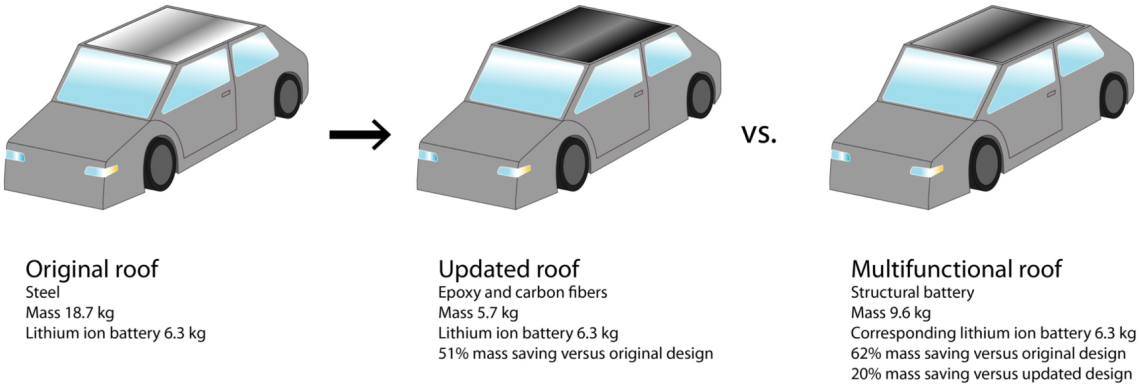

Figure 2.17: The schematic and results of modeling structural batteries in an electric vehicle's roof. The original steel roof has been replaced with a carbon fiber and epoxy roof. A structural battery roof is compared to this updated roof and its corresponding lithium ion battery. Reproduced from [17].

A recent study evaluating the performance of SBs was conducted by Asp *et al.* [18]. In this study, the authors employed commercial electric vehicles, including the Tesla Model S with a mass of 2,040 kg and the BMW i3 weighing 1,300 kg, to simulate an SB and assess

its impact on the range of electric vehicle drives.

The battery used in the study had a CF negative electrode, CF coated with active materials (NMC) positive electrode, a separator, a insulation layer, carbon reinforcement polymer, and SBE for the electrolyte. The researchers selected the battery layup, as shown in **Figure 2.18**, to minimize internal resistance, improve cell capacity, balance the amount of electrode materials, and ensure a balanced and symmetrical laminate to prevent deformation and warpage. Due to these and other factors, each SB cell had a total specific energy of 105 Wh/kg.

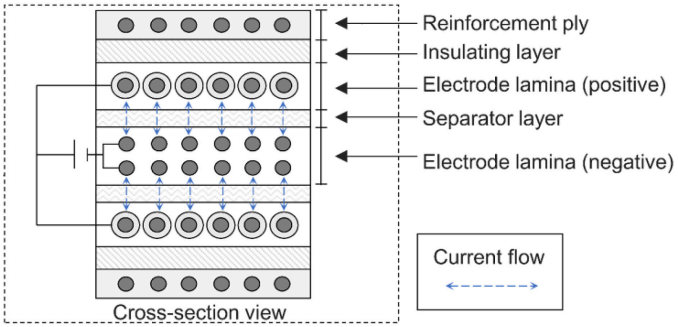

Figure 2.18: Schematic illustration of the structural battery design and layup proposed for the individual battery cell used in the study as baseline design configuration. Adapted from [18].

Asp *et al.* [18] conducted three case studies for each car. In the first case study, 70 % of the interior panels were replaced with SBs and the existing batteries were removed. In the second case study, the researchers replaced 60 % of the space frame/life module in the cars with SBs, in addition to the changes made in the first case study. In the third case study, the mass of SBs used in case study 2 was doubled. All masses and final results are presented in **Table 2.5**. The relative range was determined by dividing the range of each case by the original range.

Table 2.5: Case studies for the two electric vehicles and results of the benefits of using structural batteries. Adapted from [18].

Vehicle	Case n.	Mass of SB [kg]	Total vehicle mass [kg]	SB mass fraction	Relative Range [%]
Tesla Model S	Real	0	2040	0	100
Tesla Model S	1	270	1 500	0.18	32
Tesla Model S	2	490	1 500	0.33	64
Tesla Model S	3	980	1 990	0.49	120
BMW i3	Real	0	1 300	0	100
BMW i3	1	170	1 070	0.16	33
BMW i3	2	260	1 070	0.24	83
BMW i3	3	520	1 330	0.39	172

The results shown in **Table 2.5** reveal that in the second case study, the Tesla Model S and BMW i3 experienced a decrease mass of 25 and 18 %, respectively, while still maintaining

a range of 64 and 83 % of the original range. In addition to that, for approximately the same total mass as the original vehicles, the range increased by 20 and 72 % for the Tesla Model S and BMW i3, respectively. These findings indicate that the total mass of the cars would be reduced for the same range as the original. A simple interpolation was performed using Python software to calculate this mass. The mass fraction of SB for the Tesla Model S was 0.44, resulting in a final mass of 1 808 kg and an 11 % mass reduction. Similarly, the mass fraction of SB in the BMW i3 was 0.27, resulting in a final mass of 1 109 kg and a 17 % mass reduction.

Asp *et al.* [18] noticed that the total range increase for BMW i3 was greater than that for Tesla Model S, despite the fact that the mass fraction of SB was lower. This implies that lighter vehicles may benefit more from SBs, as shown in **Table 2.5**. However, the assumption that using SBs in large aircraft will not result in any improvement is invalid. The amount of space available for SBs in an aircraft differs from that in a car, but for aircraft of the same size, the lighter one will show better performance.

A study conducted by Thomas and Qidwai [124] aimed to evaluate the endurance increase of a small unmanned aerial vehicle (UAV) with the implementation of SBs in its wing structure. The SBs used in the study were fabricated by Telcordia Technologies of Red Bank, New Jersey. For this purpose, they considered three case studies, including PLI Wasp I with four embedded SBs, two on the top and two on the bottom of the wing structure, PLI Wasp II with two embedded SBs only on the top skin of the wing structure, and Kokam Wasp with conventional batteries. These case studies are illustrated in **Figure 2.19**.

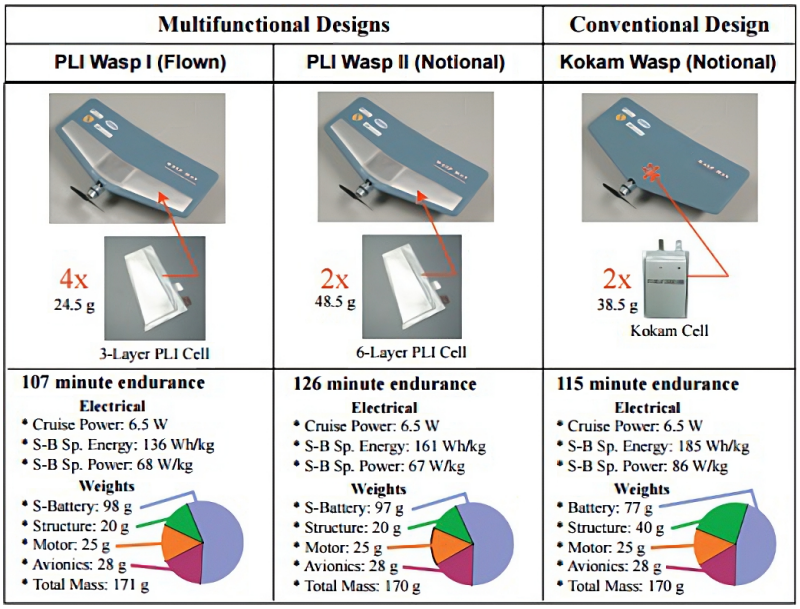

Figure 2.19: A multidisciplinary design optimization study of the flight endurance time for three case studies of the UAV. Reproduced from [124].

From the comparison in **Figure 2.19**, it can be observed that for the first case study, the

endurance is lower compared to the conventional design. However, for the second case study, there is an increase in endurance of 11 minutes compared to the conventional design. The second case study performs better than the first because the weight wasted on packaging is smaller, with only 2 packs of SBs compared to 4 in the first case study. Therefore, for the same endurance, the second case study would be lighter than the conventional design.

It is important to note that SB implementation must be done correctly in order to achieve the desired results. The first implementation of SBs actually resulted in a decrease in endurance when compared to the conventional design. This emphasizes the significance of proper implementation and design considerations when using SBs in vehicles.

In conclusion, it is clear that SBs have the potential to improve the performance of electric vehicles by reducing their weight. In their study, Asp *et al.* [18] showed that by replacing LIBs with SBs, the mass of a Tesla Model S and a BMW i3 can be reduced by 11 % and 17 %, respectively, while maintaining the same range, and there is an increase in range, 20 % and 72 %, respectively, for the same mass. Similarly, the study by Thomas and Qidwai [124] demonstrated that the implementation of SBs in the wing structure of a small UAV can increase its endurance by up to 11 minutes compared to a conventional battery design.

The following subsections aim to review recent works related to the development of SBs and their potential applications.

2.3.2 Coupled Structural Batteries

2.3.2.1 Carbon Fiber Reinforcement and Lithium-Ion Chemistry

It is worth noting that the US Army Research Laboratory (ARL) made the first attempt to create a coupled laminated SB [112] in 2007. In this study, two structural anode fabrics were tested, namely a plain-woven carbon fabric (from Textile Products Inc.) and a non-woven carbon fabric (from Hollingsworth and Vose). The results indicated that a woven carbon fabric anode produced a SB with higher specific stiffness than a composite battery.

For the cathode, stainless steel mesh was used, specifically, a woven mesh (from McMaster-Carr), an expanded foil (from McMaster-Carr), and a perforated foil (from Dexmet) were tested. Tensile tests showed that the perforated metal foil produced a SB with higher specific stiffness than the other materials. The SBs were assembled using a GF separator (from Vector Ply) and an electrolyte consisting of vinyl ester random copolymer (from Sartomer Company).

To prevent moisture intrusion during fabrication, the SBs were processed using a modified vacuum-assisted resin transfer molding method. The mechanical results obtained were positive, with a Young's modulus of 8 GPa. However, the authors noted that during testing, the carbon fabric did not fail, indicating that the load was not effectively trans-

ferred into the carbon fabric. If the load had been distributed properly and the matrix had provided complete adhesion and load transfer, the carbon fabric should have failed first, since it cannot sustain as much strain as the stainless steel and GF.

The authors concluded that the lack of failure in the carbon fabric could be attributed to several factors, such as poor fiber-matrix interface, low matrix stiffness and/or strength in combination with insufficient end tab length, or inadequate sample size.

In terms of electrochemical performance, the SBs demonstrated poor electronic insulation. The most probable cause of this was that during the manufacturing of the SBs, resin flow dragged particles from the active material in the cathode substrate and spread through the composite.

In conclusion, this study provides valuable insights into the development of SBs and highlights some issues that must be addressed, such as the fiber-matrix interface and being cautious with the manufacturing process to avoid particle contamination.

Moyer *et al.* [108] have also developed a coupled SB utilizing CF as both the current collectors and load-bearing components. They used Gi for the anode material and $LiFePO_4$ incorporated with conductive CNTs as the cathode material, which were coated onto thermally processed CF weave materials. The Whatman GF filter was used as the separator, and the electrolyte used was 1 M LiTFSI in 1-ethyl-3-methylimidazolium tetrafluoroborate (EMIMBF4) ionic liquid.

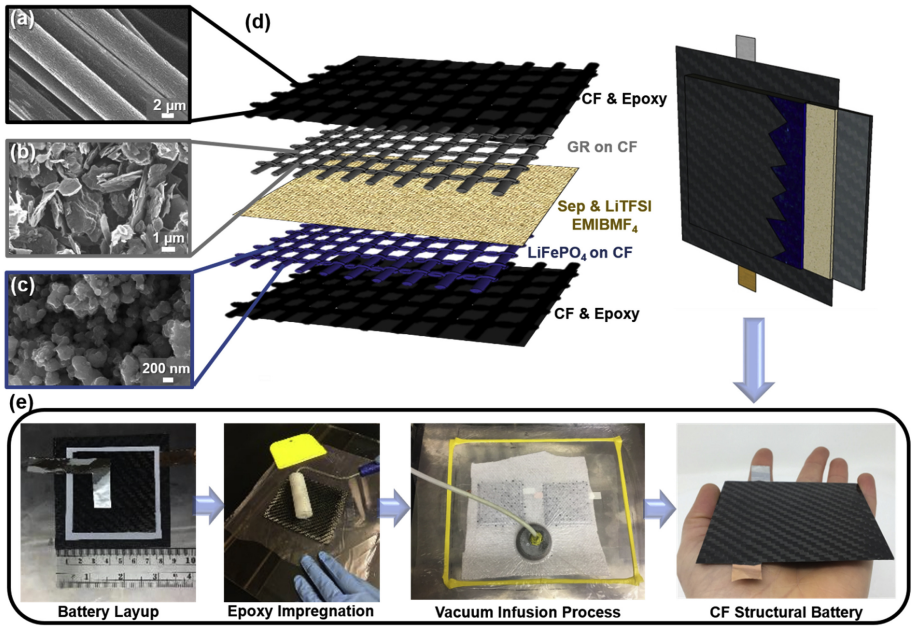

Figure 2.20: Carbon fiber battery composite fabrication as depicted by SEMs: (a) Carbon fiber; (b) Graphite; (c) Lithium iron phosphate; (d) Scheme depicting the stacking of the individual layers of the composite battery alongside a picture of these layers cured into a composite material. (e) Composite layup process depicted alongside a picture of a carbon fiber composite structural battery panel being held. Reproduced from [108].

The battery layup of CF/Gi/LiTFSI in EMIMBF4/LFP/CF was then sandwiched between epoxy-impregnated CF and placed under vacuum to cure. To overcome the air stability issues of the electrolyte, they directly assembled the battery components and electrolyte into the carbon fiber composite through a traditional composite layup process. **Figure 2.20** illustrates the various components present in the SB, the manufacturing process, and the final result.

Galvanostatic charge discharge measurements were conducted to evaluate the SB's energy storage performance at different rates ranging from 0.10 to 1.0 C. The SB's energy density was found to be 36 Wh/kg at 0.10 C and 10 Wh/kg at 1 C. **Figure 2.21a** presents the charge and discharge cycles at various C rates, while the corresponding specific energy is shown in **Figure 2.21b**.

The mechanical performance of the SB was determined by tensile testing at a strain rate of 2 mm/min, and the results showed an ultimate tensile stress of 213 MPa and a Young's modulus of approximately 1.8 GPa. The stress-strain curve of the tensile testing is shown in **Figure 2.21c**. In the case of this coupled SB, the reinforced electrochemical components are seamlessly integrated within a structural component, providing not only enhanced mechanical performance but also increased rigidity.

In addition, the authors conducted simultaneous testing of the SB's mechanical properties and battery electrochemistry by performing galvanostatic charge discharge measurements at 0.1 C under various loads. The results are presented in **Figure 2.21d**. According to these results, the higher the mechanical load, the lower the specific energy of the SB.

The authors also observed that the electrochemical properties did not recover significantly after the load was removed, indicating that the mechanical stress caused residual damage, namely delamination at the interfaces. This underscores the importance of reinforcing strategies across the carbon-battery material-epoxy interface to achieve complete battery performance under significant mechanical stress. Besides the mechanical stress, the chemical reaction occurring inside the battery also contributes to delamination.

To showcase their battery in a more practical example, they built a CubeSat using four SB as side panels. By integrating energy storage into the CubeSat structural frame, the improved gravimetric and volumetric performance of the system allows more volume and mass for additional contents into the CubeSat assembly, enabling improved value for an individual CubeSat mission. They additionally supplied power to an LED and an electric fan, as depicted in **Figure 2.22**.

Moyer *et al.* [110] attempted to address the issue of SB component delamination by introducing a binder. The authors employed the same materials as in a previous study, with the only difference being the use of a Celgard 2525 separator. The manufacturing process remained unchanged, but a polyacrylonitrile (PAN) coating was applied to both electrodes.

The results of the study indicated that the SB with PAN achieved a higher specific energy

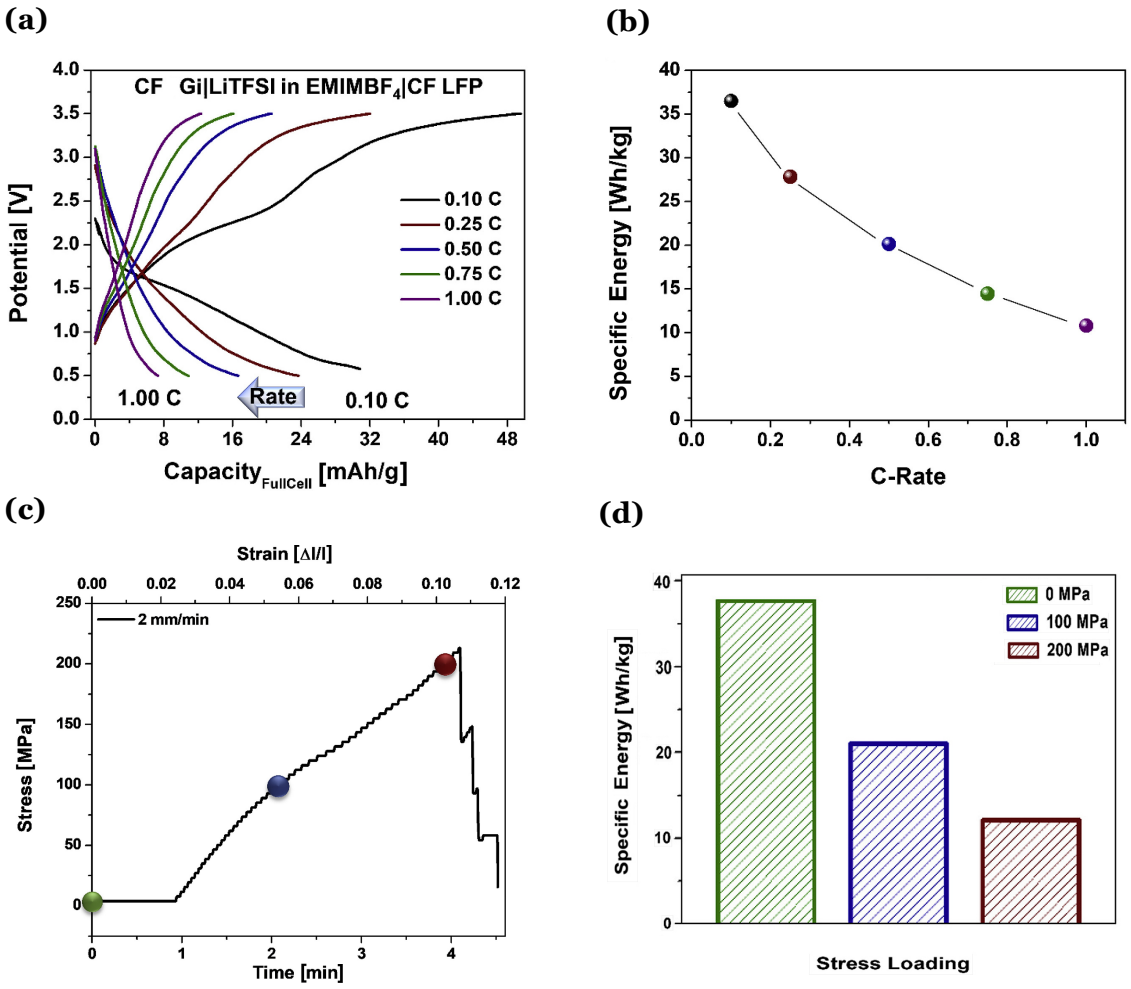

Figure 2.21: (a) First cycle charge discharge curves at each rate. (b) Average specific energy at each rate. (c) Stress strain curve of tensile testing. (d) Specific energy at different stress loadings. Adapted from [108].

of 58 Wh/kg compared to its counterpart without PAN, which only reached 21 Wh/kg at 0.10 C. Moreover, the SB with PAN exhibited a capacity retention of 80 % after 100 cycles, while the counterpart achieved only 63 %. Because the PAN coating mechanically reinforces the carbon fiber-battery material interface and provides an electroactive transport medium for lithium ions by sandwiching the active battery material between the CF and PAN coating. **Figure 2.23** illustrates the effects of the PAN coating on the electrodes during stress, demonstrating that the PAN coating ensures that the active material sticks to the surface of the CF. Due to this the SB had a ultimate tensile strength of 228 MPa and a Young's modulus of 2.6 GPa.

A similar SB was developed by Asp *et al.* [109], wherein CF fiber (from Oxeon AB) was used as the anode. Unlike Moyer *et al.* study, they did not coat any active material in the CF, but the CF itself served as the active material. For the cathode, they used an aluminum foil coated with LFP (from Custom Cells Itzehoe GmbH). Two types of GF were used for the separator: Whatman GF/A separator (from Sigma Aldrich) and a plain weave GF (from

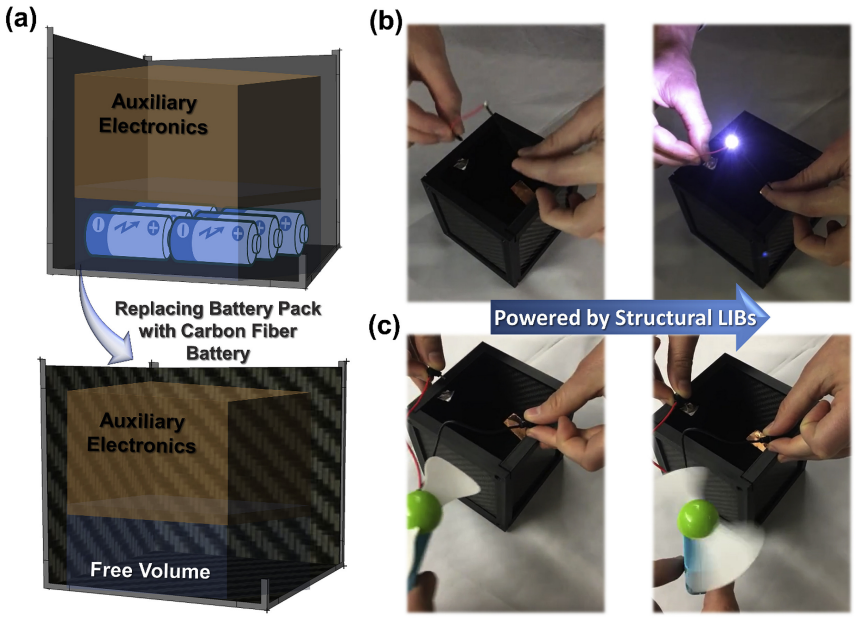

Figure 2.22: (a) Replacing interior external battery pack with structural battery creates free volume within the CubeSat chassis.(b) Lighting a LED. (c) Operating a fan. Reproduced from [108].

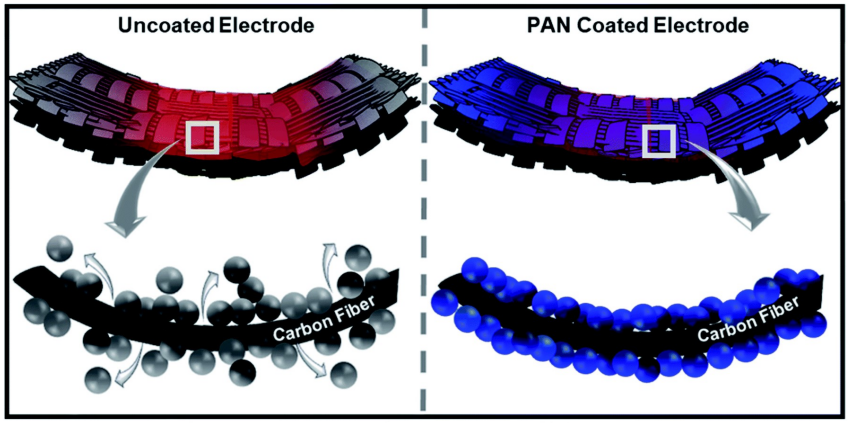

Figure 2.23: Scheme illustrating stress distribution and material delamination in carbon fiber structural battery electrodes with and without a PAN coating. Reproduced from [110].

Gividi Fabrics s.r.l.). It is worth noting that the former separator is thicker than the latter. A SBE mixture was used as the electrolyte.

The manufacturing process of the SB is illustrated step-by-step in **Figure 2.24**.

After the curing of the SB, the authors performed a scanning electron microscope (SEM) analysis and observed that the thickness of the CF varied significantly across the width of the structural battery cell due to the pressure, and this difference differed between the two separator solutions, which could affect the electrochemical performance of the cell.

The electrochemical performance was evaluated through galvanostatic cycling at different

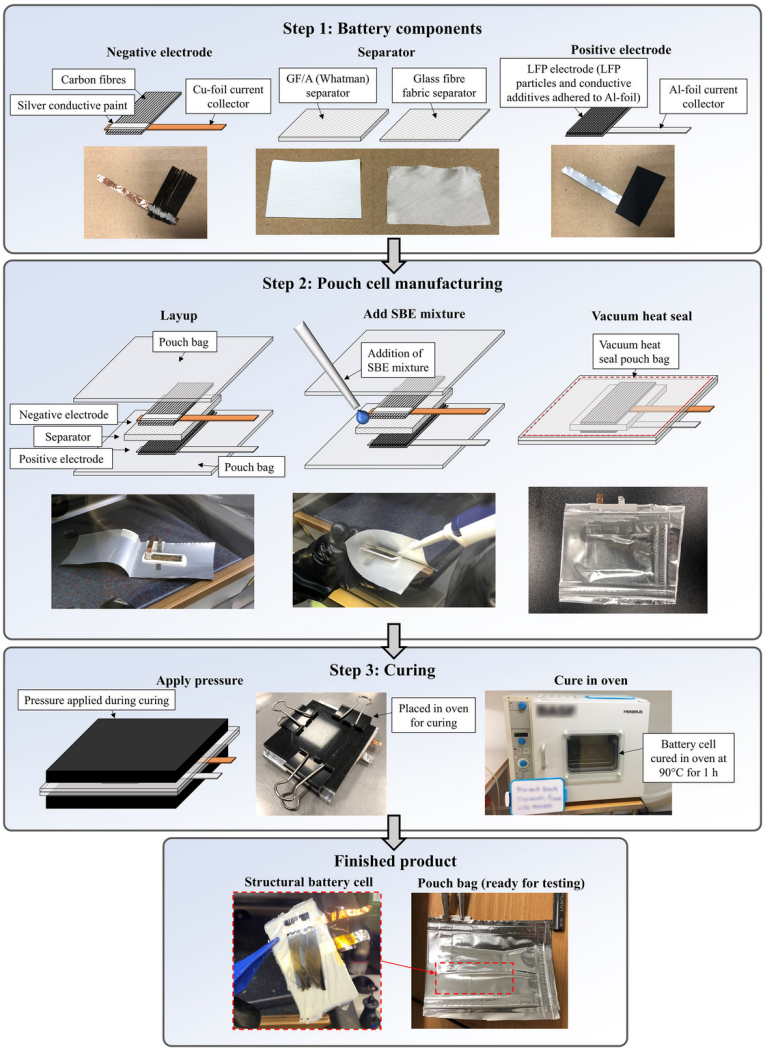

Figure 2.24: Structural battery composite fabrication, showing the steps: battery component manufacture, pouch-cell manufacture, and curing. Reproduced from [109].

C rates, and it was found that the specific energy of SB utilizing the Whatman GF/A and GF plain weave separator were 11.6 and 23.6 Wh/kg, respectively at 0.05 C. The difference in performance was attributed to the thickness of the Whatman GF/A, which was higher than that of the GF plain weave, leading to higher internal resistance, thus reducing the maximum available capacities of the electrodes. Additionally, the specific powers for the two cells at 3 C were 5.94 and 9.56 W/kg, respectively.

In **Figure 2.25**, the electrochemical results of the SB using the Whatman GF/A separator are presented. **Figure 2.25a** depicts the typical charge/discharge voltage profiles of the structural battery cells during galvanostatic cycling at different C rates, which indicate a stable charge/discharge process at the different C rates and a relatively balanced cell. Furthermore, **Figure 2.25b** shows the specific energy for different C rates, demonstrating that the difference between specific energy during charge and discharge is minimal. In **Figure 2.25c**, good capacity retention is observed. **Figure 2.25d** presents a comparison between specific energies from the two types of SBs.

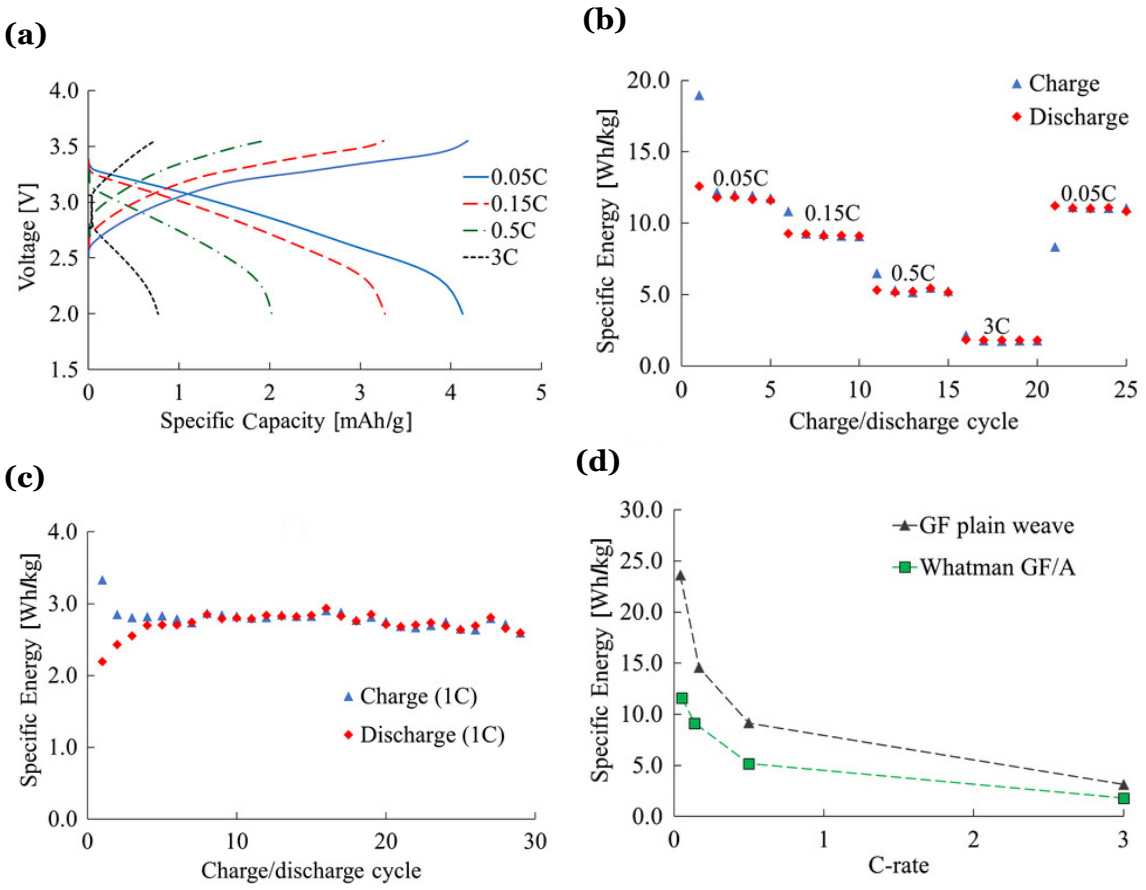

Figure 2.25: Results from electrochemical characterization based on the total mass of the battery cell. (a) Voltage profile at different C rates. (b) Specific energy at different C rates. (c) Long-term cycling (at 1 C). (d) Specific energy versus C rate for the two separator solutions. Adapted from [109].

To assess the mechanical performance of the structural batteries, Asp *et al.* [109] conducted a tensile loading analysis in both the x- and y-directions, utilizing the GF plain weave separator positioned with the fibers extending either in $\pm 45°$ or $0°/90°$ directions. It is worth noting that the $0°$ direction is parallel to the x-direction, while the CF fibers are also oriented parallel to the x-direction. The mechanical properties of each structural battery are listed in **Table 2.6**.

Table 2.6: Mechanical behavior at tensile tests of the structural battery laminates. E_x and E_y are the Youngs' modulus in the x- and y-directions, respectively. σ_x and σ_y are the tensile strengths in the x- and y-directions, respectively.

Property	Separator		
	Whatman GF/A	GF plain weave $\pm 45°$	GF plain weave $0°/90°$
E_x [GPa]	18.3	14.6	25.4
E_y [GPa]	2.9	2.8	13.3
σ_x [MPa]	> 163	> 312	> 287
σ_y [MPa]	> 16	> 34	> 72

The SB utilizing GF plain weave with fibers in directions $0°/90°$ exhibits the best overall

mechanical performance. However, it is noteworthy that the SB with GF plain weave separator and fibers in direction $\pm 45^{\circ}$ boasts the highest tensile strength, reaching 312 MPa in the x-direction. In general, the GF plain weave separator contributes to a higher tensile strength in both directions compared to the alternative separator. This is attributed to the thinner separator, which leads to a lower absorption of SBE, thereby improving both mechanical and electrochemical performance. The authors further noted that the electrochemical performance is unaffected by the variation in GF orientation.

In contrast to previous authors, Liu *et al.* [111], instead of building a traditional three-layer battery with a cathode, separator, and anode, they designed a continuous polymer structure reinforced with carbon fibers to form the entire solid-state battery. This method effectively eliminated the electrode/separator interface, resulting in a single solid polymer entity with fibers, as illustrated in **Figure 2.26**. The structural polymer, reinforcing fibers, and active material can be clearly observed in the figure, demonstrating the successful integration of these components.

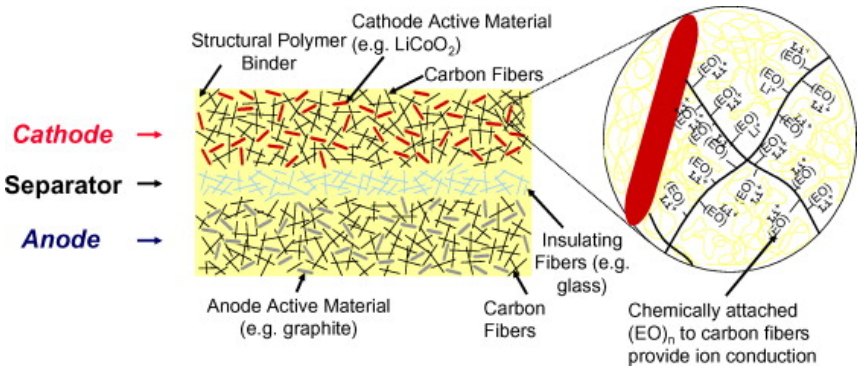

Figure 2.26: Structural battery composite fabrication, showing the steps: battery component manufacture, pouch-cell manufacture, and curing of the SBE. Reproduced from [111].

In this study, a high molecular weight poly(vinylindene fluoride) (PVDF, from Aldrich) was utilized as binder to connect all the components of the battery. The cathode was fabricated by adding carbon nanofibers (from Pyrograf Products), which acted as both a conducting diluent and a structural component, carbon black, and $LiCoO_2$ to the PVDF. The final composition consisted of 2 % carbon black, 11.5 % carbon nanofiber, 35 % $LiCoO_2$, and 51.5 % PVDF. Similarly, the anode was manufactured with Gi as the active material, and the carbon nanofiber was solely used as a structural component.

Liu *et al.* noted that the most challenging component to fabricate was the structural electrolyte. As it acted as a separator in the solid-state electrolyte, no physical separator was present. Therefore, the electrolyte was produced by blending PVDF with poly(ethylene glycol) dimethacrylate (PEGDMA, from Aldrich), which formed a polymer gel electrolyte with a $LiPF_6$ solution. Insulating fibers were added to reinforce the separator region and, modified polyethylene oxide $(EO)_n$ was also included to ensure high ionic conductivity, as well as good chemical and mechanical compatibility with PVDF.

The mechanical properties of the complete battery were tested using the three-point bending technique, and a Young's modulus of 3.1 GPa was achieved. The electrochemical performance resulted in a specific energy of 35 Wh/kg at 0.05 C.

Thus far, all the SBs discussed are laminated batteries, where the separator, cathode, and anode components are assembled by stacking them on top of each other. However, a novel design was proposed by Carlson [113] in his doctoral thesis, which deviates from the traditional stacking approach by adopting a more 3D approach. **Figure 2.27** depicts a close-up view of the cross-sectional area of the battery developed.

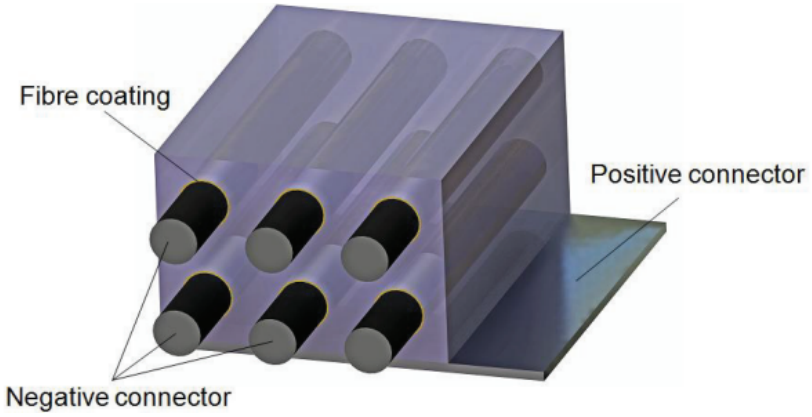

Figure 2.27: A schematic diagram depicting a cross-sectional view of the 3D battery is presented, with the carbon fibers coated with electrolyte in the cathode slurry being discernible. Reproduced from [113].

Similar to the previously presented work, Carson's battery also lacks a physical separator. The negative electrode is comprised of carbon fibers (from Toho Tenax Europe GmbH), consisting of approximately one thousand fibers, that are coated with a solid polymer electrolyte, namely methoxy polyethylene glycol 350 methacrylate (from Sartomer Europe), which is incorporated into a common cathode-doped matrix material. Even though Carson did not provide results of the mechanical and electrochemical properties of his SB, a review conducted by Asp and Greenhalgh [125] suggests that his battery attained a specific energy of 10 Wh/kg, and with a better dispersion of the positive electrode, an energy density of 175 Wh/kg, and a shear modulus of 1 GPa can be achievable.

The previous studies focused on SBs that employ CF as reinforcement and utilize LIB chemistry. This choice is driven by the existing practice of using CF as a negative electrode material in traditional LIBs. However, it's worth noting that there are also non-LIB batteries that incorporate CF as a reinforcement material.

2.3.2.2 Carbon Fiber Reinforcement and Non Lithium-Ion Chemistry

Huang *et al.* [115] proposed an alternative chemistry for SBs, Li-S, which was the first reported Li-S SB. In this battery, CF (from FibreGlast Development Corp.) was used as the

reinforcement material, and the electrodes were prepared via an electrodeposition-like mechanism. Prior to adding the cathode active material to the CF, the CFs were subjected to heating at 500 °C for 2 h in air to remove sizing agents and enhance the electrochemical performance while maintaining good mechanical properties. The CFs were then soaked in polysulfide catholyte (from Sigma-Aldrich) and electrodeposited with Li_2S (from Alfa Aesar).

The CFs used for the anode also underwent a similar process but were heated at 450 °C for 15 min to promote their lithophilic property. Lithium metal was infiltrated into the CFs, with excess lithium metal added to mitigate the loss in mechanical properties resulting from inevitable Li insertion. The excess lithium metal acted as a glue to secure the lithiated carbon fibers together, thereby preserving the mechanical strength of the anode. Instead of using a standard separator, a new separator with improved mechanical, thermal, and electrochemical performance was developed in comparison to conventional separators. This separator consisted of boron nitride (BN, from Graphene Supermarket Inc.) nanosheets combined with PVDF (from Arkema Inc.). A schematic representation of the SB is depicted in **Figure 2.28**.

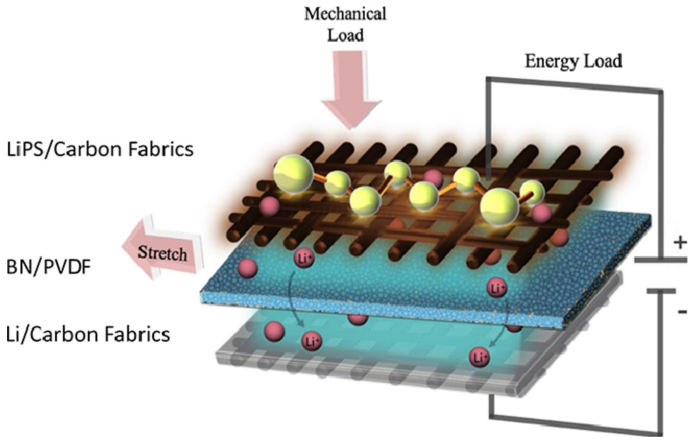

Figure 2.28: Schematic diagram of the structural lithium-sulfur battery. The mechanically robust Li-S battery consists of lithium/carbon fabrics anode, functional BN/PVDF separator and carbon fabrics/polysulfide cathode, which has a great advantage at bearing mechanical stress. Reproduced from [115].

The Li-S SB developed by Huang *et al.* demonstrated impressive electrochemical performance with a specific energy of 43 Wh/kg and initial specific capacity of 1266 mAh/g at 0.2 C, while also exhibiting a capacity retention of 81 % after 200 cycles at the same discharge rate.

To compare the performance of the SB with that of a regular Li-S battery produced by the same group, they conducted electrochemical tests, as illustrated in **Figure 2.29**. Notably, the capacity retention of the SB at 0.2 C was found to be significantly higher than that of the regular cell, as shown in **Figure 2.29a**. As the discharge rate increased, the difference in specific capacity between the SB and the regular cell grew, reaching nearly eight times

higher for the SB at 1 C, as seen in **Figure 2.29b**.

An electrochemical analysis under load was also conducted, as depicted in **Figure 2.29c**. The results demonstrate that even under a load of 20 MPa, the SB retained a capacity of more than 800 mAh/g, and it partially recovered its capacity when unloaded.

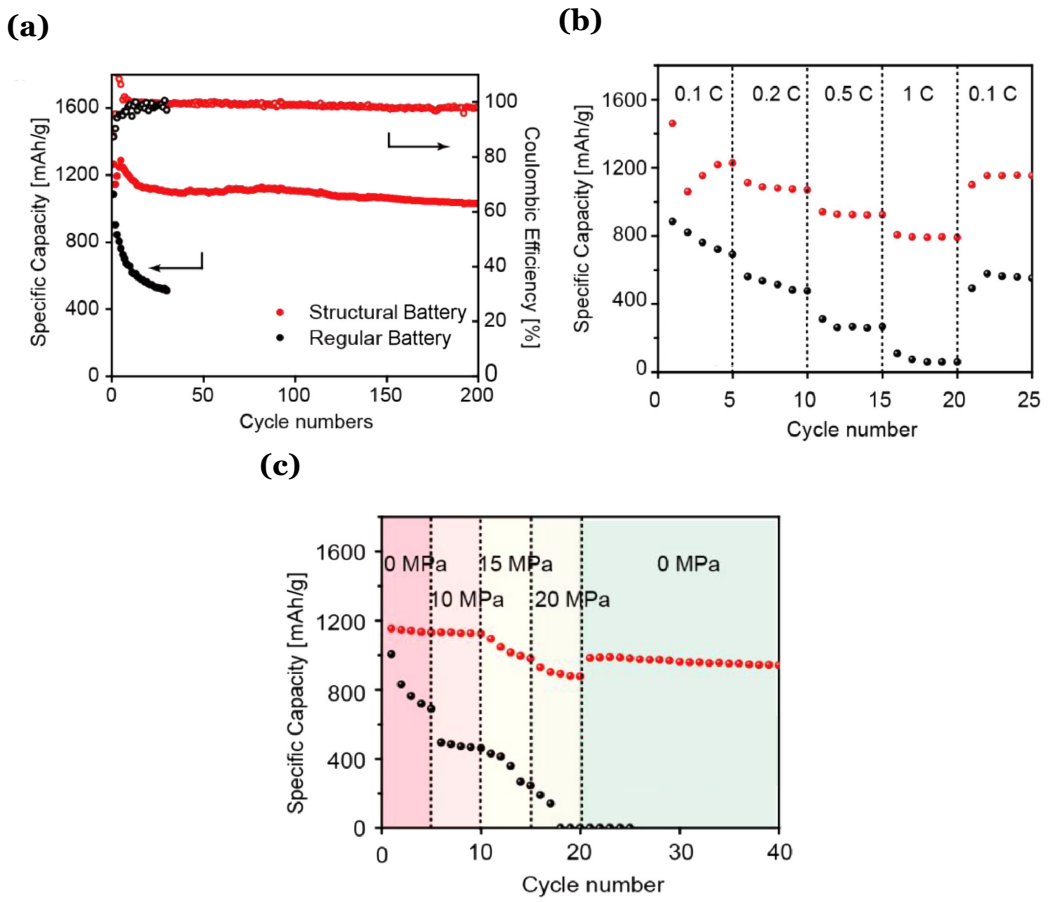

Figure 2.29: The comparison of cycling performance of the optimized structural battery and the regular battery at (a) 0.2 C and (b) different C-rates. (c) The electrochemical performance of the two batteries at various compressive stresses. Adapted from [115].

Another SB with and alternative chemistry was conceived by Liu *et al.* [107], who designed a zinc-ion SB that employed CF-reinforced laminates for enhancing the structural integrity of the battery.

The cathode of the SB comprised CF-coated MnO_2 (from Toray) which was made by mixing MnO_2, PVDF, and acetylene black in a mass ratio of 1:2:7 with N-methylpyrrolidone (NMP). The mixture was cured at 80 °C for 10 hours. The anode was a zinc sheet, and the separator was a Whatman GF soaked in a liquid electrolyte consisting of 2 M $ZnSO_4$+0.2 M $MnSO_4$.

To fabricate the SB, the vacuum infusion layup process is utilized. Two plies of CF and one ply of GF are impregnated with epoxy resin and utilized as the structural component, with CF serving as the primary reinforcement material. The layup of the Zn SB is illustrated

in **Figure 2.30**, with the following layers: 2CF/GF/Zn/Whatman GF/MnO_2/GF/2CF. The pure Zn sheet and MnO_2 electrode have a Cu foil and stainless steel tab attached, respectively. The SB is then cured in vacuum for 2 hours.

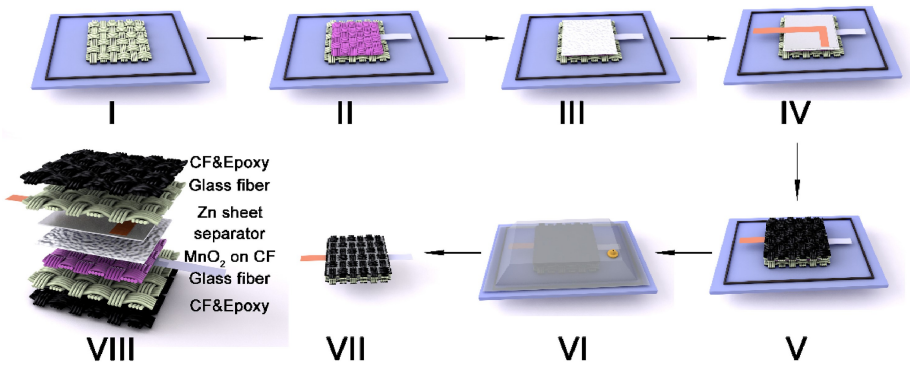

Figure 2.30: The illustration of the fabrication process of the Zn-ion structural battery: (I–V) the process of battery layup; (VI) vacuum infusion process; (VII and VIII) a scheme displaying the stacking of the individual layers of the Zn-ion structural battery and a picture of these layers cured into a composite material. Reproduced from [107].

To evaluate the mechanical performance of their Zn-ion SB, Liu *et al.* [107] conducted tensile and compressive tests at a rate of 1 mm/min and a three-point bending test at 2 mm/min. The results of these tests are depicted in **Figure 2.31**. The tensile curve of the Zn-ion SB is presented in **Figure 2.31a**, which demonstrates that the SB achieved a tensile strength of 179.5 MPa and a Young's modulus of 3.05 GPa. **Figure 2.31b** shows the compression curve of the SB, which had a compression strength and compressive modulus of 179.0 MPa and 5.88 GPa, respectively. Finally, the three-point bending test results are displayed in **Figure 2.31c**, where the SB exhibited high flexural strength of 229.6 MPa and delivered a high flexural modulus of 12.88 GPa.

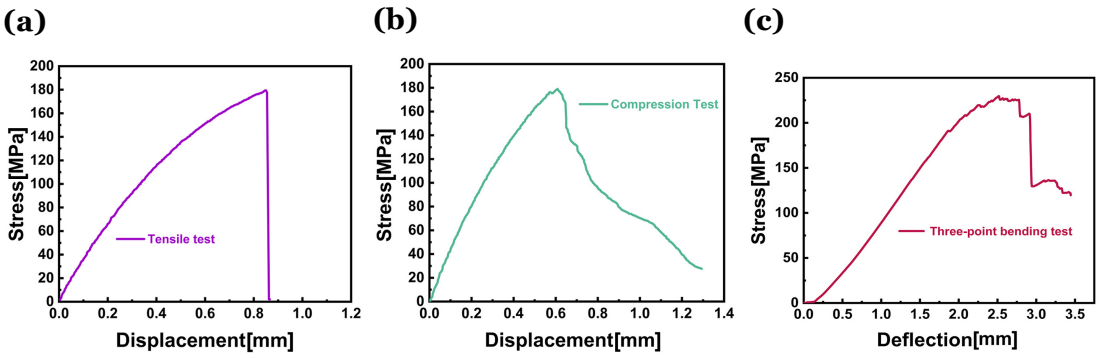

Figure 2.31: (a) Tensile test at 1 mm/min. (b) Compress test at 1 mm/min. (c) Three-point bend test at 2 mm/min. Adapted from [107].

The electrochemical performance of the Zn-ion SB developed by Liu *et al.* [107] was evaluated by subjecting it to a series of charge discharge cycles. The rate capability of the battery was investigated and the results are illustrated in **Figure 2.32a**. At a current density of 0.5 A/g, an average specific capacity of approximately 130 mAh/g was achieved. Even at

a higher rate of 2 A/g, the specific capacity remained relatively high at 77 mAh/g. The corresponding voltage profiles at various specific currents, ranging from 0.1 to 2 A/g, are demonstrated in **Figure 2.32b**.

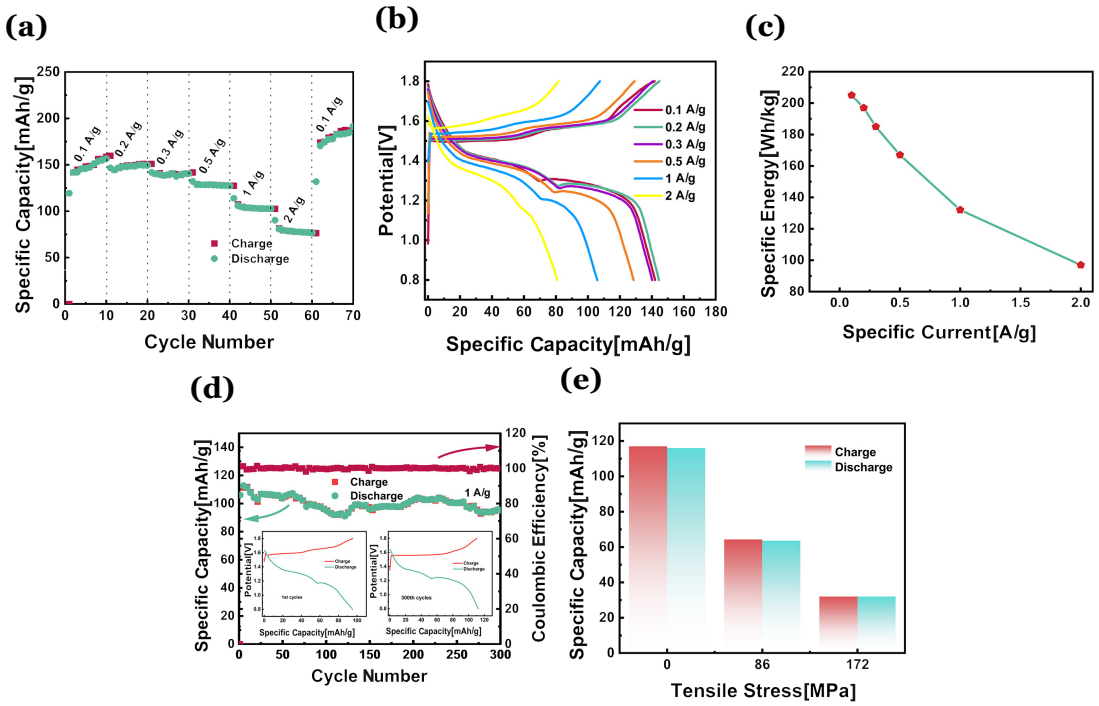

Figure 2.32: Electrochemical performance of Zn-ion structural battery:(a) Rate performance from 0.1 to 2 A/g. (b) The corresponding voltage profiles. (c) Corresponding specific currents. (d) Cyling test at 1 A/g for 300 cycles and corresponding voltage profiles at 1st and 300th. (d) Specific capacity at different tensile stresses. Adapted from [107].

Furthermore, in **Figure 2.32c**, the specific energy achieved at different specific currents is displayed, demonstrating a specific energy of 205 Wh/kg at 0.1 A/g and a specific energy of 97 Wh/kg at 2 A/g. The battery's cycling stability was analyzed, and even after 300 cycles, a specific capacity retention of about 85.3 % was obtained, along with a high Coulombic efficiency close to 100 %, indicating relatively better cycling stability, as shown in **Figure 2.32d**. The in situ electrochemical-mechanical results, obtained from galvanostatic charge-discharge cycles at 1 A/g under tensile testing at a speed of 1 mm/min, are presented in **Figure 2.32e**. The results showed a significant decrease in specific capacity with an increase in stress.

The previous studies examined were all linked to structural batteries, where the electrochemical components have the ability to bear mechanical loads, utilizing CF as at least one current collector/electrode and reinforcement for the structural battery. This is because, in order to utilize them as cathodes, active cathode materials must be applied to the CFs first to make them usable [20].

Numerous investigations [126,127] have been undertaken to evaluate the mechanical and electrochemical characteristics of CFs in the context of structural batteries. However, a

challenge arises when employing CFs as current collectors, as the introduction of ions during processes like lithium intercalation induces elastic strains in the CFs, leading to inherent tensile stress and a subsequent reduction in their maximum tensile strength. This issue has been more extensively discussed in some comprehensive reviews [19, 20, 125].

However there are other ways to improve the structural strength of coupled SBs without the use of CF. Some of the following are hard to be applied to aeronautical sector, so they won't be very deeply reviewed.

2.3.2.3 Non Carbon Fiber Reinforcement and Lithium-Ion Chemistry

Chen *et al.* [116] conducted a study where they utilized the change in shape of a battery to enhance its mechanical properties. They devised a flexible LIB that emulates the behavior of a human joint. To achieve this, they employed a conventional Gi anode/separator/LCO cathode with Al and Cu current collectors stack, which was divided into interconnected segments. Each segment was then folded in half, after which they could be wound into thick stacks having cubic shapes. The junction comprised two thick rigid stacks and a soft part. Notably, the thick stacks were designed with a cambered surface, which emulates the articular caput of bones, enabling them to buffer stress and provide the primary capacity of the flexible battery. The soft part acted as the ligament, interconnecting the thick rigid stacks, and imparting flexibility to the battery. By changing the winding methods, the battery with cylinder or triangular-shaped units could be fabricated, enabling the realization of specific deformations. A detailed illustration of this process and different shapes is shown in **Figure 2.33**.

The authors conducted mechanical simulation analysis to evaluate the performance of their design, which demonstrated that it could provide excellent flexibility while avoiding plastic deformation of the metal current collectors. The cubic, cylindrical, and triangular prism-shaped units achieved a Young's modulus of approximately 3.2 GPa, 3.2 GPa, and 4 GPa, respectively. Furthermore they achieved a energy density of 372 Wh/L, and even after 100 000 dynamic bending cycles, stretching and twisting the battery was able to retain more than 85 % of the capacity.

Although the use of these SBs for vehicle structures is unlikely, the findings showed that improving the mechanical performance of batteries is not limited to the use of composites alone. The study emphasized the possibility of making minor changes to existing materials while incorporating composite materials to create durable and robust SBs. As a result, the research broadens the possibilities for designing and developing advanced structural materials beyond the conventional use of composites, potentially leading to structural battery innovations.

Jin *et al.* [117] proposed an alternative approach for developing mechanically robust bat-

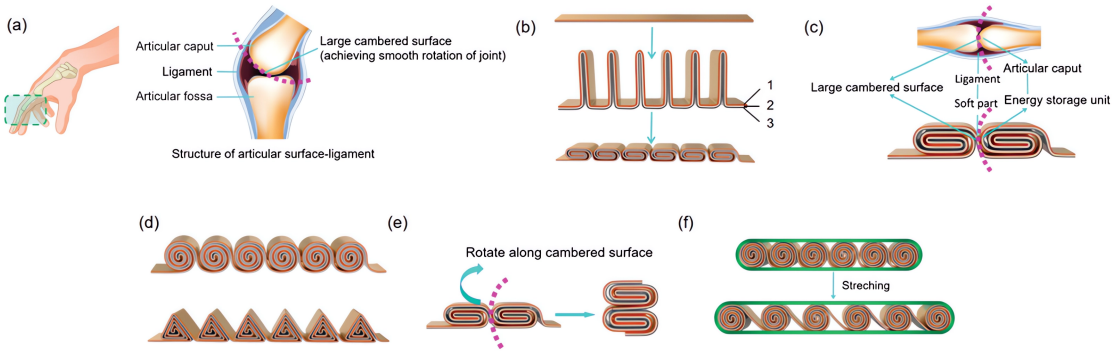

Figure 2.33: (a) The intricate structure of an articular surface-ligament system, which showcases the distinctive design elements of the ligament connection and the cambered articular caput surface, both crucial for achieving flexibility. (b) The structure and fabrication process of the flexible batteries, with the anode, separator, and cathode designated as 1, 2, and 3, respectively. (c) The thicker electrode stack corresponds to the bone, the unwound part to the ligament, and the larger cambered surface to the joint. (d) The structures of the flexible batteries with cylindrical and triangular prism-shaped units. (e) The folding schematic of the battery with cubic units. (f) The stretching deformation experienced by a battery with cylindrical units. Reproduced from [116].

teries inspired by the structure of trees, which immobilize soil and themselves against strong winds. The authors analogized the tree and the soil to the separator and granular electrode, respectively, while the shear stress introduced by bending deformation was equivalent to wind. The mechanical stability of trees is attributed to their deep and strong root networks, which hold the soil firmly. To mimic this feature, the authors infiltrated a polymeric binding material, poly(vinylidene fluoride-co-hexafluoropropylene) P(VDF-HFP), into the porous cathode and anode, thereby forming a continuous network, as depicted in **Figure 2.34a**. The composite anode and cathodes were subsequently laminated onto a ceramic-coated separator by hot-pressing, as shown in **Figure 2.34b**. This proposed approach offers a promising alternative for developing mechanically robust batteries.

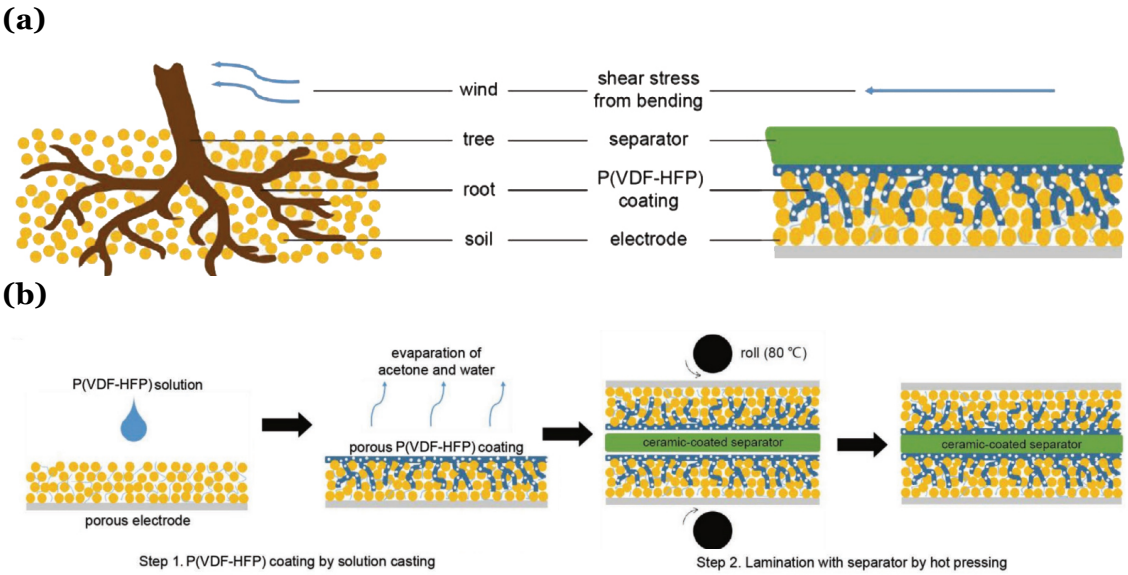

Figure 2.34: (a) The analogy between a tree against strong wind (left) and the electrode/separator adhesion against shearing introduced by bending (right). (b) A schematic of the fabrication process of a structural cell with tree-root-like interfaces through hot pressing. Adapted from [117].

From the process presented in **Figure 2.34b**, it is apparent that the binder network, inspired by the tree-root structure, results in strong bonding between the separator and the powder-based electrode, leading to a significant increase in the flexural modulus of the structural battery.

The SB developed by Jin *et al.* employed Gi as the anode, NMC as the cathode, and a 1 M $LiF_2BC_2O_4$ and 0.4 M $LiBF_4$ solution as the electrolyte. To evaluate the mechanical properties of their design, they compared it to a conventional LIB and a LIB with both electrodes replaced by CF. The common LIB exhibited a flexural modulus of 281 MPa, while the LIB with CF displayed a significant increase to 1.38 GPa. However, the SB with polymeric binder exhibited an eleven-fold improvement in flexural modulus over the common LIB, resulting in a value of 3.1 GPa, even surpassing the LIB with CF and with only a 3 % loss in specific energy. Further analysis utilizing information found in the supplementary materials and article made it possible to estimated a specific energy of 156.1 Wh/kg. Moreover, the SB exhibited a specific capacity of 148.6 mAh/g at 0.5 C and a high capacity retention of 95.5 % after 500 cycles.

Their finds reveal a viable alternative approach to improving battery robustness that does not rely on carbon fibers. Notably, the use of polymeric binders provides a feasible way to supplement or even combine with carbon fibers to improve structural battery performance even further.

2.3.2.4 Non Carbon Fiber Reinforcement and Non Lithium-Ion Chemistry

In addition to SBs that utilize CF or Li-ion chemistry, there exist other coupled SBs that do not rely on these components. An exemplar of this type of SB is one that employs Zn^{+2} as the electrolyte, as developed by Wang *et al.* [118]. To achieve this, they created a novel solid-state electrolyte consisting of branched aramid nanofibers (BANFs) that mimics the fibrous structure of articular cartilage. This innovative electrolyte was composed of poly(ethyleneoxide) (PEO, from Sigma-Aldrich) and $Zn(CF_3SO_3)_2$ (from Sigma-Aldrich) as the ion-transport components, with BANFs serving as the structural component. The weight ratio of the components was 9:3:1, respectively.

The cathode material layer was comprised of 80 wt% MnO_2, 10 wt% Gi (from Sigma Aldrich), and 10 wt% PEO polymer binder. On the other hand, the anode layer was composed of a Zn foil (purchased from Sigma Aldrich). Results of the mechanical analysis revealed that the tensile modulus of the SB was seven times higher compared to composite films based on aligned cellulose fibers and CNTs. Electrochemical analysis revealed capacities of 146.2, 129.5, 106.7, and 89.2 mAh/g at 0.1, 0.2, 0.5, and 1.0 C, respectively. Additionally, the SB retained 96 % of its capacity after 50 cycles, and the coulombic efficiency was approximately 100 % for the initial 50 cycles and 96 % at the 100th cycle. Galvanostatic charge discharge cycles and the rate capability of the SB at different C-rates are presented in **Figure 2.35a** and **Figure 2.35b**, respectively, which are related to the values presented before. Using the provided data, an approximation of the battery's specific energy yielded a value of 190 Wh/kg.

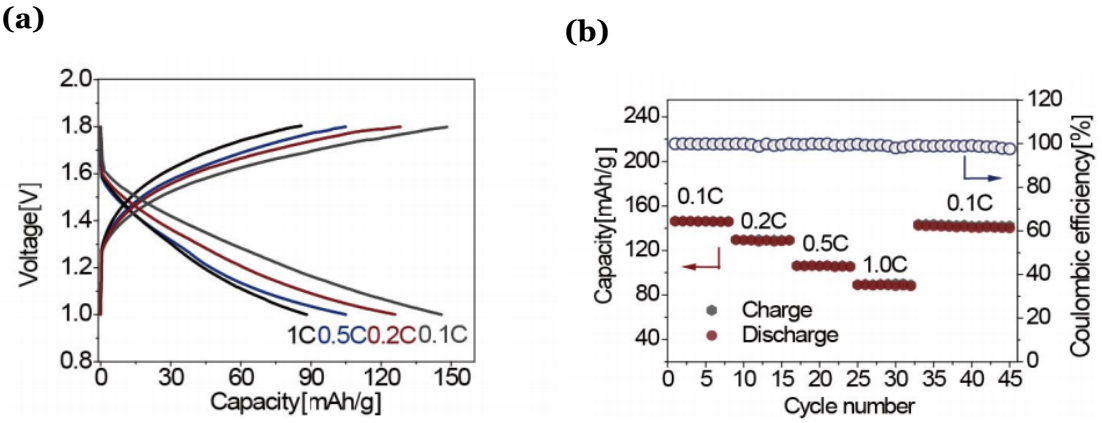

Figure 2.35: (a) Galvanostatic charge discharge curves and (b) rate capability of the Zn structural battery battery cycling within the voltage range of 1 V-1.8 V at current density from 0.1 C to 1.0 C (1 C = 150 mA/g). Adapted from [118].

In addition, the practical implementation of the SB in load-bearing and energy storage components of several small UAVs, is demonstrated in **Figure 2.36**. This successful application highlights the potential of Zn-based materials as an alternative to Li-ion for use in structural batteries. The unique shape of the SB, resulting from the high deformation tolerance of the constituent materials, is readily apparent in **Figure 2.36**, while remain-

ing functional and safe. This highly desirable property of SBs makes them an attractive option for a variety of applications.

Figure 2.36: Corrugated Zn/MnO_2 battery pack design as a replacement for the original device cover to support UAVs' main power source. Reproduced from [118].

Meng *et al.* [119] proposed an alternative approach for the development of SBs, utilizing a Ni-Fe chemistry and a stainless steel mesh as the primary structural support. The battery was composed of a solid-state ion-conducting matrix as the electrolyte, with the electrodes fabricated by growing CNTs onto the stainless steel mesh using chemical vapor deposition. Oxides/hydroxides of Fe and Ni were then deposited onto the CNT surfaces to produce the anode and cathode, respectively. The composite was assembled using a wet lay-up process with a potassium hydroxide–poly(vinyl alcohol) (PVA-KOH) gel, which formed the solid-state ion-conducting matrix. To serve as the separator, two types of materials were used, GF and Kevlar® (aramid fiber). A schematic of their SB is shown in **Figure 2.37**. The CNTs played a crucial role in reinforcing the composite and structurally interconnecting the electrolyte matrix, the active material, and the structural frame.

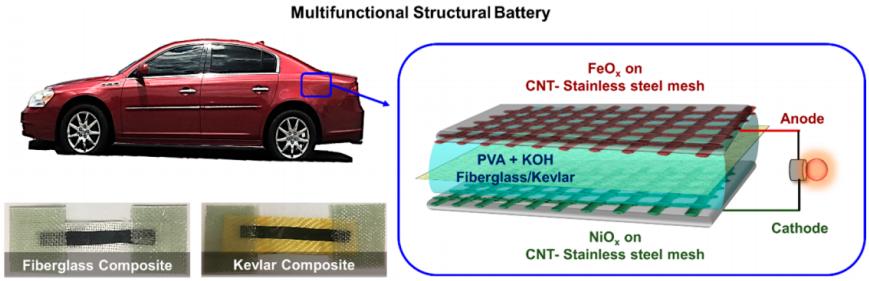

Figure 2.37: Schematic representation of a multifunctional structural battery using fiberglass or Kevlar® as the separator between the active battery materials. Adapted from [119].

Through the implementation of cyclic voltammetry and galvanostatic charge discharge tests, the electrochemical performance of the battery was assessed. The most favorable outcomes were achieved by employing GF as the separator for the SB. Specifically, the GF separator yielded a peak energy of 1.4 Wh/kg at power densities of 29 W/kg and 0.290

Wh/kg at 170 W/kg. These values were based on the combined mass of all the components within the composite.

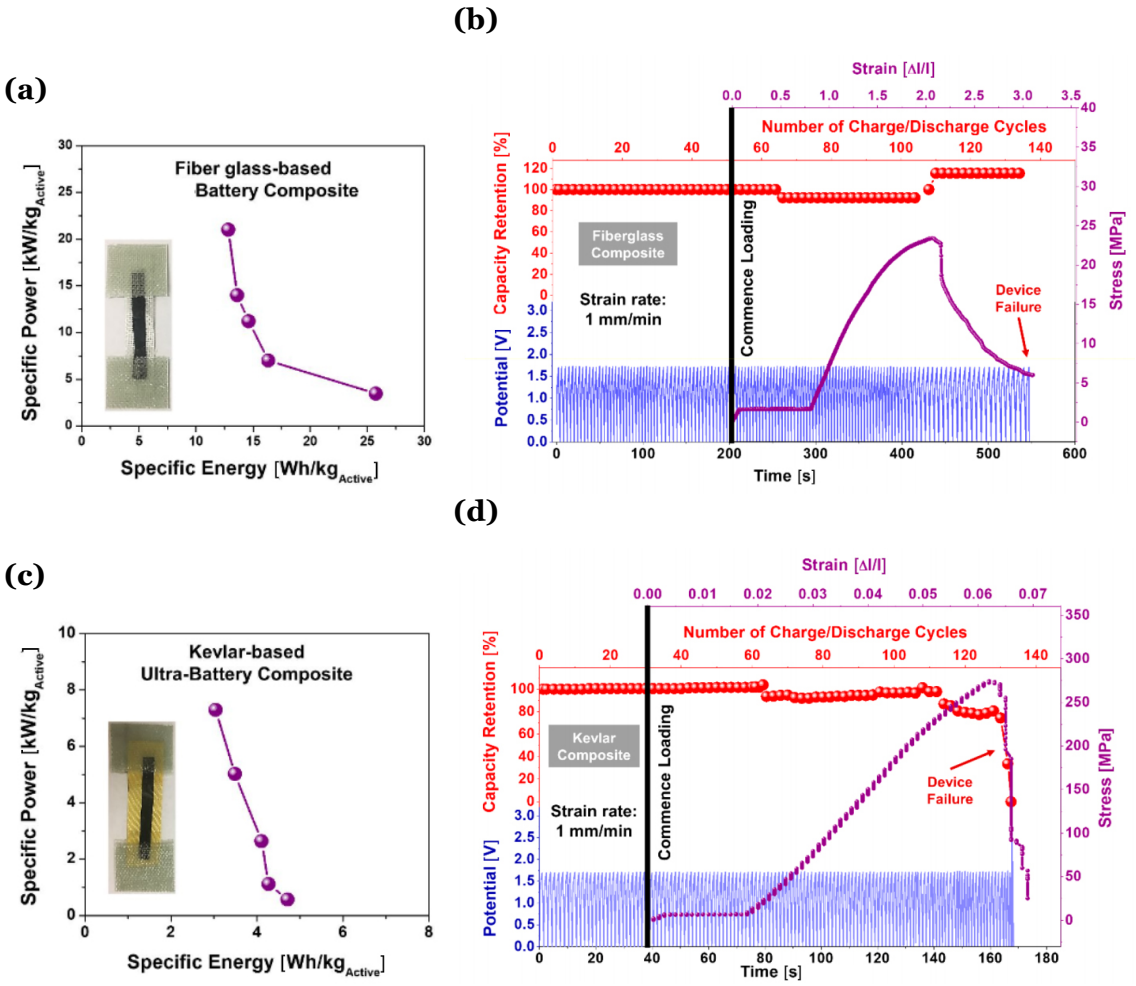

Figure 2.38: Specific energy and power of the fiber glass-based (a) and of the kevlar-based (c) Ni-Fe structural battery based on total active mass.In situ mechano-electrochemical measurements of the fiberglass (b) and Kevlar® (d) composite during simultaneous charge–discharge measurements along with dynamic tensile tests. Adapted from [119].

The specific energy and power outputs of the SB are plotted in **Figures 2.38a** and **Figure 2.38c**, respectively, using GF and Kevlar® as separators for the active material. Notably, the specific energy and power output were observed to be two to three times higher in the GF case compared to that of its Kevlar® counterpart. This was attributed to GF's comparatively lower internal resistance.

Regarding mechanical performance, the Kevlar® SB exhibited superior results, manifesting an ultimate tensile strength of approximately 280 MPa and a Young's modulus of 7.3 GPa. These properties were evaluated by subjecting the samples to tensile stresses at a rate of 1 mm/min, while concurrently undergoing galvanostatic charge-discharge cycles. **Figure 2.38b** and **Figure 2.38d** illustrate the results for the GF and Kevlar® separators, respectively.

As evidenced by the figures, the ultimate tensile strength of the GF separator was ten times lower than that of Kevlar®. However, it is intriguing to note that the capacity retention of the GF separator increased after the ultimate tensile strength was reached, while that of the Kevlar® separator substantially decreased. This discrepancy can be attributed to the more abrupt and inflexible failure of the Kevlar, whereas the GF exhibited a more plastic behavior.

Danzi *et al.* [114] designed a solid-state coaxial SB distinct from the SBs previously presented. It employs a sodium-based electrolyte rather than the traditional lithium-based electrolyte used in LIBs. The use of a sodium-based electrolyte has the advantage of being safer, homogeneous, and non-flammable, lowering the risk of thermal runaway. Furthermore, the coaxial design allows for high capacitance while maintaining good mechanical performance by reducing the possibility of delamination.

It is worth noting, as depicted in **Figure 2.39a**, that the solid-state coaxial SB is composed of three primary components. The first component is the carbon fiber reinforced polymer (CFRP, from BTPT) cylindrical shell, which houses the Cu foil (from Alfa Aesar) that serves as the precathode and current collector. The second component is an all-solid-state sodium-based electrolyte, and the third component is an aluminum coaxial anode/current collector which also gives structural integrity to the battery. The CFRP shell not only provides critical structural support to the battery, but it also protects the battery components from potential external damage.

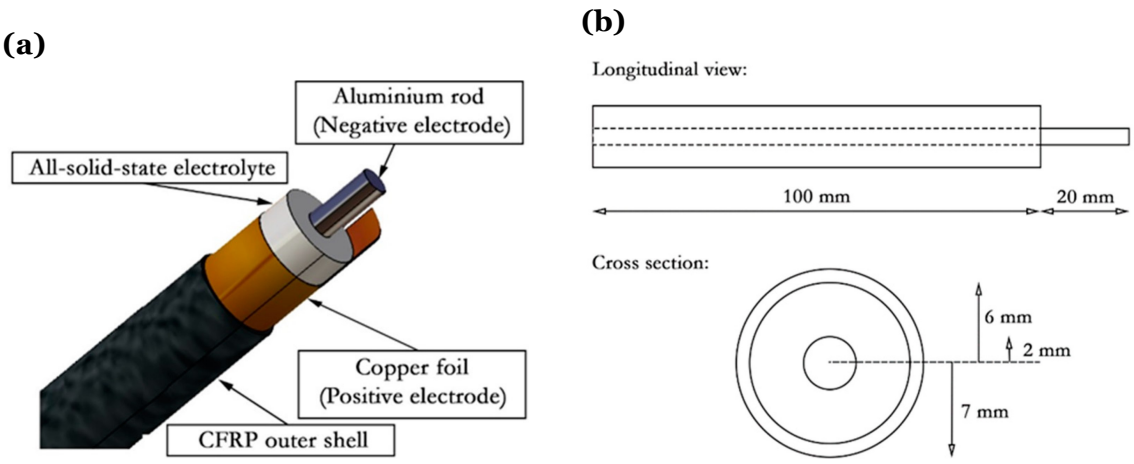

Figure 2.39: Coaxial structural battery design; (a) main components, (b) views with dimensions. The coaxial structural battery is composed of an external carbon fiber reinforced shell co-cured with a copper film that works as the positive electrode, a sodium-based all-solid-state electrolyte, and an aluminum rod as the negative electrode. Reproduced from [114].

The solid-state coaxial SB was built sequentially, with each component manufactured separately. To begin, the CFRP and Cu foil were co-cured in a hot press for 9 hours at 80 °C, while the electrolyte was made by mixing commercial precursors with deionized water before reacting and drying at 230 to 250 °C. The electrolyte that resulted was then solid-

ified and ground into powder. Once all the components were made, the aluminum rod was placed in the middle of the CFRP/Cu, and the space between them was filled with the electrolyte.

The final dimensions and configuration of the SB are depicted in **Figure 2.39b**, highlighting the possibility of customizing the battery dimensions to suit various applications. Thus, making it a versatile option for structural battery design.

Using cyclic voltammetry, the electrochemical performance of the solid-state coaxial SB was evaluated, achieving a specific energy of 38 Wh/kg and an energy density of 56.2 Wh/L. A three-point bending test was used to evaluate the battery's mechanical performance, yielding a peak load of 1.87 kN. **Figure 2.40** shows the behavior of the SB in comparison to only the CFRP outer shell. To assess the electrochemical performance under load, during the three-point bending test, a LED was connected to the SB and remained lit until the SB reached a maximum displacement of 16 mm. From the data provided, it was possible to estimate a Young's modulus of 6.5 GPa.

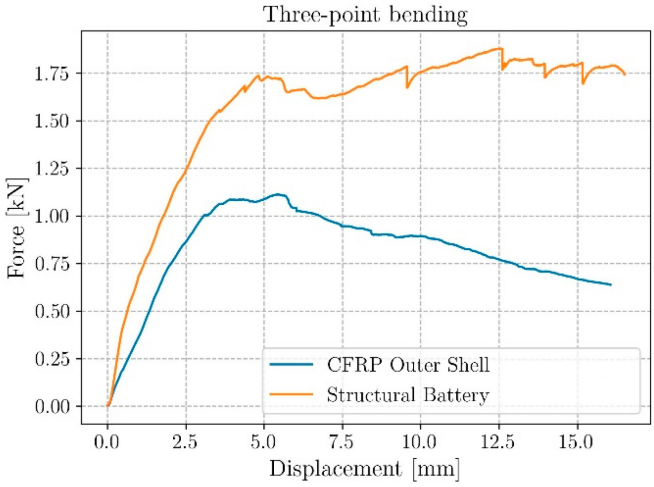

Figure 2.40: Three-point bending test, force vs. displacement curves for a structural battery and the CFRP outer shell only. Reproduced from [114].

2.3.3 Decoupled Structural Batteries

The preceding literature surveyed showcased coupled SBs, some of which demonstrated favorable electrochemical and mechanical outcomes, while others displayed solely one of these attributes. In this subsection, decoupled SBs will be reviewed and categorized similarly.

2.3.3.1 Carbon Fiber Reinforcement and Lithium-Ion Chemistry

Fu *et al* [101] proposed a novel fiber metal laminated solid-state battery, which combines the benefits of high electrical conductivity and impact resistance of metal with those of fiber metal laminates, fibers/metal/fibers. The battery consists of modified Cu and Al current collectors, which possess superior mechanical properties in comparison to commonly used LIB current collectors. These current collectors are coated with active materials and a solid-state electrolyte, and are embedded between composite fibers, which serve as the main structural component.

The anode of the battery comprises of a Li layer modified Cu sheet (from Guangdong Canrd New Energy Technology Co.,Ltd.), while the cathode is made of an Al sheet coated with $LiFePO_4$ powder (from BTR New energy materials), carbon black (from MTI) and PVDF (from Arkema), with mass ratios of 8:1:1. The solid-state electrolyte is produced by dissolving poly(ethylene oxide)diacrylate (PEGDA), bisphenol A ethoxylate dimethacrylate (E2BADMA), and 2,2´-azobis(2-methylpropionitrile) (AIBN) initiator in a liquid electrolyte consisting of 1 M LiTFSI in a non-aqueous mixture (all from Macklin).

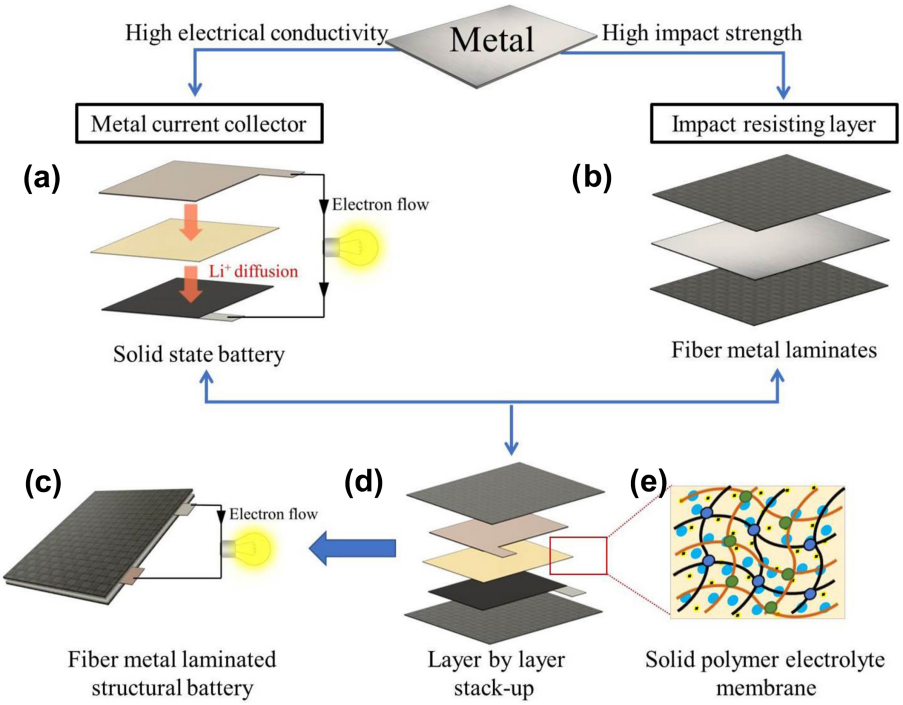

Figure 2.41: Integration design of structural battery based on multifunctionality of metal. (a) Stacking of the modified Al/Cu and the solid-state electrolyte. (b) Representation of a metal composite. (c) Representation of the structural battery, based on a metal composite where the metal is replaced by the battery components. (d) Stacking of all structural battery components. (e) Schematic of the solid-state electrolyte. Reproduced from [101].

The structural component of the battery was composed of CF (from Easy Composites) and GF (from Easy Composites), whereas the battery component was made of Cu/Al. The CF/GF/metal/GF/CF stack was assembled in the form of $[o_{CF}/o_{GF}/(Cu/Al)]_S$, and sub-

sequently cured to yield the CF/GF/metal/GF/CF solid-state battery. The schematic representation of Fu's solid-state battery, along with its implementation process, is depicted in **Figure 2.41**.

In their study, tensile testing was performed on three case studies: the previously described CF/GF/metal/GF/CF solid-state battery, a GF/metal/GF solid-state battery, and a modified Cu/Al battery embedded in an Al plastic film. The results are depicted in **Figure 2.42b**. Furthermore its performance was compared to a fiber reinforced polymer (FRP) similar to the SB but without the Cu and Al. The results are presented in **Figure 2.42a**.

It can be observed that while the modified Cu/Al exhibited some mechanical resistance, its ultimate tensile strength was less than 50 MPa. On the other hand, the GF/metal/GF solid-state battery demonstrated a tensile strength of 95 MPa, which increased to 523 MPa with the incorporation of CF, leading to a Young's modulus of 25.3 GPa. Furthermore compare to the pure FRP the mechanical performance is very similar. To assess the impact properties of these composites for automobile industries, impact testing was conducted on an SB with a configuration of $[\pm 45_{2CF}/0_{GF}/(\mathrm{Cu/Al})]_S$ and a similar FRP of -45/45 without Cu/Al. The results showed that for an impact with 30 J of energy, the FRP was penetrated with a damage area of 2.5 cm $\times$ 2.8 cm, while the SB remained unpenetrated and only exhibited minor crack lines. Moreover, the SB was still able to light up a LED. Further analysis by Lu et al. [101] concluded that this was due to the FRP absorbing all the energy, whereas the SB exhibited rebound.

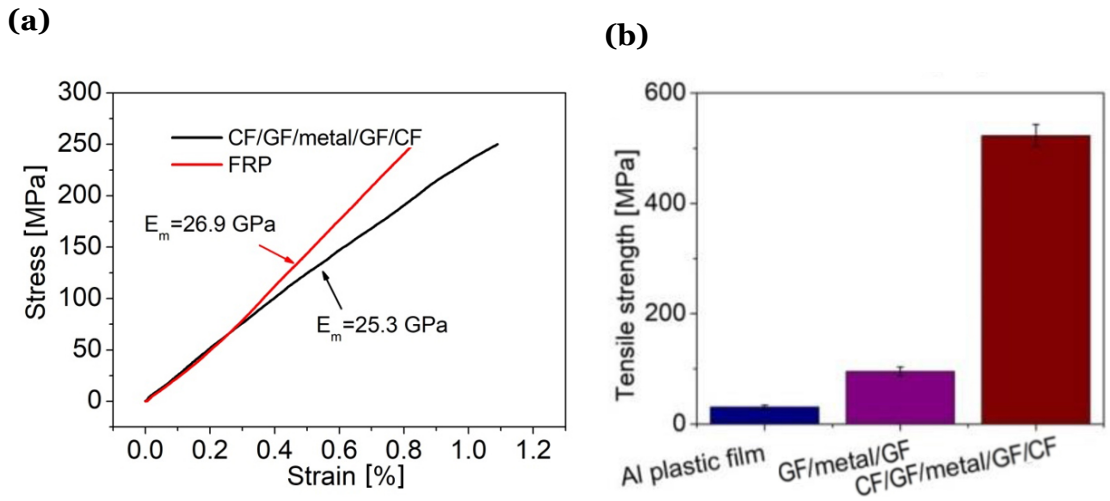

Figure 2.42: (a) Strain stress curve of fiber reinforced polymer and of the CF/GF/metal/GF/CF structural battery, with corresponding Young's modulus. (b) Ultimate tensile strength of the three evaluated case studies.Adapted from [101].

The electrochemical performance of the batteries was assessed by analyzing their voltage-capacity profiles and galvanostatic charge-discharge curves. From these analyses, as well as other available information, it was possible to estimate the specific energy to be 116.7 Wh/kg. In addition, the authors utilized a composite structure containing eight modified

Cu/Al batteries arranged in the same configuration as previously described to power a car. This battery system had a capacity of 0.011 Ah and was able to sustain the car's operation for 20 minutes. The configuration of the SB and the car powered by it are depicted in **Figure 2.43**.

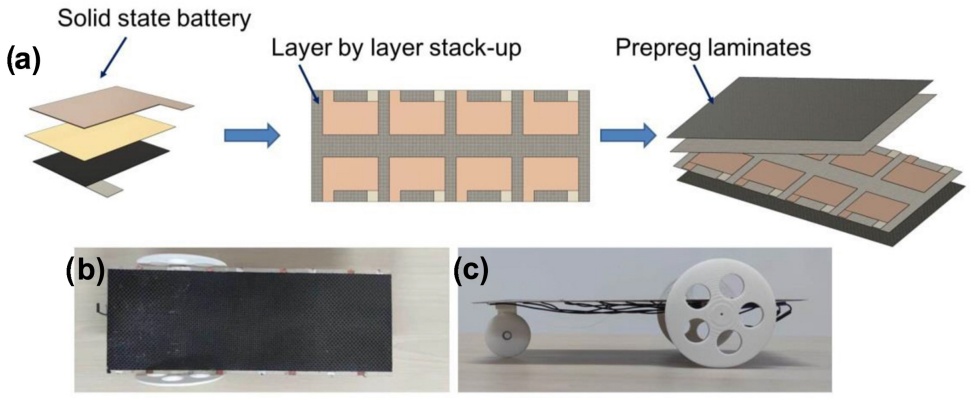

Figure 2.43: (a) Schematic illustration of the fabrication procedures for self-driven chassis. (b) The optical images of self-driven chassis taken from above. (c) The optical images of self-driven chassis taken from the side. Reproduced from [101].

Thomas *et al.* [104] employed a similar approach to develop a SB. They integrated various layers of polymer-lithium ion (PLI) bicell into woven carbon fiber and carbon-epoxy composites, as illustrated in **Figure 2.44**. The bicell consists of a $LiCoO_2$ cathode in an Al current collector, a Gi anode in a Cu current collector, and a microporous polyolefin separator. The active particles are consolidated by a P(VDF-HFP) polymer matrix, which also bonds the layers through a hot lamination process.

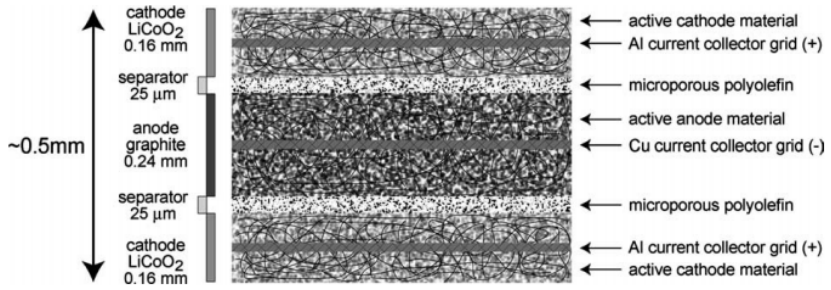

Figure 2.44: Structural batteries configurations. Reproduced from [104].

Thomas *et al.* [104] conducted an analysis of three SB configurations in their study. The first configuration consisted of a bicell core surrounded by packaging material. The second configuration incorporated woven CF layers (from Thornel) between the packaging and bicell core. The third configuration involved the addition of bonded carbon-epoxy layers (from Hercules Inc.) on the exterior of the packaging. These configurations are visually presented in **Figure 2.45**.

The authors conducted mechanical and electrochemical tests on the batteries with the intention of using them in an UAV wing structure of dimensions 30 cm length, 10 cm width,

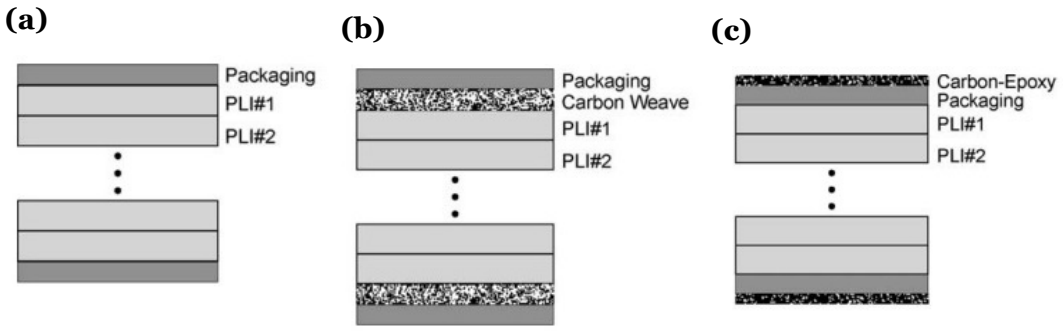

Figure 2.45: Structural batteries configurations. (a) Bicell core with outside packaging. (b) Woven CF layers between the packaging and bicell core. (c) Bonded carbon–epoxy. Reproduced from [104].

and 1.172 cm thickness. For this application, the SB comprised eight bicell layers with packaging and 0.36 cm thick reinforcement on the upper and lower sides of the core, thus achieving the desired thickness. The outcomes of the aforementioned tests are succinctly presented in **Table 2.7**.

Table 2.7: Summary of the findings of the electrochemical and mechanical test of Thomas *et al.* [104] work.

Configuration	Mass [g]	Specific Energy [Wh/kg]	Total Eenergy [Wh]	Young's Modulus[GPa]
Polymer-lithium ion bicell	N/D	165	N/D	1.02
Carbon–weave reinforced structural battery	458	119.5	54.7	4.07
Carbon–epoxy reinforced structural battery	575	95.2	54.7	8.39
Pure carbon-epoxy	387	N/D	N/D	9.89

Based on their results, they concluded that, for reinforcement thicknesses that are equal, carbon-epoxy has superior mechanical properties but inferior energetic properties, due to greater mass, when compared to carbon-weave. However, pure carbon-epoxy is lighter and stronger than both. To assess the effectiveness of their SB, they calculated the impact on the UAV's endurance by replacing the pure carbon-epoxy with the same dimensions as shown in **Table 2.7** wing structure and bicell battery, which had a total energy of 54.7 W/h, with the carbon-epoxy SB with the same dimensions and total energy. They found a 19 % increase in flight time.

The present example, while purely theoretical, serves as a demonstration of how multi-functional materials can enhance and quantify performance in specific systems, as also demonstrated in **Subsection 2.3.1**.

In a similar vein, Galos *et al.* [103] employed commercial LIBs (from LiPol Battery Co. Ltd) in a sandwich composite structure comprising CF sheets (from Colan Ltd) and a PVC

foam core (from Divinycell). Each LIB was enclosed within a protective aluminum pouch and featured a nominal capacity and voltage of 0.5 Ah and 3.7 V, respectively.

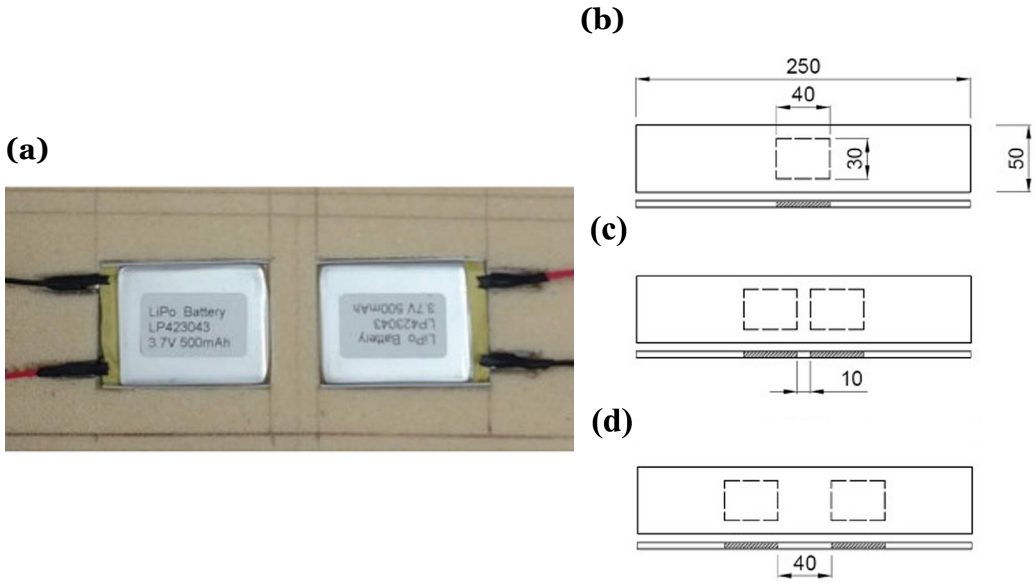

Figure 2.46: (a) Lithium-ion batteries incorporated in sandwich composite core foam (b) One lithium-ion battery. (c) Two lithium-ion battery with 10 mm spacing. (d) Two lithium-ion battery with 40 mm spacing. Reproduced from [103].

Prior to the insertion of the CF sheets, a segment of the foam core, of identical size to the battery, was removed as shown in **Figure 2.46a**. Two plies of carbon fabric were then applied to both surfaces of the foam core to produce the face sheets, which were subsequently cured at ambient temperature. For their investigation, Galos *et al.* examined three configurations: a single LIB integrated in the center of the composite, a dual LIB arrangement with a separation of 10 mm, and a dual LIB configuration with a separation of 40 mm, as illustrated in **Figure 2.46**.

The researchers conducted mechanical analysis through three-point bend tests, conducted at a rate of 2 mm/min. The outcomes indicated that the Young's modulus of the sandwich composite remained consistent when one or two batteries were present within the core. Specifically, the control composite with no batteries had a Young's modulus of 7.49 GPa, while the composite with one battery had a value of 6.98 GPa, and those with two batteries and spacing of 10 mm and 40 mm had values of 7.21 GPa and 7.41 GPa, respectively. However, the load-bearing capacity of the sandwich composite was affected when deformed beyond the elastic load limit. In the control composite, the load-bearing capacity showed an abrupt drop due to localized plastic yielding of the polymer foam core immediately beneath the load point. On the other hand, the SB with one battery and the one with two batteries with 10 mm spacing retained high load-bearing capacity since the plastic deformation was localized to the battery instead of the foam core. Moreover, the composite with two batteries and 10 mm spacing constrained the plastic deformation of the core because of the close proximity of the batteries. These findings are illustrated in **Figure 2.47a**.

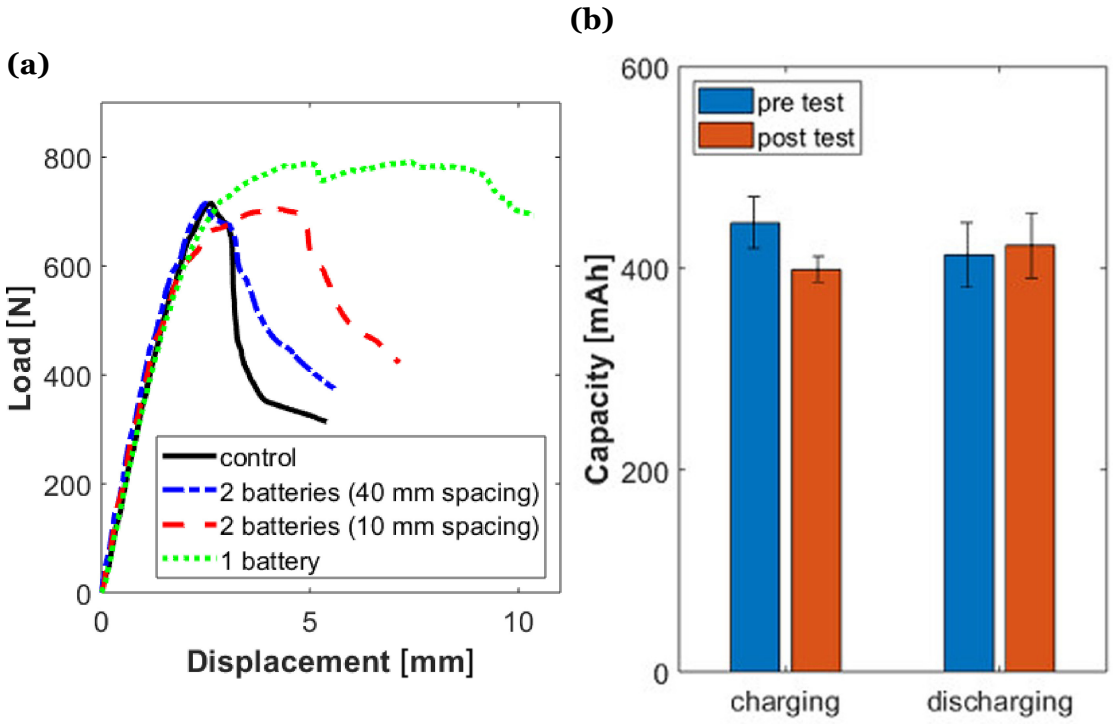

Figure 2.47: (a) Load-displacement curves for the sandwich composites in three-point bending (span length = 90 mm). (b) Cell capacity of a single lithium-ion battery embedded within the sandwich composite pre- and post-flexural testing (span length = 90 mm). Reproduced from [103].

In order to evaluate the electrochemical properties of the sandwich composites, they performed cyclic charge-discharge tests at a constant 1 C rate while under load. The specific energy of the sandwich composites with one and two batteries was found to be 43.4 Wh/kg and 71.7 Wh/kg, respectively, corresponding to energy densities of 26.9 Wh/L and 53.8 Wh/L. This is in contrast to the specific energy and energy density of the LIB, which were found to be 185 Wh/kg and 385 Wh/L, respectively. It is worth noting that the decrease in specific energy was more than half, but the energy density was seven times less in the best-case scenario, as the sandwich composites contained a significant amount of unused space. Despite this limitation, the sandwich composites exhibited promising results under load, as even after experiencing a load of 670 N, their loss in capacity was minimal, as shown in **Figure 2.47b**.

2.3.3.2 Non Carbon Fiber Reinforcement and Lithium-Ion Chemistry

Ladpli et al. [100] introduced a novel SB concept, where high-energy Li-ion battery electrode materials are integrated within high-strength CFRP composites. The primary reinforcement mechanism in this design involves through-thickness interlocking polymer "rivets" that extend through precisely engineered perforations within the battery stack. These rivets interlock the electrode layers and securely fasten them onto the structural CFRP facesheets. **Figure 2.48** visually depicts this innovative approach.

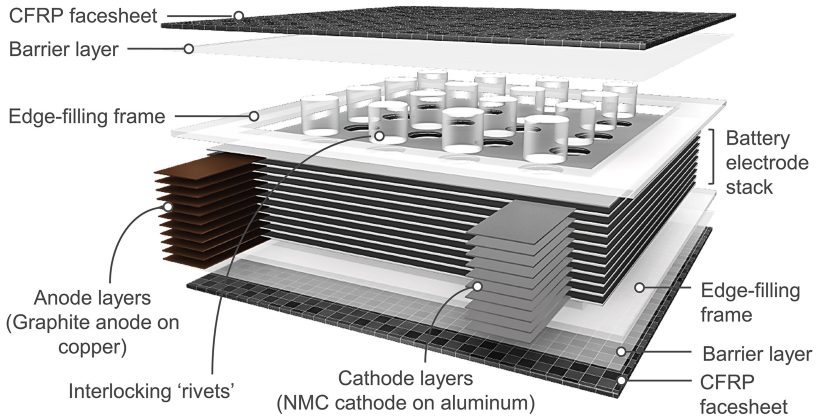

Figure 2.48: 3D schematic illustration of novel structural battery. An array of through-thickness rivets is used to interlock a stack of typical Li-ion battery electrodes three-dimensionally. These rivets are securely anchored on the encapsulating carbon fiber reinforced polymer (CFRP) facesheets, allowing the entire unit to act as a mechanically-efficient sandwich structure. Reproduced from [100].

The sandwich-style construction employed in this work effectively enhances the moment of inertia of the laminate, thereby resulting in higher flexural rigidity. Furthermore, the use of through-thickness interlocking polymer 'rivets' prevents delamination between the electrode layers and facilitates the transfer of shear stress through the battery stack to the CFRP facesheets. **Figure 2.48** illustrates the three main components of the sandwich battery which include the core battery electrode stack, the structural facesheets, and the reinforcement rivets.

The electrodes utilized in this study were made of commonly used materials for LIBs. Specifically, the anode was composed of Gi (from Farasis Energy, Inc.) on copper foil, while the cathode was made of NMC (from Farasis Energy, Inc.) on aluminum foil. The complete stack consisted of eleven anode and ten cathode layers. The separator was made of polyolefin (from Farasis Energy, Inc.), while the electrolyte was lithium-salt liquid electrolyte, $LiPF_6$, dissolved in an organic solvent (from Farasis Energy, Inc.).

The structural layer of the SB was composed of CF (from Toray) and used to manufacture the CFRP composites through a vacuum-assisted resin infusion process. Additionally, a thin barrier layer was bonded to the structural layer to passivate it. The barrier layer was made of the same polyethylene-co-acrylic-acid (EAA) ionomer thermoplastic (from Dupont) as that used for the rivets. This design allowed the rivets to be firmly bonded to the facesheets, while simultaneously serving as an encapsulation layer for the electrochemical cell. The assembly process of the SB is illustrated in **Figure 2.49**.

In their study, four different case studies were investigated, including a pouch cell without any reinforcement, a SB reinforced with CFRP, and two SBs with rivets in a 4×4 array and in a 5×5 array. The properties of each case study are summarized in **Table 2.8**.

The findings revealed that the capacity obtained for the SBs fell slightly below the theoreti-

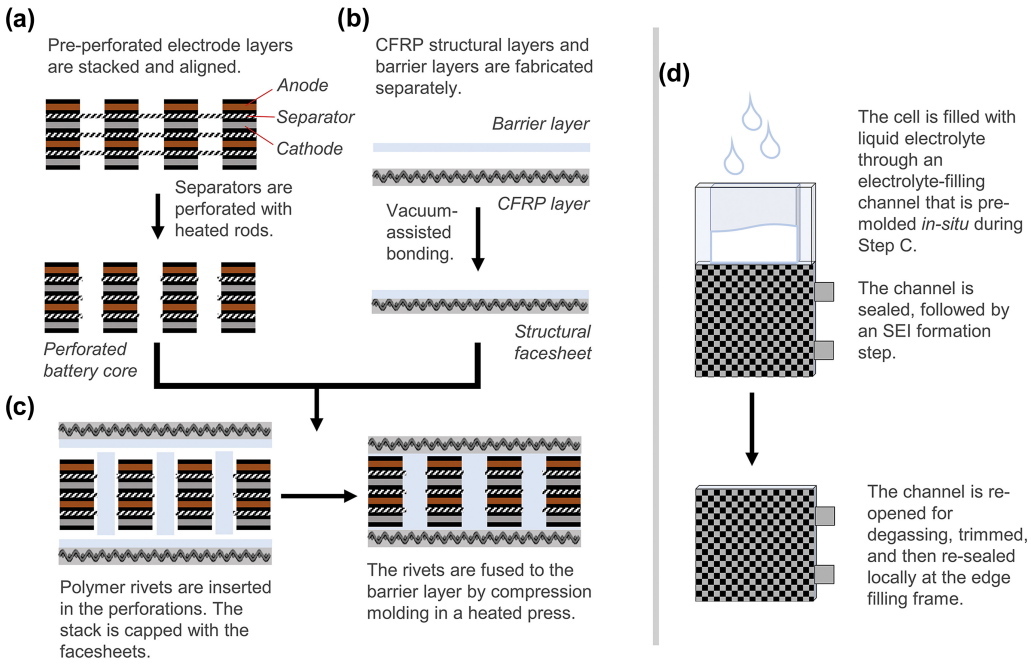

Figure 2.49: Novel structural battery fabrication process. (a) Perforated anode/cathode layers are laminated in alternating fashion, followed by local heating of the separator layers to create through-holes. (b) Structural facesheets are fabricated by vacuum-assisted bonding of CFRP plates and thin EAA barrier layers. (c) The structural battery assembly and riveting process uses compression molding to melt and fuse rivets to the encapsulating facesheets (d) The cell is filled with liquid electrolyte through a pre-formed channel. The cell is then sealed, formed, degassed, and resealed. Reproduced from [100].

Table 2.8: Summary of the properties of the batteries tested by Ladpli *et al.* [100], where the percentage values indicate the fraction of active surface area of the unperforated baseline pouch.

Case Study	Sample Description	Dimensions and Mass	Active Surface Area per Layer and Theoretical Specific Capacity
Baseline Pouch	Nonperforated battery in aluminum-laminate pouch	90 mm × 90 mm × 3.5 mm 81 ± 1 g	7921 mm^2 4.60 Ah (100 %)
CFRP/No Rivet	Nonperforated battery in CFRP but without rivets	110 mm × 110 mm × 5 mm 120 ± 5 g	7921 mm^2 4.60 Ah (100 %)
CFRP 4 × 4	CFRP with 4 × 4 perforation array	110 mm × 110 mm × 5 mm 120 ± 5 g	7469 mm^2 4.34 Ah (94.3 %)
CFRP 5 × 5	CFRP with 5 × 5 perforation array	110 mm × 110 mm × 5 mm 120 ± 5 g	7215 mm^2 4.19 Ah (91.1 %)

cal capacity, 4510 mAh, with a deviation of −2.0 % from the theoretical value for CFRP/No Rivet, 4243 mAh, −2.3 % for the CFRP 4 × 4, and 3974 mAh, −5.2 % for the CFRP 5 × 5. These results translate into specific energy values of 210, 139, 131, and 123 Wh/kg for the Baseline Pouch, CFRP/No Rivet, CFRP 4 × 4, and CFRP 5 × 5 samples, respectively. Furthermore, the corresponding energy densities were 601, 276, 260, and 243 Wh/L, **Table 2.9**.

Additionally, the study evaluated the life cycle performance of the batteries and observed

that all the batteries maintained at least 80 % of their capacity even after 800 cycles. Despite the novel SB structure and fabrication technique, the batteries were able to maintain a similar life cycle performance to that of industry-standard pouch cells with the same chemistry.

Furthermore, the mechanical performance of the batteries was evaluated using a quasi-static three-point bending test at a constant displacement rate of 3.33 mm/min, and structural sandwich samples were measured in the experiments to represent the upper mechanical performance bound. The Young's modulus was determined to be $\sim$ 1.1, $\sim$ 2.6, $\sim$ 9.6, $\sim$ 10.5, and $\sim$ 12.4 GPa for the Baseline Pouch, CFRP/No Rivet, CFRP 4 $\times$ 4, CFRP 5 $\times$ 5, and structural sandwich, respectively.

Table 2.9: Summary of the results of the electrochemical and mechanical tests performed on the batteries studied by Ladpli *et al.* [100], where the percentage values indicate the specific capacity loss compared to its theoretical value.

Case Study	Capacity [Ah]	Specific Energy [Wh/kg]	Energy Density [Wh/L]	Young's Modulus [GPa]
Baseline Pouch	4.60 (0 %)	210	601	1.1
CFRP/No Rivet	4.51 (-2,0 %)	139	276	2.6
CFRP 4 x 4	4.24 (-2,3 %)	131	260	9.6
CFRP 5 x 5	3.97 (-5,2 %)	123	243	10.5
Structural Sandwich	N/D	N/D	N/D	12.4

The use of CFRP sheets alone resulted in a slight increase in mechanical performance due to the presence of relative shear movement in the electrode layers, hindering the transfer of shear stress through the battery stack core and leading to inefficient use of these sheets. However, when interlocking rivets were introduced, a significant improvement in mechanical performance was observed, with a four-fold increase compared to the CFRP/No Rivet configuration and a ten-fold increase compared to the Baseline Pouch. Furthermore they reached almost 85 % of that of the structural sandwich, in which the entire battery volume was replaced with a structurally efficient polymer core. Additionally, the use of interlocking rivets resulted in minimal loss of active material, with only 5.7 % and 8.9 % being lost. Notably, the electrochemical performance under load showed that the best performing sandwich battery, CFRP 5 $\times$ 5, was able to carry up to 1160 N at the maximum 2 mm deflection, as compared to the 236 N carried by the CFRP/No Rivet configuration. These results demonstrate that the interlocking rivets effectively facilitate shear stress transfer through the electrode stack to the CFRP facesheets, reducing bending lengths and constraining boundary conditions. In summary, the use of interlocking rivets in sandwich battery construction maintains battery integrity and enhances electrical connections.

Zhang *et al.* [105] also adopted a sandwich-style approach in their study. The battery component served as the core of the sandwich-style SB and was responsible for carrying the transverse shear and compression loads while also storing energy. On the other hand, the top and bottom face skins were made of aluminum alloy, which carried the in-plane

and bending loads. A clear depiction of this SB can be found in **Figure 2.50a**.

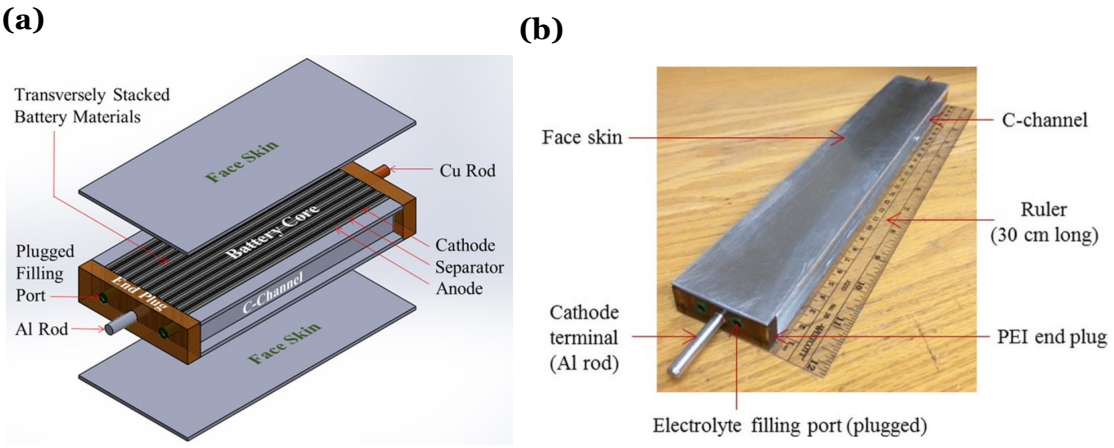

Figure 2.50: (a) Schematic concept of sandwich structural battery with (b) Photo of the assembled sandwich structural battery core and two face skins. Reproduced from [105].

The anode used in this study consisted of Cu foil coated with mesocarbon microbeads (MCMB) and a water-based binder composed of sodium salt of carboxymethyl cellulose (CMC) and styrene-butadiene rubber (SBR), with carbon black added as a conductive additive. The composition of the anode was 96.5 wt% MCMB, 0.5 wt% carbon black, 1.0 wt% CMC, and 2.0 wt% SBR. The cathode was made of Al foil coated with NCM bound with PVDF dissolved in NMP, with the weight percentages of NCM, carbon black, and PVDF being 94 %, 3 %, and 3 %, respectively. A separator (from Celgard) was used to prevent direct contact between the cathode and anode, and the electrolyte employed was a 1 M $LiPF_6$ solution.

The face skins were bonded to the top and bottom of the core using an adhesive, and C channels made of the same material as the face skins and polyetherimide end plugs were employed to isolate the core and confine the electrolyte. The final dimensions of the battery were 309 mm × 50 mm × 17.9 mm, with a geometric volume of 0.277 L and a mass of 632.2 g. The battery developed by the authors is depicted in **Figure 2.50b**.

The electrochemical performance of the SB was evaluated through charge and discharge cycles conducted at a rate of approximately C/3. The results revealed that the SB exhibited a specific energy of 102 Wh/kg, an energy density of 248 Wh/L, and a total energy of 64.5 Wh. Charge and discharge curves, obtained at room temperature for various cycles, are presented in **Figure 2.51a**. In addition, it exhibited a capacity retention of 85.8 % after 190 cycles. Furthermore, it was observed that the coulombic efficiency decreased to 97.5 % at the 190th cycle, **Figure 2.51b**. To evaluate the mechanical performance, three-point bend tests were conducted on the SB with (wet) and without (dry) the electrolyte, and the results are shown in **Figure 2.51c**. Zhang *et al.* [105] determined that the SB had a shear modulus of 5.69 GPa, and a Young's modulus of 32.7 GPa.

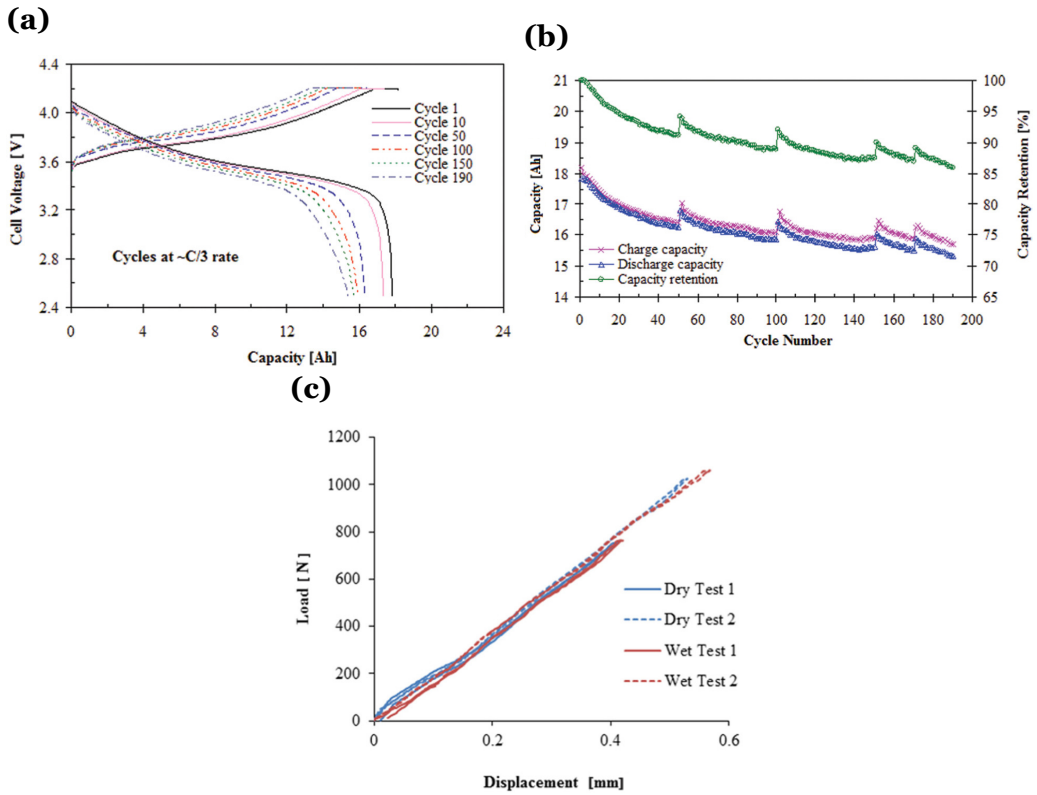

Figure 2.51: Performance of sandwich structure battery: (a) charge discharge curves, (b) charge and discharge capacity and capacity retention versus cycle number. (c) Load versus mid-span displacement plots for the three-point bend tests. Reproduced from [105].

It was also observed that after 50 charge discharge cycles at C/3 rate, three-point bend tests up to 1060 N did not adversely affect the subsequent electrochemical performance.

Hollinger *et al.* [106] took a simpler approach by employing standard 18650 cylindrical battery cells, which were housed within an aluminum tube. The primary aim was to utilize this battery system as the arms of a quadcopter.

The battery cells had an outer diameter of 18.5 mm, a length of 65 mm, and weighed 48.5 g. With a rated capacity of 3.2 Ah and a nominal voltage of 3.6 V. These LIBs exhibited a specific energy of 237 Wh/kg and an energy density of 659 Wh/L. Each SB was tested with either two or three cells inside the tube, respectively, and an outer diameter of 22.225 mm. An ABS plastic sleeve was utilized to electrically insulate the batteries from the exterior tube, as shown in **Figure 2.52**.

To assess the mechanical performance of the battery, a three-point bend test was conducted at a constant speed of 0.36 mm/min and a specified displacement of 24 mm. The results of this test, shown in **Table 2.10**, were used to compare the performance of the battery to that of an aluminum tube with the same dimensions, but without batteries inside. The Young's moduli were calculated based on the information provided.

It was observed that the variation in the test outcomes between the two-cell and three-

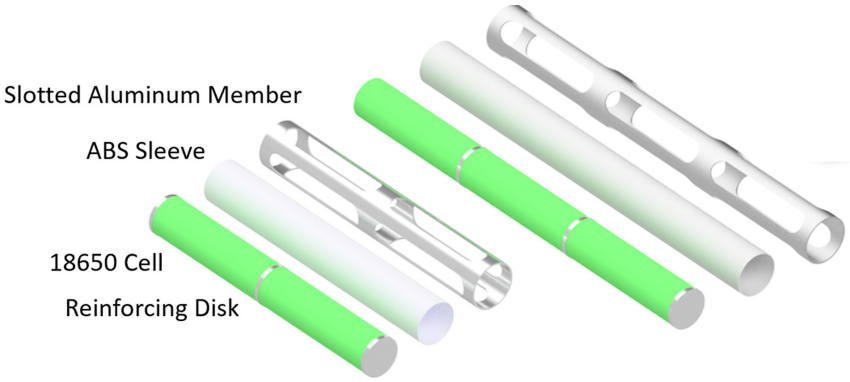

Figure 2.52: The two-cell and three-cell structural batteries consisting of slotted aluminum members, ABS plastic sleeves, 18650 lithium-ion battery reinforcement, and reinforcing inter-cell disks. Reproduced from [106].

Table 2.10: Stiffness, yield force and Young's moduli for all members tested by Hollinger *et al.* [106].

Configuration	Stiffness [N/mm]	Yield Force [N]	Young's Modulus [GPa]
134 mm (two-cell) with 18650	338.4	910.5	0.429
134 mm (two-cell) without 18650	82.16	477.5	N/D
200 mm (three-cell) with 18650	424.6	2622	0.538
200 mm (three-cell) without 18650	33.37	302.2	N/D

cell configurations was not due to the difference in length of the test articles, which was constant at 90 mm, but rather because of the diverse loading points. In the two-cell tests, the load was applied at the strongest point, between the slots, while in the three-cell tests, the load was applied at the weakest point, in the middle of the slots. Although no electrochemical analysis were conducted on the structural battery under load, its specific energy and energy density were estimated to be 212 Wh/kg and 443.2 Wh/L, respectively, slightly lower than those of the battery cell.

By substituting hollow aluminum tubes with the proposed structural battery in a notional quadcopter design, a theoretical maximum hover time enhancement of 41 % was achieved. The hypothetical design case was simplified to remove the impacts of additional variables, while still illustrating the potential of structural batteries.

2.3.4 Decoupled and Coupled Structural Batteries Comparison

After a thorough review of the existing literature on SBs, **Table 2.11** presents a comparative analysis of the most relevant properties of the batteries, reinforcement employed, and chemistry used. It's important to highlight that the reported Young's moduli were

determined using different testing methods. Some were measured through tensile strain testing, while others employed three-point bend testing. As a result, when interpreting the results, this factor must be considered. Moreover, as previously mentioned, certain coupled SBs may not possess the necessary rigidity to serve as standalone structures, necessitating their integration within a composite material. In such cases, it is important to acknowledge that the specific energy and Young's modulus of the SBs are likely to be altered. Therefore, when interpreting the results, it is crucial to consider these changes resulting from the integration process.

Additionally, **Figure 2.53** is an updated version of **Figure 2.14**, which includes SBs that were not previously referenced. In **Figure 2.54a**, it is provided a graphical representation of the specific energy of SBs based on the chemistry used. Furthermore, **Figure 2.54b** presents the Young's modulus of SBs based on the reinforcement employed.

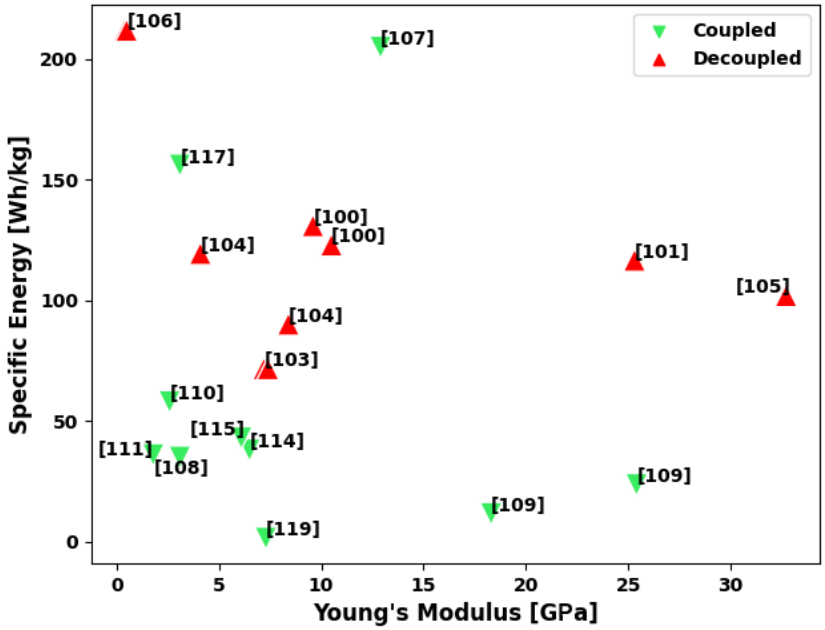

Figure 2.53: Specific energy values versus corresponding Young's modulus of reported structural batteries, numbered by their references.

From the comparison presented in **Figure 2.53**, it is evident that coupled SBs generally exhibit inferior mechanical and electrochemical performance compared to decoupled SBs, which corroborates the findings of **Figure 2.14**. Notably, the sole exception is the SB developed by Liu *et al.* [107], which displays the second highest specific energy. It's important to highlight that this battery relies on Zn-ion chemistry rather than Li-ion chemistry, showing that other chemistries have the possibility of surpassing Li-ion chemistry.

It can be observed from **Figure 2.54a** that structural batteries based on lithium chemistry generally exhibit higher specific energy. However, when considering only the coupled SBs, those employing Li-ion chemistry do not offer significantly greater specific energy than those based on other chemistries. Thus, the coupling mechanism appears to

Table 2.11: A summary of the findings from various structural battery research projects, highlighting the key reinforcement materials used, the base chemistry used, and the associated Young's modulus and specific energy values.

Main Reinforcement	Chemistry	Young's Modulus [GPa][1]	Specific Energy [Wh/kg]	Ref.
Coupled Structural Battery				
Carbon Fiber	Lithium-ion	8	N/D	[112]
Carbon Fiber	Lithium-ion	1.8	36	[108]
Carbon Fiber	Lithium-ion	2.6	58	[110]
Carbon Fiber	Lithium-ion	3.1	35	[111]
Carbon Fiber	Lithium-ion	18.3	11.6	[109]
Carbon Fiber	Lithium-ion	25.4	23.6	[109]
Carbon Fiber	Lithium-ion	N/D	10	[113]
Carbon Fiber	Zinc-Manganese Dioxide	12.8	205	[107]
Carbon Fiber	Sodium-ion	6.5	38	[114]
Carbon Fiber	Lithium-Sulfur	6.05	43	[115]
Interconnected parts imitating human joint	Lithium-ion	4	N/D	[116]
Polymer binder infiltrated in porous electrodes	Lithium-ion	3.1	156.1	[117]
Aramid nanofibers and zinc foil	Zinc-ion	N/D	190	[118]
Stainless steel mesh	Nickel-Iron	7.3	1.4	[119]
Decoupled Structural Battery				
Carbon Fiber	Lithium-ion	25.3	116.7	[101]
Carbon Fiber	Lithium-ion	4.07	119.5	[104]
Carbon Fiber	Lithium-ion	8.39	90.2	[104]
Carbon Fiber	Lithium-ion	7.21	71.7	[103]
Carbon Fiber	Lithium-ion	7.41	71.7	[103]
Interlocking polymer rivets	Lithium-ion	9.6	131	[100]
Interlocking polymer rivets	Lithium-ion	10.5	123	[100]
Aluminum sheets and battery	Lithium-ion	32.7	102	[105]
Aluminum tube and battery	Lithium-ion	0.429	212	[106]
Aluminum tube and battery	Lithium-ion	0.538	212	[106]

[1] Highest value found in the literature.

have a greater impact on specific energy than the underlying chemistry. In terms of Young's modulus, as shown in **Figure 2.54b**, there is little difference between using CF reinforcement or not. Although on average, CF-based SBs exhibit slightly superior performance, certain instances of non CF-based SBs can outperform them. It is noteworthy that some of the SBs employing non CF reinforcement also incorporate CF as a secondary reinforcement. Moreover, for CF-based batteries, whether coupled or decoupled, on average the Young's modulus is quite similar, whereas for non CF-based SBs, there is a significant

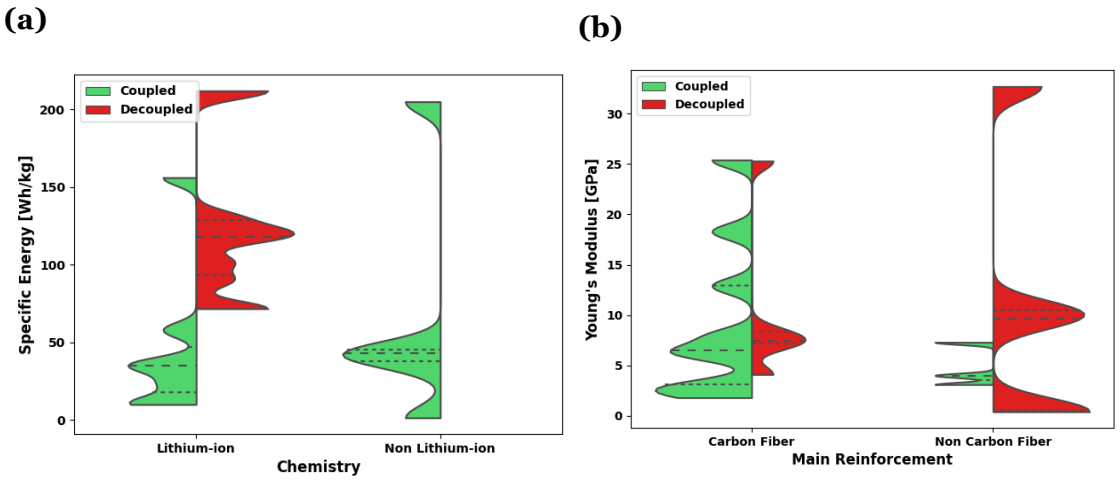

Figure 2.54: Violin plots. (a) Specific energy of the structural batteries divided by the chemistry and coupling. (b) Young's modulus of the structural batteries divided by the main reinforcement and coupling.

difference, decoupled present higher Young's modulus on average.

In conclusion, this comprehensive analysis of the works on SBs reveals an enormous variety and potential for these batteries to adapt and provide innovative solutions. Nevertheless, it is crucial to consider the environment, purpose, and operating conditions when designing SBs, to ensure the best possible outcome.

2.3.5 Recyclability, Maintenance and Environmental Impact

The life cycle of SBs presents certain challenges that must be addressed, particularly in their integration into device structures, which is critical for achieving weight reductions. In contrast to conventional batteries, the failure or damage of an SB requires replacement of the entire device structure, making maintenance and recycling difficult. Moreover, the goal of achieving more efficient electric vehicles necessitates environmentally sustainable and safe components for manufacturing SBs. Recycling and disposal of the battery components, including the structural support, active material, electrolyte, and connectors, must be carried out individually to minimize negative environmental impacts, some investments have been made to reuse the raw materials of LIBs [128]. Given that used electric car batteries typically retain 75 % to 80 % of their capacity, they can be used for less energy-demanding applications such as backup power or electric scooters [129]. Therefore, SBs should be designed to be easily recyclable to reduce the environmental impacts of sending used batteries to landfills.

Moreover, it is important to consider the life expectancy of Li-ion batteries, which are widely used in SBs and EVs. Studies indicate that Li-ion batteries used in EVs typically have a life span of approximately 10 years [130]. This means that the entire structure, at best, will last for 10 years before requiring replacement. Such a scenario is not desirable

due to its environmental impact and cost implications. Therefore, effective maintenance strategies for SBs must be adopted to extend their operational life and promote sustainable practices.

Zackrisson *et al.* [131] conducted a prospective LCA of SBs used as a car roof, replacing steel roofs and conventional batteries. Their SB model consisted of CF as the negative electrode, GF as the separator, and CF coated with $LiFePO_4$, PVDF binder, and carbon black as the positive electrode, with an SBE electrolyte. The costs and energy consumption for each component, from the coating process to the production of chemicals in the SBE, were included in the LCA. The results were divided into the current state of structural battery research (referred to as initial design), and what can be theoretically reachable with continuous improvements to its manufacturing and design (referred to as target design). The structural battery roofs in the initial and target designs weigh 7.8 kg and 9.2 kg, respectively, with corresponding energy densities of 41 Wh/kg and 121 Wh/kg. In comparison, a steel roof weighs 18.6 kg. Consequently, the initial design offers a mass savings of 10.8 kg in the vehicle, while the target design provides a mass savings of 9.4 kg. Moreover, these structural battery roofs can also contribute to additional mass savings of traction batteries, ranging from 2.2 kg to 12.9 kg. Therefore, the total mass savings achieved by implementing these structural battery roofs are even more substantial.

The authors also modeled the conventional batteries to be replaced by the structural battery, using a 24 kWh Li-NMC battery for a small vehicle and an 85 kWh Li-NCA battery for a large vehicle. The costs of manufacturing the steel roof were also taken into account, as were the recycling process and transport to the recycling center. The net difference in life cycle environmental impacts when replacing a steel roof and an equivalent part of the original battery with a structural battery roof are presented in **Figure 2.55**. A negative measure indicates an avoided impact due to the structural battery roof.

Figure 2.55a depicts the climate impact, which is the production of CO_2 per kilogram, of the SBs in all case studies. The authors observed that the climate avoidance was greater in the small electric vehicle (EV) compared to the large EV due to the lower energy density of the NMC battery in the former. **Figure 2.55b** displays the net life cycle ozone formation impacts, revealing that the use of SB roofs avoids ozone formation in all examined cases. However, the photochemical ozone formation impacts show a different pattern compared to climate impacts, with the largest savings from using an SB roof seen in the large EV. The authors explained that the reason for this is not the size of the EV but the production of the NCA cathode, which has relatively large NO_x emissions. Lastly, **Figure 2.55c** illustrates resource depletion, measured in gram antimony equivalents, and again, the use of SB roofs avoids abiotic depletion.

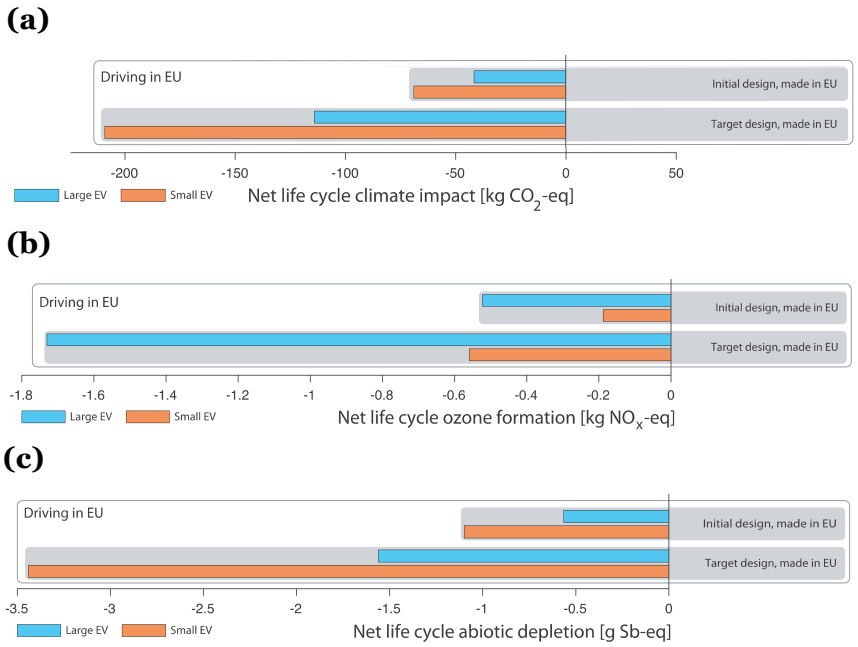

Figure 2.55: (a) Net life cycle climate impacts of structural battery roof, all cases, in kilogram CO2 equivalent. (b) Net life cycle ozone formation of structural battery roof, all cases, in kilogram nitrogen oxide equivalents. (c) Net life cycle abiotic depletion of structural battery roof, all cases, in gram antimony equivalents. Adapted from [131].

In summary, the analysis indicates that SBs have the potential to not only enable weight reduction but also have smaller adverse environmental impacts. Specifically, SBs in the small EV yielded greater reductions in climate and abiotic depletion, while SBs in the large EV offered greater reductions in ozone formation. Furthermore they also concluded that the sources of the environmental impacts are mainly the production of the components chosen.

From this section, it becomes evident that when developing a SB, electrochemical and mechanical performance are not the sole factors to be considered. Other critical aspects such as cost, safety, environmental impact, among others, are highly influenced by the materials chosen for the electrochemical and structural components, as well as the design of the SB.

A nested pie chart in **Figure 2.56** visually illustrates some of the factors mentioned earlier, presenting their interdependencies and how they can be affected.

The selection of materials significantly influences the overall cost of the SB, as certain materials are more cost-effective to obtain and manufacture than others. Additionally, the lifespan of the SB hinges on the active materials chosen. Recyclability, on the other hand, is influenced by the ease with which the materials of the electrochemical and structural components can be recycled or reused in less demanding applications.

Safety considerations primarily revolve around the choice of materials for the electrochemical component, as some chemistries are less reactive, possess a lower risk of ther-

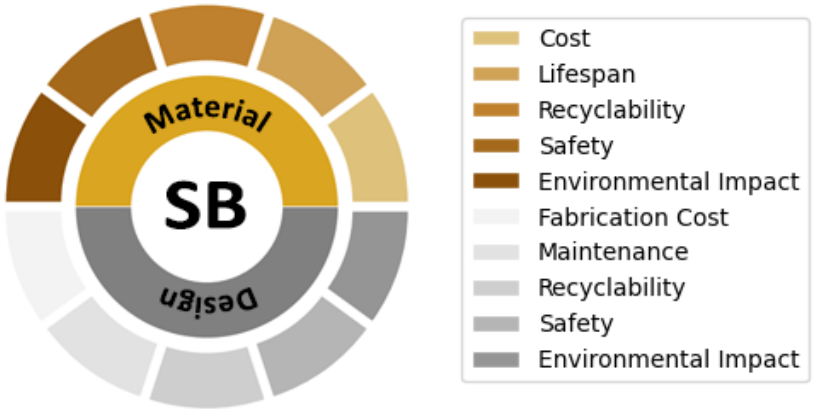

Figure 2.56: Factors to consider when designing a structural battery and its interdependencies.

mal runaway, and exhibit lower toxicity. Furthermore, the production and extraction of materials for the SB can result in varying environmental impacts, with some processes being more environmentally friendly than others.

The choice of design also plays a crucial role, affecting fabrication costs and ease of assembly. A simple and straightforward assembly process is preferred. Moreover, the design influences the maintenance process and the ability to monitor the health of the SB throughout its operational life.

Recyclability is not limited to the ease of recycling materials, but rather extends to the disassembly and reusability of components. Decoupled SBs offer greater ease in distinguishing and separating components for recycling or reuse, while coupled SBs may pose challenges due to the tight integration of the different components, making it challenging to repurpose them beyond their original function.

Safety is also influenced by design, as a well-designed SB should ensure that it continues to operate safely even in the event of failure. Similar to the materials, the various assembly processes required for the SB consume energy and contribute to pollution, necessitating careful consideration during the design phase to minimize negative environmental impacts.

In conclusion, the careful selection of materials and design for the SB is crucial, taking into account all the aforementioned factors and more, to ensure a positive impact on the environment and overall sustainability.

Chapter 3

Materials and Experimental Procedures

This chapter aims to explain the process of selecting the chemical composition for the structural battery, as well as the materials used. A detailed account of the fabrication techniques involved in the production of the various battery components, particularly the cathode and electrolyte, will be provided. Moreover, the step-by-step assembly of the structural battery will be expounded upon. Lastly, the experimental procedures utilized to assess the mechanical and electrochemical properties of the battery will be presented.

3.1 Materials

As stated in the **Section 1.2**, the SB developed employs an Al-ion chemistry. This decision was made due to the fact that aluminum is significantly more abundant in the earth's crust compared to lithium, thus making it more economical, environmentally sustainable, and easier to extract. Given the focus of this research on the development of a cost-effective and sustainable battery, the Al-ion chemistry was deemed to be a suitable choice. Although AIBs have a lower specific energy, it has been demonstrated that they possess considerable potential.

In addition to their performance, AIBs offer several other advantages over LIBs, including the potential for tens to hundreds of thousands of life cycles, non-flammability, safety, a lower likelihood of thermal runaway, and high specific power. While AIBs share similar advantages to SIBs, as illustrated in **Figure 2.13**, they boast higher theoretical specific energy, cyclability, and several other slightly superior properties. Significantly, AIB components are easier to fabricate than SIB components, as most studies on SIBs mentioned in this work rely on more challenging-to-produce battery components.

Zinc, potassium, and magnesium batteries were not considered due to insufficient research. Although AABs have significantly higher specific energy, they are mainly non-rechargeable and require replacement after a certain period. Since the battery is integrated into a structure, this renders the structure equally disposable, which is neither an economically nor environmentally sustainable practice. This method might be viable if the battery outlives the structure, but according to MIT's research, the battery does not last more than 30 days [132].

Figure 3.1 presents a spider plot that qualitatively analyzes some of the previously mentioned battery chemistries. The graph represents a comparison of Li-ion, Al-ion, and Na-

ion batteries based on the findings and conclusions of the studies reviewed in this work. A score of 1 denotes the poorest evaluation, while 5 denotes the best. From this analysis is possible to see that the AIBs have better results and why their chemistry was chosen over the others.

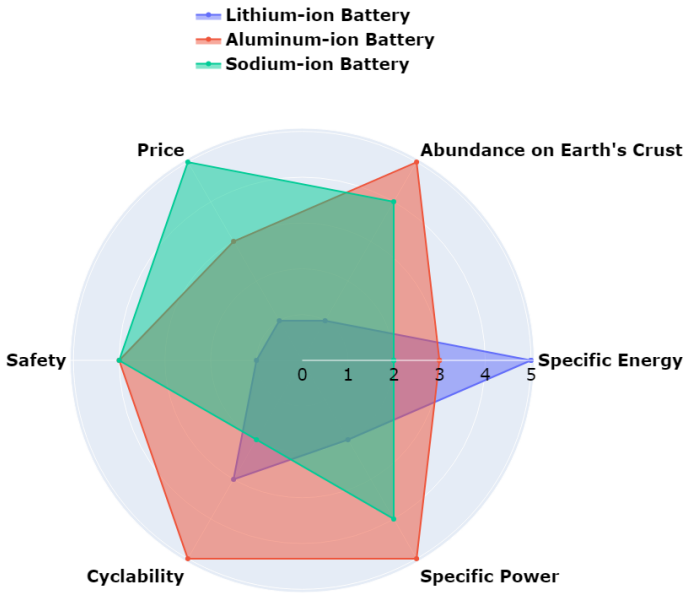

Figure 3.1: Qualitative analysis of lithium-ion batteries, aluminum-ion batteries and sodium-ion batteries.

For the negative electrode of the AIB, an Al (from MIT KJ Group, 7429-90-5) sheet with a thickness of 15 µm and 99.35 % purity was selected, following the common practice for AIBs. To form the cathode, G nanoplatelets with 2 - 140 layers (from Graphenest) was chosen as the active material, which was coated onto carbon fiber (from Rebelco 195 T), that served as both current collectors and structural components of the battery. The use of G is well-established as an efficient active material for AIBs, while the integration with CF enhances the mechanical and electrical properties of the fibers. Moreover, the decision was made to integrate the electrochemical components within a structural component to enable its functionality as a standalone structure. To achieve this, impregnated CF and GF (from Rebelco, 1195 P) sheets were utilized as the structural component of the battery. The separator comprised a Whatman Grade 1 filter paper (from Cytiva), which was soaked in electrolyte, and served as an insulator to prevent short circuits within the AISB.

In order to enhance the safety of the SB, an IL was chosen as the electrolyte, which was expected to offer several benefits, as previously demonstrated. The IL electrolytes utilized in AIBs consist predominantly of aluminum-containing salts, especially aluminum chloride ($AlCl_3$), and corresponding solvents. Among these solvents, three primary options are employed, namely 1-ethyl-3-methylimidazole chloride ([EMIM]Cl), 1-butyl-3-methylimidazolium chloride ([BMIM]Cl), and urea. **Figure 3.2** presents a statistical

summary of the most commonly employed IL electrolytes in AIBs, along with their respective molar ratios.

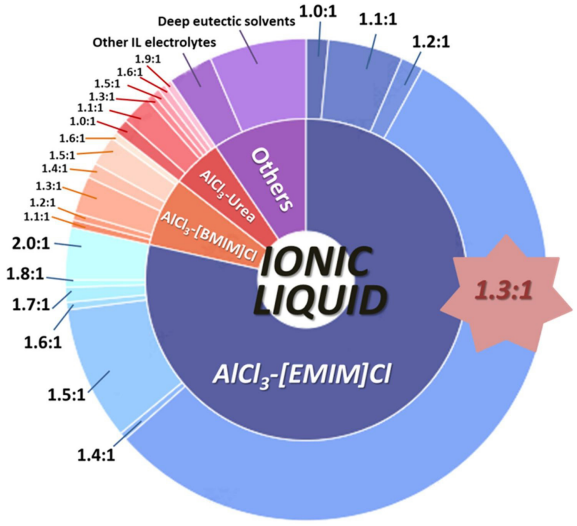

Figure 3.2: Statistical analysis of various molar ratios in ionic liquids used in rechargeable aluminum-ion batteries. Reproduced from [29].

As depicted in **Figure 3.2**, the most commonly employed IL in AIBs is the $AlCl_3$-[EMIM]Cl with a ratio of 1.3:1, as it demonstrated superior battery performance. The charging mechanism of AIBs utilizing these ILs involves the oxidative intercalation of $AlCl_4^-$ into the cathode, followed by the deposition of Al as $Al_2Cl_7^-$ is reduced at the anode, generating Al and $AlCl_4^-$.

However, a major drawback of [BMIM]Cl and [EMIM]Cl is their high cost. To address this issue, new solvents such as urea have been gaining attention due to their low cost and environmentally friendly nature. Despite having a slightly lower discharging voltage compared to other ILs [68], the IL made of $AlCl_3$ salt, 99 % pure (from Thermo Fisher Scientific Inc., 7446-70-0) and urea, 99.5 % pure (from Thermo Fisher Scientific Inc., 57-13-6) was chosen as the electrolyte for this study due to the aim of designing a cost-effective and sustainable SB. Previous studies [133–135] have demonstrated that there is no significant change in the performance of $AlCl_3$-Urea with mole ratios ranging from 1.3:1 to 1.5:1. Thus, for this study, a mole ratio of 1.4:1 was employed.

The presence of both $AlCl_4^-$ and $Al_2Cl_7^-$ anions in acidic $AlCL_3$ IL electrolytes is a well-established fact. Despite this, the charging and discharging mechanism of batteries utilizing such electrolytes and G cathodes remains uncertain. Nevertheless, two distinct reversible processes are believed to occur during charging and discharging:

$$\text{At the anode:} \quad 4Al_2Cl_7^- + 3e^- \leftrightarrow Al + 7AlCl_4^- \quad (3.1)$$

At the cathode: $nC + AlCl4^{-} \leftrightarrow C_n(AlCl_4^{-}) + e^{-}$ (3.2)

3.1.1 Cathode Fabrication

The fabrication process of the cathode involved coating the CF with a slurry comprising of G nanoplatelets and P(VDF-HFP) (from Solvay, Solef 21216) in an 4:1 mass ratio. The preparation of the slurry entailed mixing G and P(VDF-HFP) in a mortar using mechanical means. Subsequently, a polymer solvent, N,N-dimethylformamide (DMF, from Honeywell, 33120-1L), was added to the mixture until the slurry achieved the desired consistency to coat the CF. The cathode electrode composite was then dried for 5 hours at 60 °C to obtain a mass of active materials of approximately 3 mg/cm^2. The detailed steps for the fabrication of the cathode are illustrated in **Figure 3.3**.

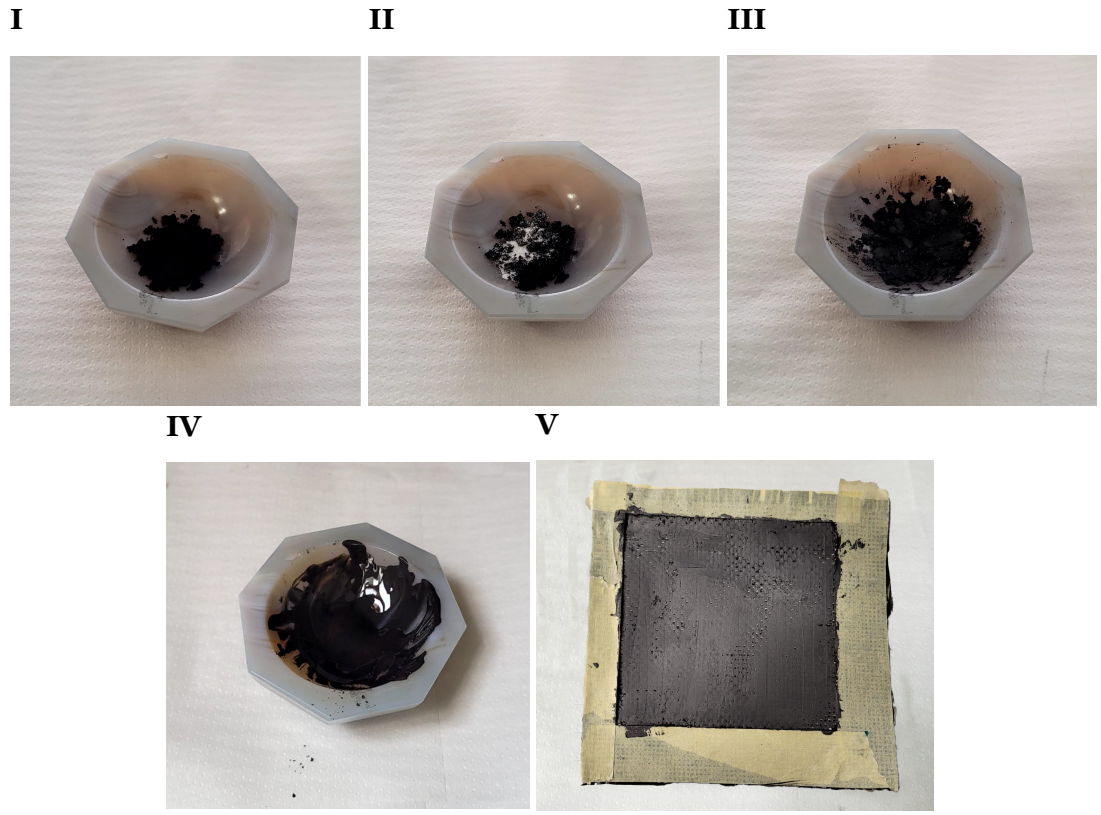

Figure 3.3: Fabrication steps of the cathode: I - Adding graphene; II - Adding PVDF; III - Blend the mixture; IV - Adding the polymer solvent and mixing; V - Coating the slurry onto carbon fiber tissue.

3.1.2 Electrolyte Fabrication

The synthesis of the electrolyte involved a meticulous procedure of mixing urea and $AlCl_3$ in a tightly sealed flask, in this case paraffin plastic was used. Ideally, a glove box would have been used to create an oxygen free environment and prevent any undesired reaction

with atmospheric air. However, due to the unavailability of such equipment, alternative measures, such as tightly sealing the flask, were taken to minimize reaction with oxygen. The solution temperature was carefully controlled by submerging the flask in ice-cold water. By following this approach, the ionic liquid was successfully produced through stirring of the mixture at ambient temperature over night. In **Figure 3.4** is shown the IL in the mixing stage at ambient temperature after being taken out of the ice-cold water.

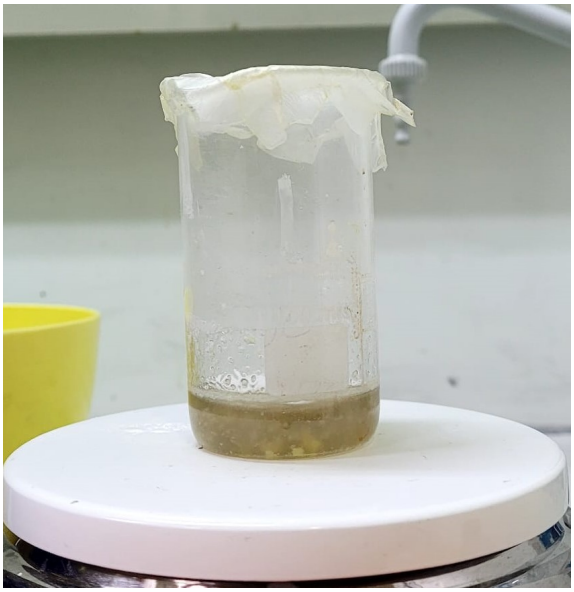

Figure 3.4: Final steps of the manufacture of the ionic liquid, $AlCl_3$-Urea at a molar concentration of 1.4:1.

3.1.3 Structural Battery Fabrication

The fabrication process of the AISB involved the utilization of a vacuum infusion layup technique. The layup process wasn't possible to be done inside a glove box not ensuring a proper insulation of the electrochemical components from oxygen. For the cathode material, G nanoplatelets were chosen, as previously mentioned, and a Cu foil tab was added to it. On the other hand, an Al sheet was employed as the anode, featuring its own tab. Prior to assembly, the Al sheet was cleaned using alcohol and all components dried in the oven to remove moisture.

In this work, a design similar to the one employed by Asp *et al.* [18], as depicted in **Figure 2.18**, was adopted. This design not only prevented direct contact between Al and CF, which is undesirable when CF constitutes the entire structural component, but also effectively reduced internal resistance, achieved balanced electrode material distribution, enhanced cell capacity, and ensured a symmetric laminate structure to prevent deformation and warpage [18].

The arrangement of the electrochemical components followed a specific layup sequence, as depicted step by step in **Figure 3.5**. The sequence involved placing the components in the following order: cathode, separator, anode, separator, and cathode. A schematic representation of this layup sequence is also provided for clarity and reference.

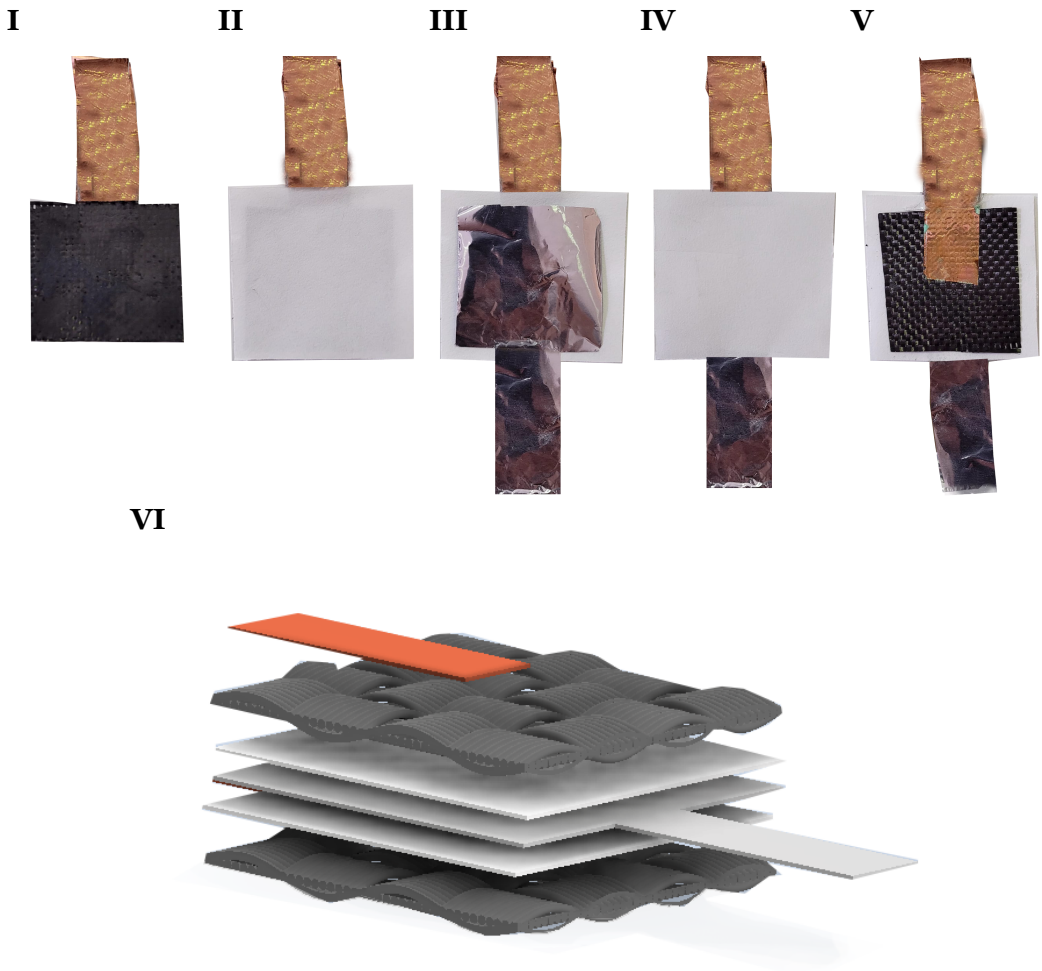

Figure 3.5: Layup of process of the electrochemical components: I - Cathode; II - Separator; III - Anode; IV - Separator; V - Cathode; VI - A scheme displaying the 3D stacking of the of the electrochemical components of the Aluminum-ion structural battery.

Following that, the separator was saturated with the ionic liquid using a syringe, **Figure 3.6**. Care was taken to use the minimum amount required to maintain mechanical performance and avoid excessive weight gain. The purpose of enclosing it within a sealing bag, and why it wasn't stacked between the structural component, will be elaborated on in subsequent sections.

The previously assembled electrochemical component has load bearing capabilities due to the reinforced cathode acting as a structural element, allowing it to be used as a structural battery. Nonetheless, it lacks the necessary rigidity and stiffness for independent

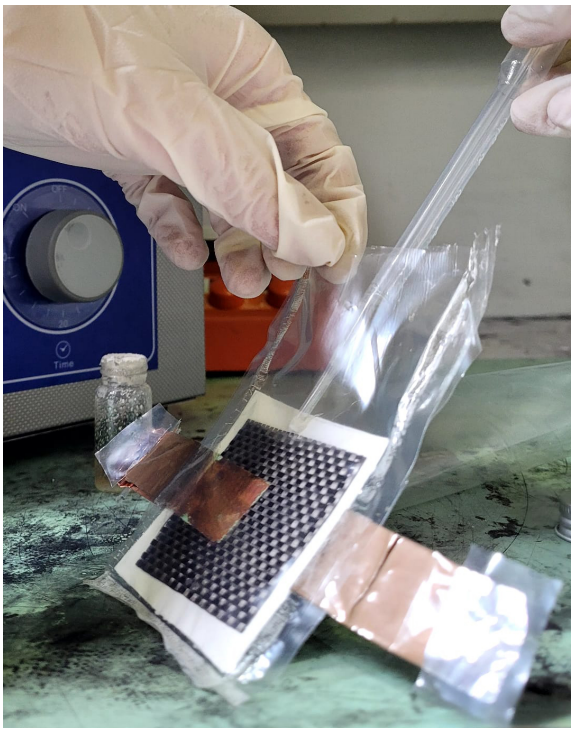

Figure 3.6: Injection of the ionic liquid in the separator.

functionality as a standalone structure. As a result, it requirements integration into a fiber-reinforced polymer, which will serve as the primary structural component.

In order to determine the most mechanically advantageous design for the battery's structural component, multiple designs were implemented and assessed. In all of these designs, an equal total mass of fibers was utilized. Whether using carbon fiber or glass fiber, each design incorporated a total of eight fiber sheets, as the mass per unit area for CF and GF sheets is approximately equivalent, measuring 196 g/m^2 and 195 g/m^2, respectively, and eight was chosen as the number because CFRP utilized in aeronautical structures is normally made up of eight carbon fiber sheets.

Samples intended solely for mechanical testing of the designs were fabricated by cutting the fibers for the structural component into 60 $\times$ 60 mm^2 pieces. Before the layup process, these fibers were meticulously coated with SR GreenPoxy 56, a green epoxy resin (from Sicomin), in conjunction with SD Surf Clear, a hardener (from Sicomin). As for the electrochemical components, the surface area of the active material was 30 $\times$ 30 mm^2, accounting for 25 % of the total SB surface area. To mitigate the utilization of costly materials, and considering the absence of electrochemical tests, the CF employed for the cathode was intentionally left uncoated with G, while the separator remained untreated without immersion in the IL.

However, for the samples employed in electrochemical and mechanical testing, the CF was coated with G, and the separator was soaked in IL. Fibers for the structural component were cut into 100 $\times$ 100 mm^2 pieces and coated with the same resin mixture. The elec-

trochemical components, in turn, had a surface area of 50 × 50 mm^2, also corresponding to 25 % of the total surface area. In both types of samples, the separator was cut to be 10 mm larger than the electrodes in both dimensions. Following the layup, the samples were cured under vacuum and pressure at room temperature for 24 hours, followed by an additional 24 hours at 40°C, like instructed in the epoxy data sheet.

The first design exclusively utilized carbon fiber sheets. To prevent a short circuit between the Cu and Al foil tabs in contact with CF, they were electrically insulated using a duct tape. A schematic representation of the step-by-step layup process and the stacked battery for this design is presented in **Figure 3.7**.

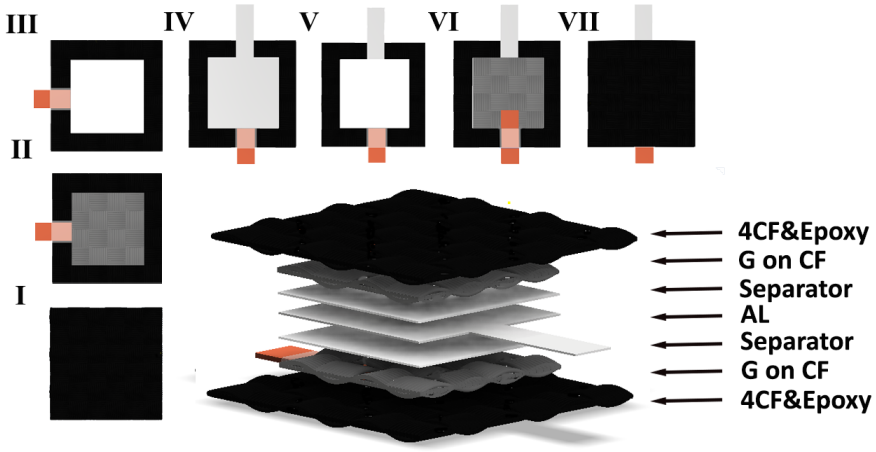

Figure 3.7: A scheme displaying the stacking of the individual layers of the first design of the Aluminum-ion structural battery. I - Four epoxy-impregnated CF sheets, II - Cathode, III - Separator, IV - Anode, V - Separator, VI - Cathode, VII - Four epoxy-impregnated CF sheets.

For this design, **Figure 3.7**, the initial layer consisted of four epoxy-impregnated CF sheets in step I. Subsequently, the electrochemical components were assembled following the previously described procedure, steps II to VI. Finally, four additional epoxy-impregnated CF sheets were laid on top to seal the electrochemical components.

The second design closely resembled the first, but it employed two GF sheets on each side to insulate the tabs. This minimal number of GF sheets was found to offer adequate electrical insulation. The remaining fiber sheets in this design were CF, resulting in a total of four GF and four CF sheets. A schematic representation of the step-by-step layup process and the stacked battery for this design can be found in **Figure 3.8**.

In the case of this design, **Figure 3.8**, the initial layer comprised two epoxy-impregnated CF sheets in step I. Then, two epoxy-impregnated GF sheets were stacked on top in step II.

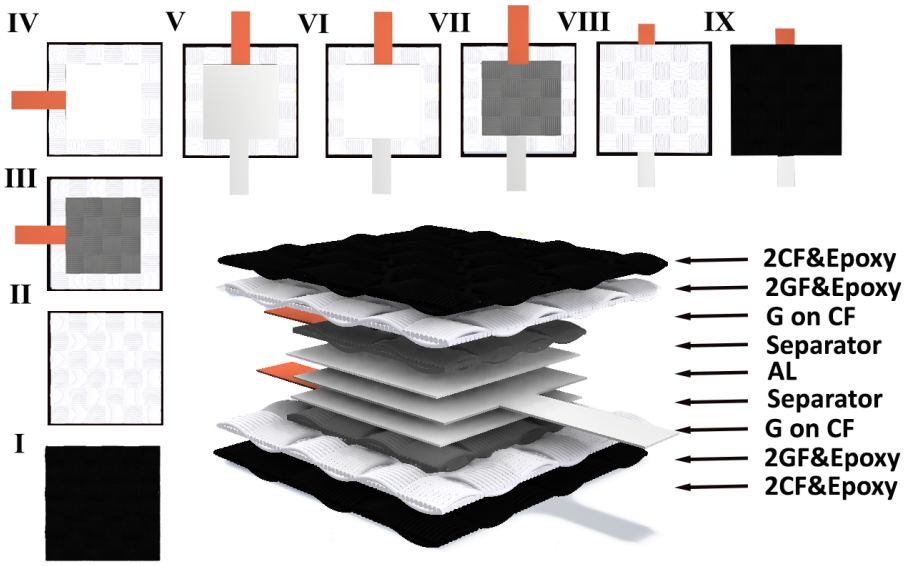

Figure 3.8: A scheme displaying the stacking of the individual layers of the second design of the Aluminum-ion structural battery. I - Two epoxy-impregnated CF sheets, II - Two epoxy-impregnated GF sheets, III - Cathode, IV - Separator, V - Anode, VI - Separator, VII - Cathode, VIII - Two epoxy-impregnated GF sheets, IX - Two epoxy-impregnated CF sheets.

Following that, the electrochemical components were layered according to the previously outlined process in steps III to VII. Finally, the first two steps were repeated, adding two epoxy-impregnated GF sheets and two epoxy-impregnated CF sheets in steps VIII and IX, respectively, to seal the electrochemical components.

These two designs were developed to evaluate the trade-off between incorporating a polymer around the tabs, potentially increasing defects and interfaces within the composite, and using GF, which is structurally weaker than CF but reduces defects and interfaces within the composite.

The third design presented greater complexity compared to the previous two. In this design, the electrochemical components (cathode) and structural components were integrated into a single unit, further reducing defects and interfaces within the composite. To insulate the tabs, two GF sheets were again employed, but these sheets featured a hole in the middle to allow contact between the IL-soaked separator and the cathode. This design consisted of two CF sheets, one of which the cathode was incorporated into, along with two GF sheets on each side. A schematic representation of this design and its step-by-step layup process is shown in **Figure 3.9**.

For this design, **Figure 3.9**, the first layer involved one epoxy-impregnated CF sheet in step I. Next, the epoxy-impregnated CF sheet with G was stacked on top in step II. The resin mixture was only applied in the area were G coating wasn't to be applied. In step

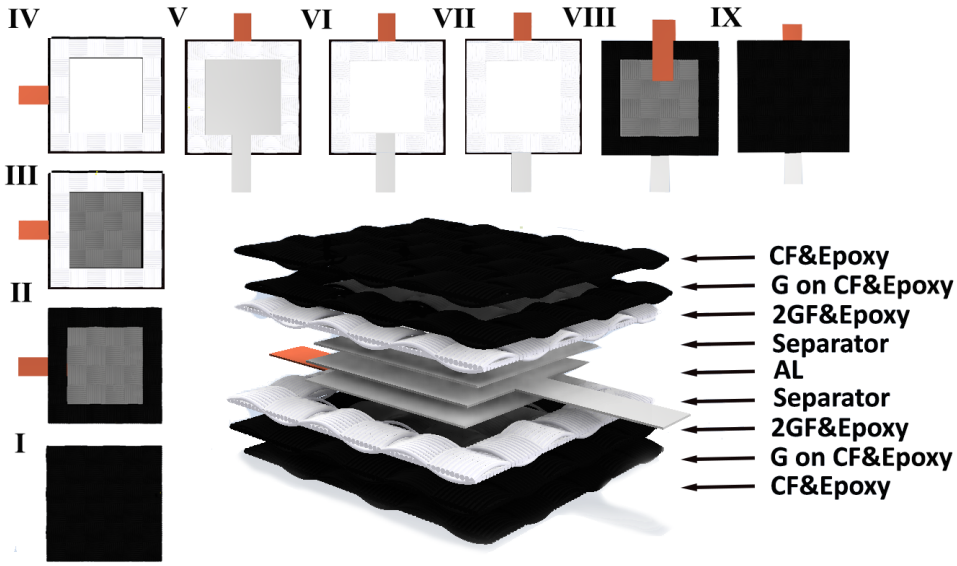

Figure 3.9: A scheme displaying the stacking of the individual layers of the third design of the Aluminum-ion structural battery. I - One epoxy-impregnated CF sheets, II - Cathode on epoxy-impregnated CF sheets, III - Two epoxy-impregnated GF sheets, IV - Separator, V - Anode, VI - Separator, VII - Two epoxy-impregnated GF sheets, VIII - Cathode on epoxy-impregnated CF sheets, IX - One epoxy-impregnated CF sheets.

III, two epoxy-impregnated GF sheets were stacked. Subsequently, the electrochemical components (separator, Al foil, and separator) were stacked in steps IV to VI. Finally, the first three steps were repeated, two epoxy-impregnated GF sheets, the epoxy-impregnated CF sheet with G, and one epoxy-impregnated CF sheet were layered on top in steps VII, VIII, and IX, respectively, to seal the electrochemical components.

3.1.4 Mechanical Characterization

The Al-ion structural battery underwent three-point bend testing using a Shimadzu AGS-X testing machine, equipped with a 10 kN load cell, and employing a testing rate of 2 mm/min. This rate aligns with the typical speed employed in previous studies. Furthermore, the span distance between the supports was set in accordance with the guidelines outlined in ASTM Standard D 790 [136], ensuring it exceeded 16 times the thickness of the samples, which in this case was 50 mm for the mechanical testing of the three designs and 75 mm for the mechanical testing of the complete SB.

Furthermore, the flexural strength σ_f and bending modulus E_f were obtained using the following equation [136]:

$$\sigma_f = \frac{3PL}{2bh^2} \quad (3.3)$$

$$E_f = \frac{L^3 t}{4bh^3} \quad (3.4)$$

Where P represents the applied load (N), L denotes the span (mm), b refers to the specimen width (mm), h refers to the specimen thickness (mm), and t denotes the slope of the tangent to the initial straight-line portion of the load-deflection curve (N/mm). The three supports had a diameter of 5 mm.

The Al-ion structural battery used in the tests had dimensions previously explained. In **Figure 3.10** is shown the set up for the mechanical tests, on it is possible to observe a SB and a multimeter connected to its tabs.

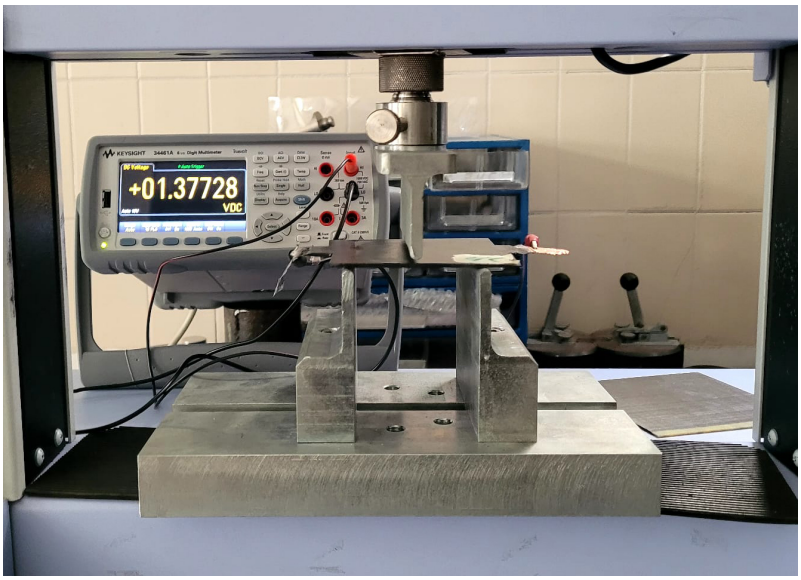

Figure 3.10: The set up for the three-point bending test of the structural batteries.

3.1.5 Electrochemical Characterization

To assess the electrochemical properties of the structural battery, it is typically necessary to conduct a series of discharge and charge tests, and others. However due to the electrolyte this was not possible and the reason are going to be presented in the subsequent chapter. Consequently, an alternative approach was employed to demonstrate the battery's charge storage capability. The battery was connected to different colored LEDs, in order to verify its ability to power devices.

In addition, the voltage of the battery and its internal resistance were measured. To determine the internal resistance, a resistor was connected to the terminals of the battery, and

the voltage drop across the resistor was measured using a voltmeter. The circuit diagram for this setup is depicted in **Figure 3.11**.

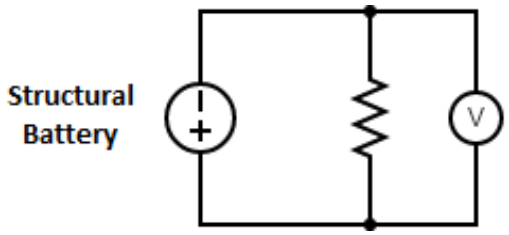

Figure 3.11: Circuit to measure the internal resistance of the battery.

The internal resistance of the battery can then be estimated using Ohm's Law. The internal resistance (Ri) is approximately equal to the voltage drop across the resistor (Vr) divided by the current flowing through it (Ir), **Equation 3.5**.

$$Ri = \frac{Vr}{Ir} \quad (3.5)$$

Chapter 4

Results and Discussion

This chapter aims to provide a comprehensive presentation of the findings and results obtained in the course of this study. It encompasses not only the final outcomes but also delineates the meticulous process undertaken to attain these outcomes, encompassing both successes and failures encountered along the way. By delving into the details of the methodology and experimental procedures, this chapter will offer a comprehensive account of the journey towards the ultimate results.

4.1 Graphene Coating

Before finalizing the selection of the CF coating method used as discussed in **Chapter 3**, a thorough evaluation of several techniques was conducted. Among the considered methods were electrophoretic deposition, spray coating, and the method ultimately employed in this study. However, due to constraints imposed by the available equipment, the electrophoretic deposition method was ruled out as a viable option, even though this would allow for better mechanical results [115]. Nonetheless, the spray coating method was subjected to experimental testing. In this approach, a graphene solution of varying concentrations was meticulously prepared using DMF and ultrasonicated until the graphene was dispersed, and subsequently spray coated onto the CF substrate [137]. Following the subsequent drying process at ambient temperature, the observation of a well-coated graphene layer proved to be challenging without the aid of a microscope. Moreover, the adhesion between graphene and CF was notably weak, resulting in an electrical resistance comparable to that of the pristine CF. Consequently, based on a comparative evaluation of the two approaches, the method employed in this study was chosen, as it exhibited superior performance when compared to the spray coating technique, for this method graphene and PVDF were mixed together and then DMF was added until forming a paste, this was then spread over the carbon fiber sheets.

4.1.1 Morphological Results

In **Figure 4.1**, a microscopic view of the coated carbon fiber is presented. The left side of the image displays the pristine carbon fiber, whereas the right side shows the coated carbon fiber. The analysis reveals that the distribution of G is non-uniform, as evident from the exposure of carbon fiber in some regions where the graphene was coated.

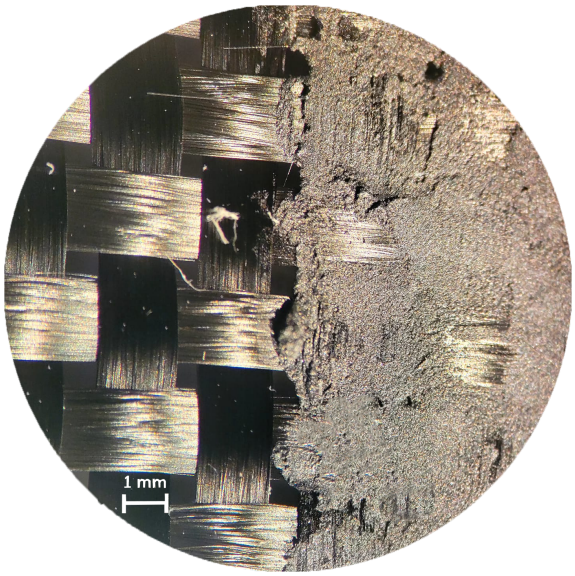

Figure 4.1: Microscopic view of the coated carbon fiber.

Moreover, given the intended application of the battery under load conditions, it is crucial to assess the adhesion of the graphene coating to the carbon fiber and the potential occurrence of cracks upon the application of a load. To investigate these aspects, a microscopic examination of the graphene coated carbon fiber was conducted before and after subjecting it to tensile testing. The visual representations of these observations are illustrated in **Figure 4.2**.

(a) **(b)**

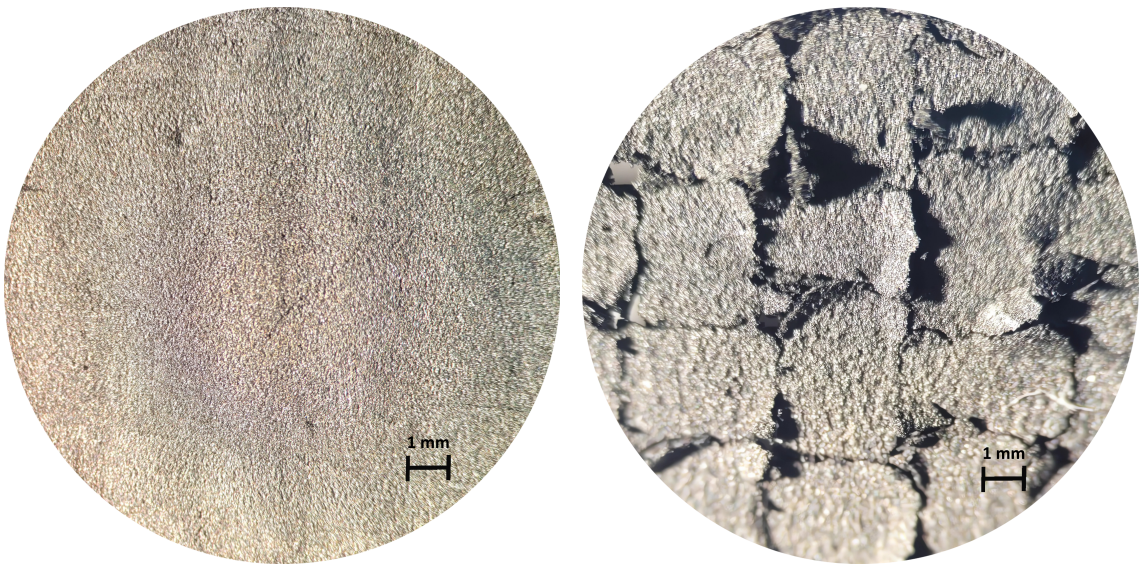

Figure 4.2: (a) Initial state of the graphene coated carbon fiber (b) Final state of the graphene coated carbon fiber after deformation.

Considering that the primary objective of the observation was to examine the surface condition rather than measure tensile strength, no quantitative measurements were recorded.

However, a displacement of 1 mm was applied during the testing process. **Figure 4.2a** showcases a section of the carbon fiber surface exhibiting a uniform graphene coating prior to deformation. Conversely, **Figure 4.2b** depicts the same sample following the tensile test, revealing noticeable delamination and loss of graphene coating, particularly in regions where fiber intersections occur. Nevertheless, it is worth noting that in areas without fiber intersections, the graphene coating exhibited good adhesion, in **Figure A.1** is shown a zoom out view. This suggests that the cathode electrodes, composed of graphene carbon fiber, possess sufficient mechanical resilience to withstand external stress and resist deformation.

4.1.2 Electrical Results

In order to assess the impact of the coating, the electrical resistance of pristine CF and CF coated with G was measured utilizing a Keysight 34461A digital multimeter. The measurement distance between the connection points was fixed at 5 cm, and a total of five samples were evaluated for each case, and 100 measurements were taken over the span of 1 minute. The outcomes of these measurements are depicted in **Figure 4.3**.

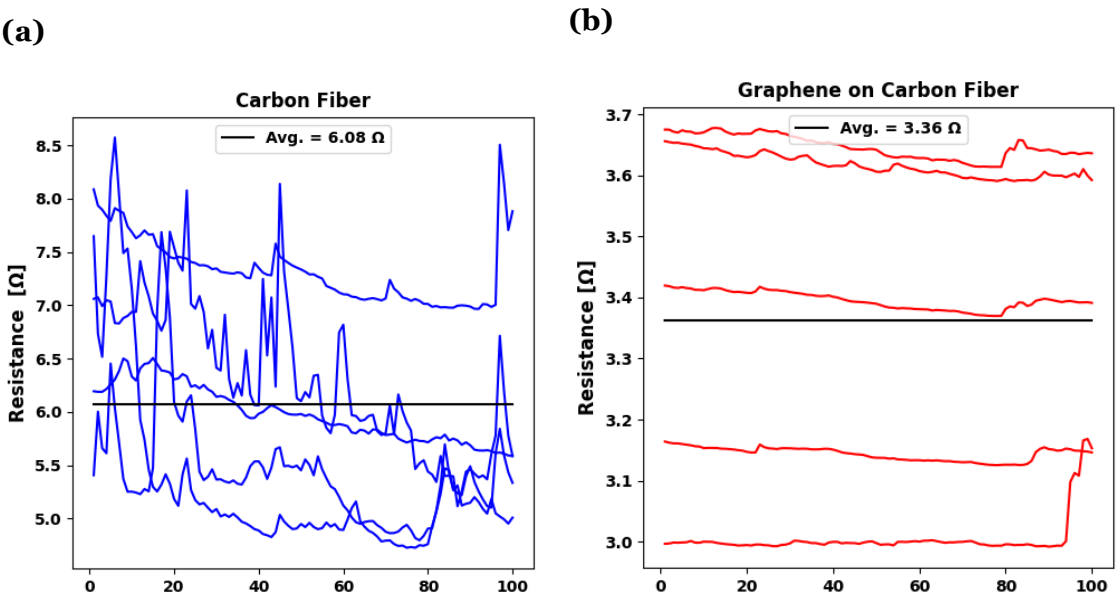

Figure 4.3: (a) Electrical resistance of pristine carbon fiber. (b) Electrical resistance of graphene coated onto carbon fiber.

From **Figure 4.3a**, it is evident that the electrical resistance of the pristine CF exhibits notable irregularity within a given sample during the measurement period. Moreover, the resistance displays considerable variation, ranging from below 5.00 to over 8.50 Ω. The average resistance obtained from 500 measurements yielded a value of 6.08 Ω.

In contrast, as depicted in **Figure 4.3b**, the coated CF demonstrates minimal resistance variance within a single sample, with resistance amplitudes ranging from 3.70 Ω to 3.00 Ω,

between all five samples. This results in an average resistance of 3.36 Ω. It is worth noting that the coated CF samples, which exhibited higher resistance, exhibited a less uniform coating of G. With an improved coating method, it may be possible to achieve a resistance as low as half of that exhibited by the pristine CF.

From this results we can conclude that the graphene coating improves the conductivity of the cathode material, as lower resistance indicates less impedance to the flow of electrons, allowing for easier electron transfer within the cathode.

4.2 Electrolyte Fabrication

During the synthesis of the IL, as said before, it was done without the glove box, and an unintended interaction between the IL mixture and, ambient air occurred, releasing a lot of gases during the manufacturing.

A test SB was specifically fabricated to investigate the interaction between the IL and the other battery components. Notably, during the vacuum infusion layup process, the IL demonstrated increased reactivity with ambient air. This reactivity resulted in the formation of solid compounds on the separator, which are difficult to observe due to their white coloration. To enhance visibility, the IL was applied on a darker material, allowing their visualization, as depicted in **Figure 4.4**. Moreover, when the electrolyte came into contact with the resin, a reaction occurred, visible due to the released gases. This effect arose due to the reaction between $AlCl_3$, a Lewis acid, and the epoxy functional group of the resin.

Minimal voltage, a few millivolts, was detected during the testing of this sample. This low voltage is likely a result of the complete reaction between the IL and the resin, occurring during the curing process under vacuum and pressure. It is probable that with further optimization of this method, such issues can be prevented.

Figure 4.4: Compound formation due to the reaction of the ionic liquid with air.

Figure 4.4 illustrates the presence of compounds formed as a result of the reaction between the IL and ambient air. The observed concentration of these compounds is relatively high, which can be attributed to the absence of specific measures aimed at minimizing their formation. However, it is important to note that appropriate measures were implemented during the battery manufacturing process to address this issue, such as minimizing the contact of the electrolyte with air, before sealing the battery.

Following the assembly of the battery, its voltage was measured using a multimeter to see the impact of the electrolyte on its performance. The average voltage recorded was approximately 1.4 V, with the highest measurement reaching around 1.65 V, as seen in **Figure A.2** in appendix. These values differ from the anticipated voltage of approximately 2 V as suggested in the literature [138]. It is important to note that while the electrolyte may not significantly affect the voltage in some batteries, the use of an organic electrolyte like $AlCl_3$-Urea can indeed influence the voltage levels. However, this might not be the sole reason, the material used in the electrodes, more specifically the G nanoplatelets could also be the reason for lower voltage.

The diminished in voltage, that may be due to the electrolyte, can be attributed to the presence of oxygen within it, which has a detrimental effect on the battery's performance. Additionally, during the voltage measurements, a noticeable decrease in voltage was observed when connected to the multimeter and other cases, even if the battery wasn't connected to anything after some time the new measured voltage would be significantly lower. Furthermore, the voltage would some times increase on it's own, both this observations show that the electrolyte wasn't stable and reactions were occurring constantly within it. This behavior can be observed in the videos provided in the supplementary materials.

Determining the exact cause of this behavior is challenging and may be attributed to various factors. Several potential reasons can be considered as potential contributors to this:

- **Chemical Reactions -** Within the battery, the presence of oxygen can initiate chemical reactions, resulting in the formation of intermediate compounds or species, as exemplified in **Figure 4.4**. These reactions have the potential to consume active species, notably aluminum ions, leading to a gradual decline in battery voltage or increase the internal resistance. However, as oxygen is consumed, oxygen-related reactions can diminish parasitic reactions and facilitate the dissolution or removal of these compounds, ultimately causing an increase in voltage.
- **Formation and Removal of Passive Layers -** When oxygen reacts with aluminum, passive oxide layers are formed on the surface of the battery electrodes. These oxide layers act as barriers, increasing the internal resistance of the battery and resulting in a decrease in voltage. However, during battery operation, these passive layers can undergo reduction or dissolution processes. This reduction or dissolution leads to a decrease in the resistance imposed by the oxide layers, allowing for improved electrochemical reactions and subsequent increase in voltage.

The aforementioned explanations regarding the internal behavior of the battery are speculative in nature, as they are based on observations and assumptions. Without conducting further tests and analysis, it is difficult to ascertain the exact cause of the observed phenomena. However, one undeniable factor contributing to these issues is the presence of oxygen within the electrolyte [139].

Based on these findings, it is crucial to employ a glove box during IL synthesis to obtain a functional electrolyte, because without it the obtained IL is very unstable. To address the issue of resin reaction, a slight modification needs to be made to the previously presented designs. For designs 1 and 2, this can be resolved by placing the electrochemical components inside an insulation bag and cutting it to the desired dimensions, thereby segregating them from the structural components. However, for design 3, achieving the same level of isolation is not straightforward, since the cathode and CF used in the structural component form a single entity. Despite this limitation, design 3 was still tested to compare its mechanical performance with the others that underwent the aforementioned modification. The layup process for all designs remains similar to the previously described process, with the exception that for designs 1 and 2, the electrochemical components are placed inside an insulation bag prior to the infusion layup process.

4.3 Structural Design Results

Three samples were tested for each design, and the results of the three-point bending tests are presented in **Figure 4.5**. Remarkably, the outcomes for the three samples of each design exhibit remarkable similarity. Notably, in **Figure 4.5a**, a discernible decrease in force is observed near the value of 400 N, although no external indications of damage are visible. This implies that the underlying cause resides within the inner layers of the samples. However, design 1 achieved a high average flexural strength of 220.6 MPa and a remarkable Young's modulus of 12.1 GPa.

In **Figure 4.5b**, a drop in force is observed close to the value of 300 N, the cause also occurring within the inner layers, similar to design 1. Design 2 achieved an average high flexural strength of 126.6 MPa and a high Young's modulus of 10.4 GPa. Moreover, one of the samples exhibits a notable decline in rigidity, despite its external resemblance to the other two. This discrepancy in mechanical properties is likely attributable to internal factors and may stem from deficiencies in the manufacturing process.

Figure 4.5c presents the results for design 3, where no drop in force occurred before the highest load. This design achieved an average high flexural strength of 396.2 MPa and a high Young's modulus of 35.7 GPa.

Table 4.1 summarizes the mechanical results and thickness of the three designs. From the table, it can be observed that design 1 and design 2 share similar thickness and Young's modulus values. However, design 1 achieved nearly double the maximum flexural strength,

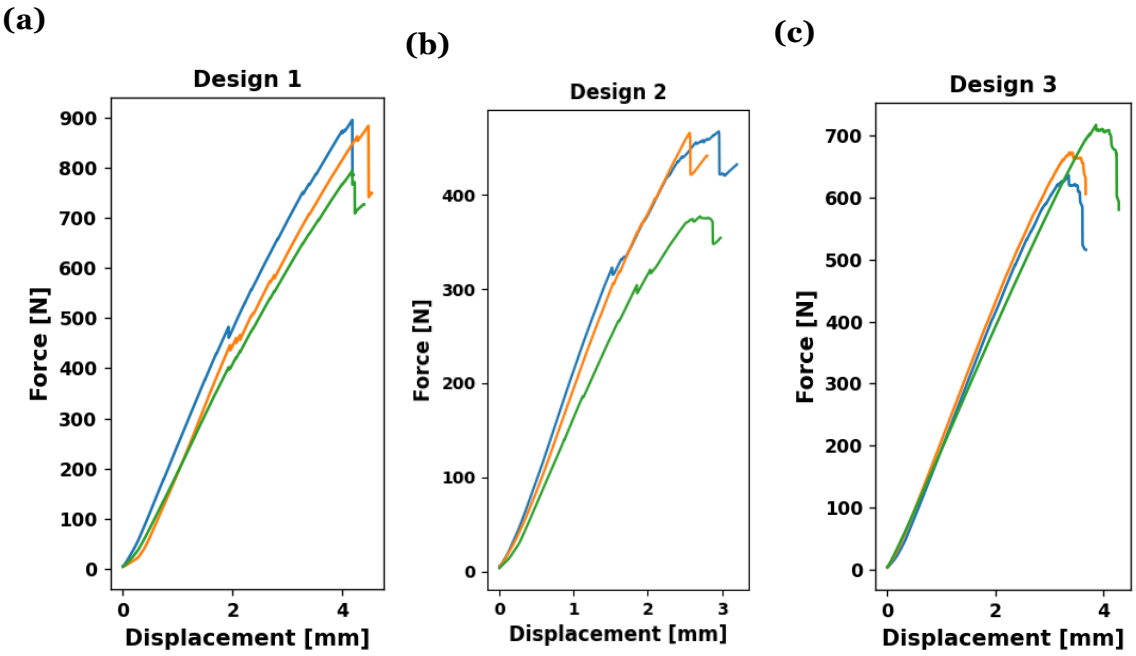

Figure 4.5: Three-point bending tests (a) Design 1. (b) Design 2. (c) Design 3.

indicating that insulating the tabs using a polymer and enhancing defects and interfaces is a more advantageous approach than using GF. On the other hand, design 3 outperformed the previous two designs significantly. It possessed a thinner profile, a flexural strength surpassing design 1 by more than twofold, and a Young's modulus almost three times higher than the other designs. If design 3 were entirely composed of CF and the tab insulation were implemented similarly to design 1, even better results could be attained.

Table 4.1: Summary of the results of the three-point bending test for the three structural battery designs.

Design	Thickness [mm]	Flexural Strength [MPa]	Young's Modulus [GPa]
1	2.2 ± 0.1	220.6 ± 22.6	12.1 ± 1.8
2	2.1 ± 0.1	126.6 ± 7.44	10.4 ± 1.1
3	1.5 ± 0.1	396.2 ± 53.3	35.7 ± 1.6

In order to investigate the underlying cause of the force reduction observed during the testing, the samples were meticulously sectioned and subjected to microscopic examination, as depicted in **Figure 4.6**.

The examination of **Figure 4.6** provides valuable insights into the structural integrity of the different designs. It is notable that no significant cracking is observed in any of the designs, indicating that the observed decrease in force during the test is likely attributed to delamination between the various layers. Specifically, for design 1 and 2, delamination is expected to occur between the insulation bag and the fibers, while for design 3, it is anticipated to occur between the separator and the fibers.

Another noteworthy observation is the considerable contribution of the separator and

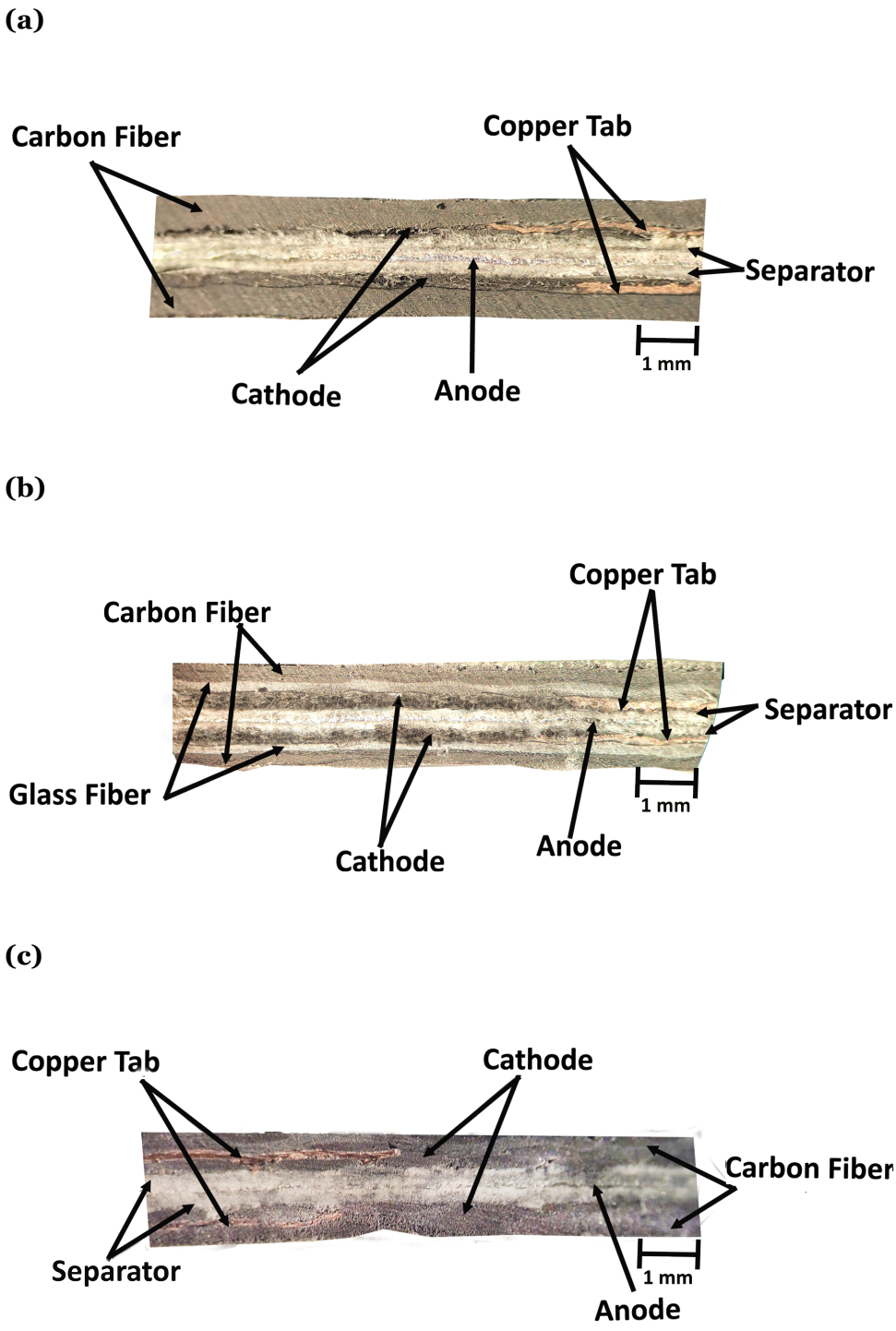

Figure 4.6: Microscopic view of the structural batteries designs after testing. (a) Design 1. (b) Design 2. (c) Design 3.

cathode to the overall thickness of the structural battery. From the analysis of **Figure 4.6a** and **Figure 4.6b**, it is evident that the electrochemical components can be visually distinguished with clarity, along with the interfaces between these components and the

structural elements. However, in the case of design 3, as depicted in **Figure 4.6c**, the cathode is not clearly observable, consequence of a more seamless integration of the cathode within the structural component. Its location can be inferred from the presence of the Cu tab, which indicates its positioning. It is worth noting that incorporating the G coating could potentially facilitate its visualization, moreover the GF is not visible is this section that's why is not indicated.

The present finding serves to strengthen the concept that by introducing minor adjustments to the traditional arrangement of structural batteries, it is possible to enhance their mechanical capabilities. However, to achieve this, it is essential to ensure that the electrolyte does not undergo any adverse reactions with the resin, and that the stacking process does not result in electrical insulation caused by resin coating the electrodes.

It is crucial to emphasize that the results obtained from these designs should not be regarded as definitive representations of the ultimate performance of the structural battery, as the incorporation of G and the IL was not implemented in this particular evaluation.

4.4 Structural Battery Results

Among the designs evaluated in the previous subsection, design 1 emerged as the optimal choice due to its superior performance. Design 3 was excluded from consideration due to its inability to isolate electrochemical components from structural elements. After meticulously following the procedures outlined in the preceding section, the electrochemical component and the fully assembled structural battery were successfully fabricated. As depicted in **Figure 4.7a**, the electrochemical component, enclosed within a sealing pouch, was meticulously prepared. Subsequently, this component was carefully inserted into the structural component, resulting in the completion of the structural battery, as illustrated in **Figure 4.7b**.

It is worth noting that the electrochemical component, comprising the sealing pouch and insulation tape, has an average mass of 5.8 g. In contrast, the entire assembled battery weighs approximately 30 g, encompassing both the electrochemical component and the structural components.

4.4.1 Electrochemical

As mentioned earlier, the defective electrolyte hindered the execution of comprehensive electrochemical tests, such as cyclic voltammetry, charge-discharge cycling, and capacity measurements, because when the battery was connected to the equipment during discharge test, even for a current of 0.1 A, the voltage would drop instantly to zero. However, in order to validate the concept of an aluminum-ion structural battery and demonstrate its energy storage capability akin to conventional batteries, a practical demonstration was

(a) **(b)**

Figure 4.7: (a) Assembled electrochemical component. (b) Assembled structural battery.

conducted by connecting it to different color LEDs. **Figure 4.8** illustrates the experimental setup employed to establish the connection with the LEDs, thereby showcasing the battery's functionality. The utilization of LEDs with varying colors stems from their distinctive voltage requirements.

To perform the experiment, four SBs were connected in series to achieve a combined voltage suitable for activating different colored LEDs. As mentioned earlier, each SB had an average voltage of 1.4 V immediately after manufacturing, with a maximum voltage of 1.65 V. However, it should be noted that the voltage exhibited significant fluctuations.

Consequently, the total voltage obtained from the series connection was 4.49 V, as depicted in **Figure 4.8a**. It is important to mention that in normal circumstances, without any issues related to the IL, the voltage of each SB would be expected to be around 2 V, as mentioned earlier, resulting in a total voltage of approximately 8 V, which would be sufficient to power a small electric motor.

In **Figure 4.8a**, the green crocodile clip on the right side initially remained disconnected from the SBs but was connected to the LED. Upon connecting it to the SBs, as illustrated in **Figure 4.8b** to **Figure 4.8e**, the LEDs were observed to illuminate. A video demonstration of this procedure can be found in the supplementary materials.

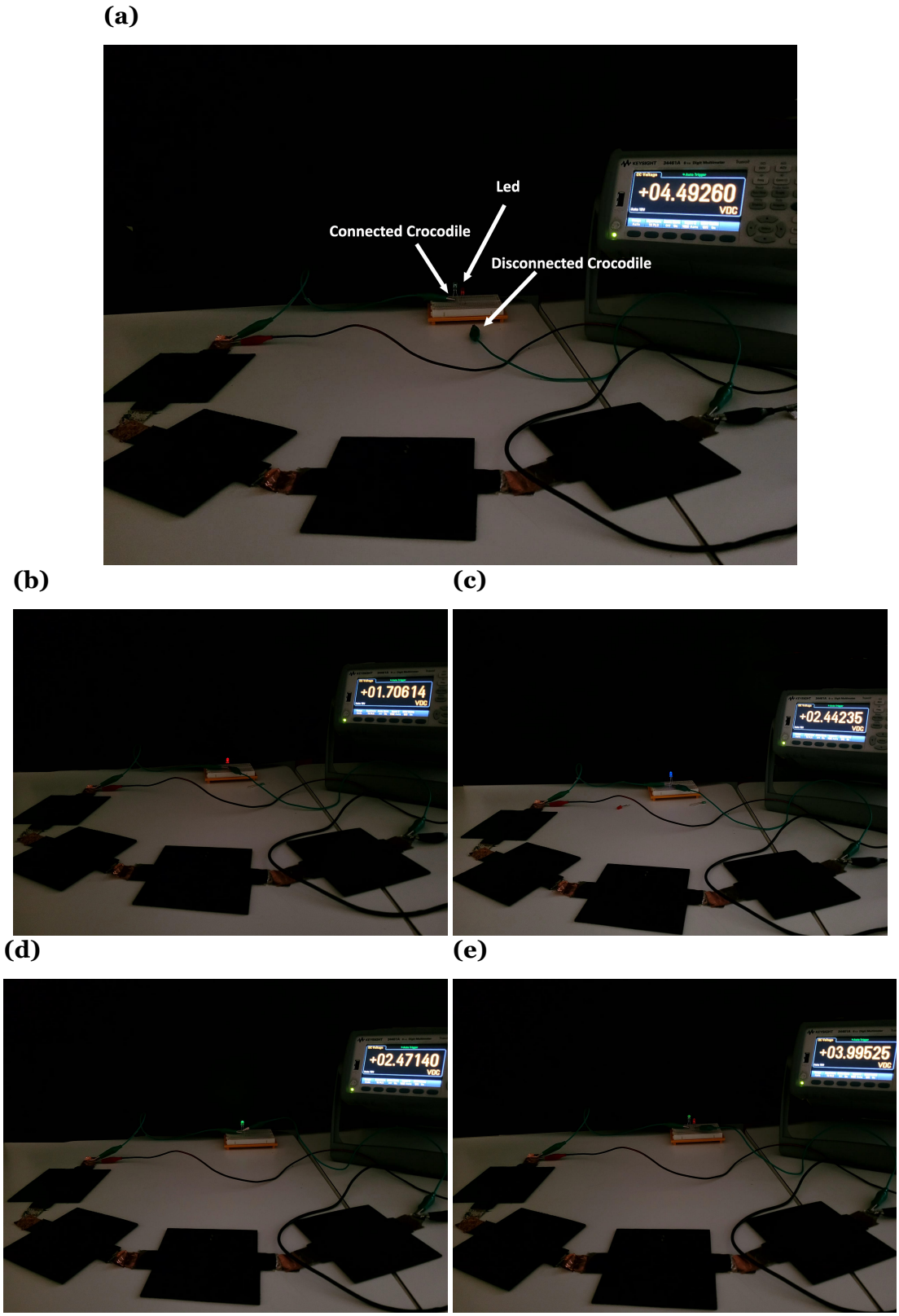

Figure 4.8: Powering a LED with the structural batteries (a) Disconnected LED. (b) Light up red LED. (c) Light up blue LED. (d) Light up green LED. (e) Light up red and green LED.

As depicted in **Figures 4.8b**, **4.8c**, and **4.8d**, it was possible to light up red, blue, and green LEDs, respectively, although with low intensity. Furthermore, by connecting a red and green LED in series, both were able to be lit, albeit with even lower intensity, **Figure 4.8e**.

As previously mentioned, the internal resistance was calculated using the method described earlier. In this calculation, a resistor with a value of 210 Ω was utilized. When measuring the voltage across the resistor, it was observed to be in the range of a few millivolts, meaning the drop in voltage across it was almost the total voltage of the battery. However, rather than stabilizing, the voltage readings continued to decrease over time. This behavior indicates that the internal resistance of the battery is exceptionally high.

Based on this result, it can be inferred that the previous assumptions regarding the structural battery's high internal resistance due to the presence of intermediate compounds or oxide layers are likely valid. These factors can account for the observed voltage drop when the battery is connected to the multimeter, as well as the fluctuations in voltage.

4.4.2 Mechanical

In accordance with the preceding chapter, a series of three-point bending tests were conducted, employing support spans set at a length of 75 mm. Throughout these tests, voltage and resistance measurements were acquired utilizing a multimeter. In order to establish a benchmark for evaluating the SB's performance, a CFRP specimen, containing an equal number of layers as the structural battery, eight layers of carbon fibers, was fabricated and subjected to the same experimental conditions. Alongside performance comparisons, additional properties including mass and thickness were also evaluated.

In **Figure 4.9a**, the mechanical test results for the SB and CFRP are depicted. The plotted lines represent the average values obtained from all samples for each case.

As expected, the CFRP exhibited superior performance. It achieved a Young's Modulus of 70.1 GPa and a flexural strength of 843.6 MPa, while the SB attained only 19.1 GPa and 247.5 MPa, respectively.

Furthermore, comparing the SB's mechanical performance to other structural batteries in **Figure 4.9b**, it is evident that the results are at the higher end of the spectrum. Despite being lower than the CFRP, the SB demonstrates promising mechanical properties within the context of structural batteries. This is a result of the integration of the electrochemical component on the structural component with eight layers of CFs, naturally leading to a reduction in specific energy due to the increased weight.

It is noteworthy that, similar to the previous designs, no external cracking was observed, indicating that the failure was internally. The delamination between the structural component and the electrochemical component was identified as the underlying cause, con-

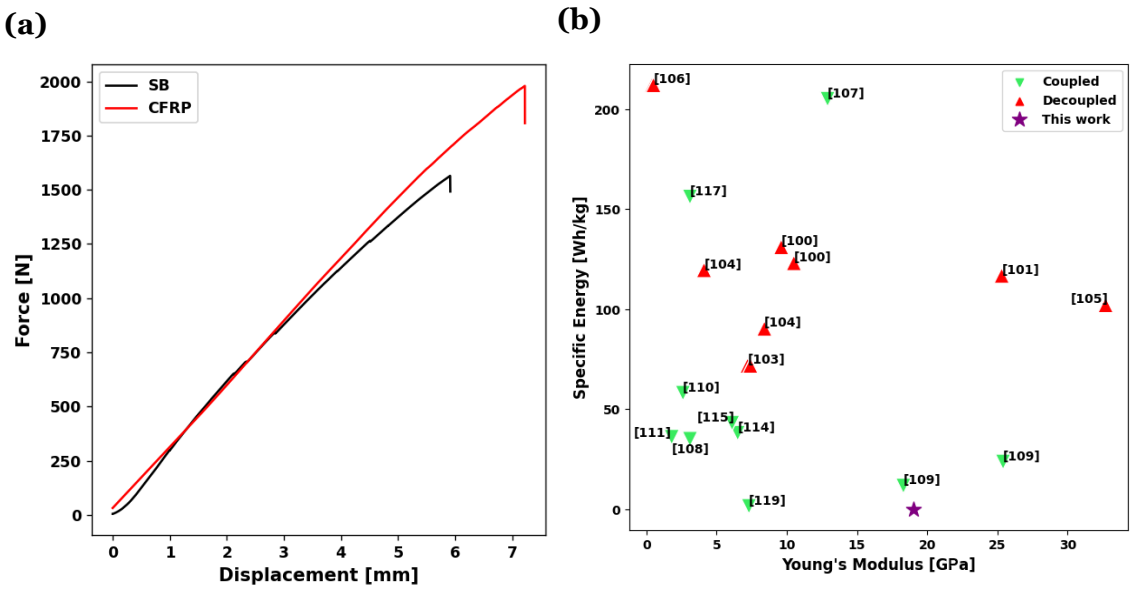

Figure 4.9: (a) Results of the three-point bending test for the structural battery and the carbon fiber composite. (b) Comparison of the performance of this work's structural battery and previous works.

sistent with the behavior observed in the earlier designs.

Intriguingly, even after the structural component of the SB failed, there was no noticeable change in voltage. This indicates that the electrochemical component remained intact and capable of withstanding higher loads and deformations. Another surprising finding was the no change in the resistance measured with a multimeter, even after a displacement of 5 mm. Although it does not represent the internal resistance, this observation provides valuable insights into the behavior of the SB under load. This results can be observed in **Figure 4.10**.

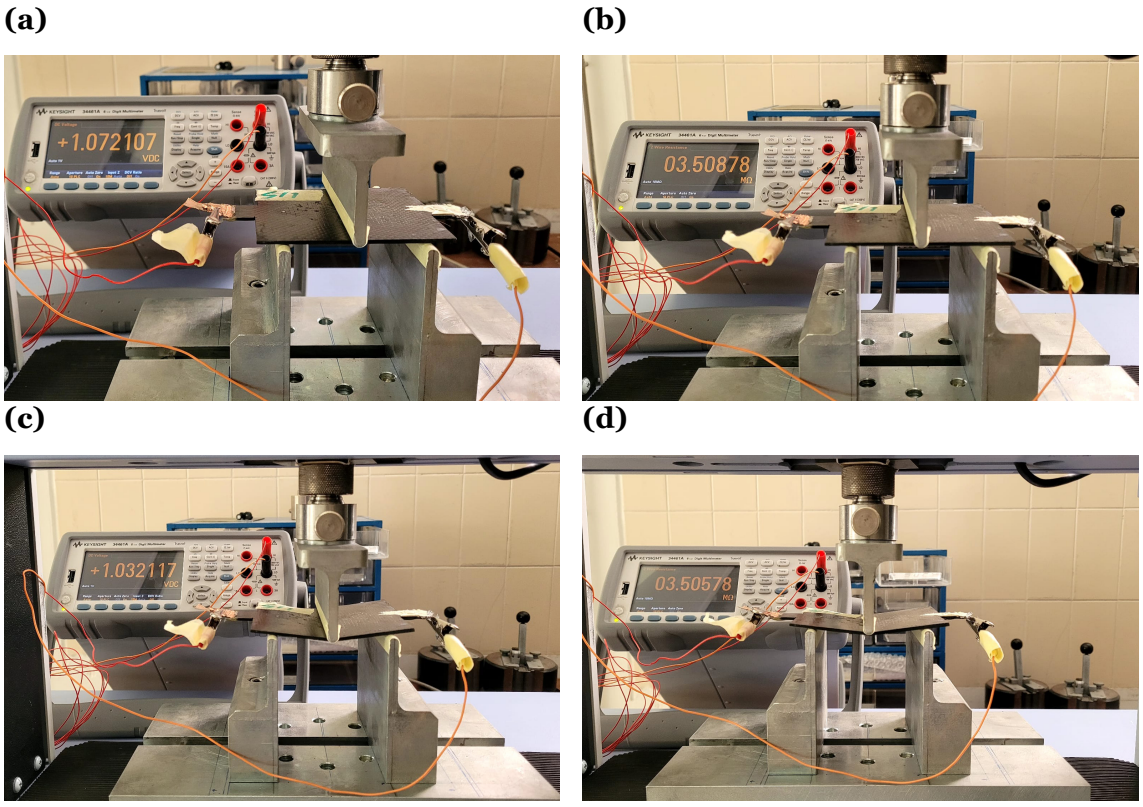

Figure 4.10: [Measured structural battery: (a) voltage under 0 mm displacement (1.07 V); (b) resistance under 0 mm displacement (3.51 MΩ); (c) voltage under 5 mm displacement (1.03 V); (d) resistance under 5 mm displacement (3.51 MΩ).

From **Figures 4.10a** and **4.10c**, one can discern a marginal alteration in the battery's voltage, even following a displacement of 5 mm and an applied load of 1 000 N. This observation highlights the continued functionality of the battery under these conditions. Additionally, **Figures 4.10b** and **4.10d** depict the nearly constant nature of the electrical resistance.

To provide a comprehensive overview, **Table 4.2** presents all the test results and physical measurements for the SB and CFRP. Notably, the integration of the electrochemical component resulted in a relatively modest 30 % increase in mass. However, the thickness nearly doubled, with a substantial 69 % increase compared to the CFRP. Given that the primary purpose of the SB is to function as a structural element in space-constrained environments, this significant increase in thickness poses a challenge. However, it is important to highlight that even with the increased thickness, the SB still offers significant space-saving advantages compared to conventional batteries.

Table 4.2: Summary of the results of the three-point bending test for the developed structural battery and CFRP.

Sample	**Thickness [mm]**	**Mass [g]**	**Flexural Strength [MPa]**	**Young's Modulus [GPa]**
CFRP	1.6 ± 0.2	23.5 ± 2.3	843.6 ± 37.5	70.1 ± 5.1
SB	2.7 ± 0.3	30.7 ± 2.3	247.5 ± 34.1	19.1 ± 4

In summary, the mechanical test results indicate that the SB falls short of the CFRP in terms of performance. However, when evaluated among other structural batteries, the SB demonstrates competitive mechanical properties. The internal delamination issue remains a concern but does not compromise the functionality of the electrochemical component. The mass increase due to integration is relatively modest, while the thickness increase poses challenges in space-limited applications.

Chapter 5

Conclusions and Future Work

5.1 Conclusions

The degradation and environmental destruction have compelled society to prioritize environmental care, leading to the pursuit of sustainable solutions to meet our everyday needs and mitigate further damage. One such solution is the replacement of conventional combustion engines in vehicles with alternative power sources, with electricity being the most sought after.

In light of this, the investigation into energy storage devices has intensified, with particular emphasis on enhancing electric vehicle efficiency. Structural batteries have emerged as a promising solution, being the focus of this work, prompting a thorough review of different types and their impact on electric vehicle performance. To facilitate the selection of an appropriate chemistry for the design of a structural battery, fundamental knowledge about batteries and commonly used chemistries was acquired, along with a consideration of their respective advantages and disadvantages.

Once a satisfactory level of understanding and knowledge had been attained, an aluminum-ion structural battery reinforced with carbon fibers was chosen as the subject for development and study.

Throughout this endeavor, numerous challenges were encountered, and corresponding solutions were devised. The experimental procedure encompassed the step-by-step manufacturing of different components of the structural battery, including the cathode, electrolyte, and layup process.

For the fabrication of the cathode, graphene coating onto carbon fibers was essential, and two methods were tested: (1) spraying a solvent and graphene solution, and (2) applying a slurry of graphene, binder, and solvent. The latter approach yielded superior results, exhibiting a greater reduction in electrical resistance of the pristine carbon fibers and improved adherence.

In terms of electrolyte fabrication, an ionic liquid consisting of $AlCl_3$-Urea was chosen due to its advantages in safety, cost-effectiveness, and rechargeability. However, challenges were encountered during the manufacturing process, as a required glove box was not utilized, resulting in contamination of the ionic liquid with oxygen. Nonetheless, a functional ionic liquid was successfully produced.

In the layup process of the structural battery, three designs were evaluated to determine the one with most favorable mechanical results. Despite encountering issues with the best design's compatibility with the ionic liquid, a functional structural battery was successfully produced. The resolution of these compatibility issues may be achievable through the execution of additional tests aimed at optimizing the manufacturing process.

During the three-point bending test, the structural battery exhibited a Young's modulus of $\approx$ 19 GPa and a flexural strength of $\approx$ 248 MPa. Comparisons with other works indicated commendable results in terms of the Young's modulus, although performance fell short when compared to a pure CFRP with the same fiber content, suggesting the need for further improvements in the layup process. However, in terms of electrochemical performance, the extremely high internal resistance prevented charge and discharge cycles, thereby impeding the measurement of specific energy. Nevertheless, the developed structural battery demonstrated the ability to illuminate LEDs of different colors and achieved an average voltage of 1.4 V, underscoring its potential as an energy storage device. Furthermore, the causes of the high internal resistance are known, as well as the solution.

Although a comprehensive assessment of its electrochemical performance and multifunctionality was hindered, the mechanical tests provided valuable insights. Minimal changes in the batteries internal resistance were observed under a 1 000 N of load, corresponding to a 6 mm displacement. Additionally, even when the structural component failed, the voltage remained constant, indicating the structural integrity of the reinforced electrochemical component and its capability to withstand higher loads.

In terms of its application in the aeronautical sector, the structural battery developed thus far requires substantial improvement before it can become a viable option. Nevertheless, it exhibits promising potential for implementation in fuselage panels and wing panels. Being an aluminum-ion battery, its lifespan has the potential to exceed that of the structures themselves. This implies that there would be no necessity to replace an entire structure solely due to the battery reaching the end of its life.

In conclusion, structural batteries present a promising solution for more efficient electric vehicles and the accelerated development of electric aircraft. Overall, this work successfully achieved its intended objectives, culminating in the successful fabrication of a functional structural battery capable of withstanding loads and storing energy. While the detailed electrochemical tests were not fully completed, the outcomes so far have been highly encouraging.

5.2 Future Work

Considering the comprehensive research undertaken in this dissertation, it is evident that there are numerous avenues for further exploration in the field of structural batteries for aeronautical and aerospace applications. The following topics are proposed as future re-

search directions:

- **Alternative Electrode Manufacturing Processes -** In order to enhance the mechanical performance of the cathode, the consideration of electrodeposition as an alternative fabrication method should be explored. This technique has the potential to yield improvements in the cathode's mechanical properties. Similarly, for the anode, infiltrating or deposition aluminum onto fibers could offer opportunities to enhance its mechanical performance. These alternative approaches hold promise for achieving superior mechanical characteristics in both electrodes.
- **Evaluation of Electrochemical Performance -** Future studies should prioritize the optimization of the electrolyte manufacturing process employed in this work or explore alternative electrolyte materials, including solid and semi-solid electrolytes. By evaluating different electrolyte options, the aim is to enhance the electrochemical and mechanical performance of the structural battery.
- **Enhancement of Mechanical Performance -** Further experimentation is warranted to explore additional layup designs for the structural battery, such as making the electrochemical component of fibers only. Additionally, alternative configurations, such as a sandwich composite configuration, should be investigated to assess their potential for improving the mechanical performance of the battery.
- **Digital Twin Analysis -** For an in-depth evaluation of the electric aircraft's performance when structural components and batteries are substituted with structural batteries, it is highly advisable to conduct an extensive numerical analysis. This comprehensive analysis promises to offer invaluable insights into the feasibility and potential advantages of integrating structural batteries into electric aircraft systems. The analysis should encompass structural, electrical, and electrochemical assessments, along with a LCA of the battery itself.
- **Performance Under Extreme Conditions -** Considering that some electric vehicles often operate in extreme conditions, such as negative and high temperatures, it is essential to investigate the impact of these conditions on the performance of the structural battery. Future work should aim to assess the battery's behavior and performance under challenging environmental conditions, enabling a comprehensive understanding of its capabilities and limitations.

By addressing these future research directions, the potential for advancements in the field of structural batteries can be realized. These investigations will contribute to the refinement and development of high-performance structural battery systems, paving the way for their broader application in various industries, including aeronautics and aerospace.

Bibliography

[1] Climate change: what the EU is doing. Date accessed: 22 January 2023. [Online]. Available: https://www.consilium.europa.eu/en/policies/climate-change/ 1

[2] The 17 goals | sustainable development. Date accessed: 29 January 2023. [Online]. Available: https://sdgs.un.org/goals 1

[3] H. Ritchie, M. Roser, and P. Rosado, "CO2 and Greenhouse Gas Emissions," *Our World in Data*, 2020. [Online]. Available: https://ourworldindata.org/co2-and-other-greenhouse-gas-emissions 1

[4] "Global energy-related co2 emissions by secto – charts – data and statisticsr – charts – data and statistics," 2022, Date accessed: 22 January 2023. [Online]. Available: https://www.iea.org/data-and-statistics/charts/global-energy-related-co2-emissions-by-sector 1

[5] "Global energy-related co2 emissions by sector in 2020 and 2050 – charts – data and statistics," 2022, Date accessed: 22 January 2023. [Online]. Available: https://origin.iea.org/data-and-statistics/charts/global-energy-related-co2-emissions-by-sector-in-2020-and-2050 1

[6] T. Duffy, "All these car brands are going electric soon," 2022, Date accessed: 22 January 2023. [Online]. Available: https://www.gearpatrol.com/cars/g38986745/car-brands-going-electric/?slide=10 1

[7] B. A. Adu-Gyamfi and C. Good, "Electric aviation: A review of concepts and enabling technologies," *Transportation Engineering*, vol. 9, p. 100134, 2022. [Online]. Available: https://www.sciencedirect.com/science/article/pii/S2666691X2200032X 1

[8] A. Jay, "Number of flights worldwide in 2022/2023: Passenger traffic, behaviors, and revenue," 2023, Date accessed: 22 January 2023. [Online]. Available: https://financesonline.com/number-of-flights-worldwide/ 1

[9] "Aviation research center switzerland," Date accessed: 22 January 2023. [Online]. Available: https://www.arcs.aero/sites/default/files/downloads/Bericht_Flightpath_2050.pdf 1

[10] E. Gofman, "Energy density of aviation fuel," 2003, Date accessed: 25 January 2023. [Online]. Available: https://hypertextbook.com/facts/2003/EvelynGofman.shtml 2

[11] L. Li, "Energy density of solid-state battery reached 500 wh-kg," 2022, Date accessed: 25 January 2023. [Online]. Available: https://www.takomabattery.com/energy-density-of-solid-state-battery-reached-500/ 2, 17

[12] "Nims researchers report 500 wh/kg+ li-air battery," 2022, Date accessed: 25 January 2023. [Online]. Available: https://www.greencarcongress.com/2022/01/20220124-nims.html 2

[13] O. L. Li and T. Ishizaki, "Chapter 4 - development, challenges, and prospects of carbon-based electrode for lithium-air batteries," in *Emerging Materials for Energy Conversion and Storage*, K. Y. Cheong, G. Impellizzeri, and M. A. Fraga, Eds. Elsevier, 2018, pp. 115–152. [Online]. Available: https://www.sciencedirect.com/science/article/pii/B9780128137949000041 2, 17

[14] Cityairbus demonstrator. Date accessed: 25 January 2023. [Online]. Available: https://www.airbus.com/en/urbanairmobility/cityairbus-nextgen/cityairbus-demonstrator 2

[15] Verdict media limited. Date accessed: 25 January 2023. [Online]. Available: https://www.aerospace-technology.com/projects/extra-330le-electric-aircraft/ 2

[16] W. P. I. JP Thomas, SM Qidwai and G. Pham, "Multifunctional structure-battery composites for marine systems," *Journal of Composite Materials*, vol. 47, 2012. [Online]. Available: https://journals.sagepub.com/doi/10.1177/0021998312460262 2

[17] W. Johannisson, D. Zenkert, and G. Lindbergh, "Model of a structural battery and its potential for system level mass savings," *Multifunctional Materials*, vol. 2, p. 035002, 9 2019. [Online]. Available: https://dx.doi.org/10.1088/2399-7532/ab3bdd 2, 27, 28, 29

[18] D. Carlstedt and L. E. Asp, "Performance analysis framework for structural battery composites in electric vehicles," *Composites Part B: Engineering*, vol. 186, p. 107822, 2020. [Online]. Available: https://www.sciencedirect.com/science/article/pii/S1359836819351509 2, 29, 30, 31, 32, 75

[19] L. E. Asp, M. Johansson, G. Lindbergh, J. Xu, and D. Zenkert, "Structural battery composites: a review," *Functional Composites and Structures*, vol. 1, no. 4, p. 042001, nov 2019. [Online]. Available: https://dx.doi.org/10.1088/2631-6331/ab5571 2, 45

[20] G. Lim, K. Chan, N. Sutrisnoh, and M. Srinivasan, "Design of structural batteries: carbon fibers and alternative form factors," *Materials Today Sustainability*, vol. 20, p. 100252, 2022. [Online]. Available: https://www.sciencedirect.com/science/article/pii/S2589234722001440 3, 44, 45

[21] N. S. Muhammed Hafiz, G. Singla, and P. Kumar Jha, "Next generation sodium-ion battery: A replacement of lithium," *Materials Today: Proceedings*, 2022. [Online]. Available: https://www.sciencedirect.com/science/article/pii/S2214785322070961 5, 21

[22] J. Zhang, L. Zhang, F. Sun, and Z. Wang, "An overview on thermal safety issues of lithium-ion batteries for electric vehicle application," *IEEE Access*, vol. PP, pp. 1–1, 05 2018. 6

[23] J. A. Talbot and Peter. The history and development of batteries. Date accessed: 03 February 2023. [Online]. Available: https://phys.org/news/2015-04-history-batteries.html 5

[24] S. Terry, "Early electric battery, 1850 - stock image - v510/0062." [Online]. Available: https://www.sciencephoto.com/media/363826/view/early-electric-battery-1850 6

[25] Components of cells and batteries. Date accessed: 05 February 2023. [Online]. Available: https://depts.washington.edu/matseed/batteries/MSE/components.html 7, 9

[26] E. Vergori, F. Mocera, and A. Soma, "Battery modelling and simulation using a programmable testing equipment," *Computers*, vol. 7, p. 20, 03 2018. 8

[27] J. Shepard. Li-ion batteries, part 4: Separators. Date accessed: 05 February 2023. [Online]. Available: https://www.batterypowertips.com/li-ion-batteries-part-4-separators-faq/ 8

[28] W. Luo, S. Cheng, M. Wu, X. Zhang, D. Yang, and X. Rui, "A review of advanced separators for rechargeable batteries," *Journal of Power Sources*, vol. 509, p. 230372, 2021. [Online]. Available: https://www.sciencedirect.com/science/article/pii/S0378775321008831 9

[29] X. Han, Y. Bai, R. Zhao, Y. Li, F. Wu, and C. Wu, "Electrolytes for rechargeable aluminum batteries," *Progress in Materials Science*, vol. 128, p. 100960, 2022. [Online]. Available: https://www.sciencedirect.com/science/article/pii/S007964252200041X 9, 19, 20, 73

[30] L. Wang, J. Li, G. Lu, W. Li, Q. Tao, C. Shi, H. Jin, G. Chen, and S. Wang, "Fundamentals of electrolytes for solid-state batteries: Challenges and perspectives," *Frontiers in Materials*, vol. 7, 2020. [Online]. Available: https://www.frontiersin.org/articles/10.3389/fmats.2020.00111 9

[31] Z. Zhang and V. G. Pol, "Understanding the thermal safety of solid-state lithium battery: An in-situ thermal study," *ECS Meeting Abstracts*, vol. MA2020-02, no. 5, p. 880, nov 2020. [Online]. Available: https://dx.doi.org/10.1149/MA2020-025880mtgabs 9

[32] C. Morris. Are solid-state batteries always safer than li-ion? Date accessed: 05 February 2023. [Online]. Available: https://chargedevs.com/newswire/are-solid-state-batteries-always-safer-than-li-ion/ 10

[33] "Section 3 - sealed nickel-cadmium cells and batteries," in *Rechargeable Batteries Applications Handbook*, ser. EDN Series for Design Engineers. Newton: Newnes, 1998, pp. 35–151. [Online]. Available: https://www.sciencedirect.com/science/article/pii/B9780750670067500048 10

[34] A guide to understanding battery specifications - mit. Date accessed: 26 February 2023. [Online]. Available: http://web.mit.edu/evt/summary_battery_specifications.pdf 10

[35] J. Shepard. The difference between primary and secondary battery chemistries. Date accessed: 07 February 2023. [Online]. Available: https://www.batterypowertips.com/difference-between-primary-secondary-battery-chemistries-faq/ 13, 14

[36] Primary batteries. Date accessed: 07 February 2023. [Online]. Available: https://www.amicell.co.il/batteries-primary-batteries/ 13

[37] Advantages and disadvantages of primary batteries: Electricity - magnetism. Date accessed: 07 February 2023. [Online]. Available: https://www.electricity-magnetism.org/electric-battery/advantages-and-disadvantages-of-primary-batteries/ 13

[38] Secondary batteries. Date accessed: 07 February 2023. [Online]. Available: https://www.doitpoms.ac.uk/tlplib/batteries/secondary.php 14

[39] Difference between primary cell and secondary cell. Date accessed: 07 February 2023. [Online]. Available: https://www.vedantu.com/chemistry/difference-between-primary-cell-and-secondary-cell 14

[40] List of battery types. Date accessed: 07 February 2023. [Online]. Available: https://en.wikipedia.org/wiki/List_of_battery_types 14

[41] [Online]. Available: https://www.epectec.com/batteries/cell-comparison.html 15

[42] ™ aluminium-ion battery. Date accessed: 28 February 2023. [Online]. Available: https://graphenemg.com/energy-storage-solutions/aluminum-ion-battery/ 14

[43] Catl unveils its latest breakthrough technology by releasing its first generation of sodium-ion batteries. Date accessed: 28 February 2023. [Online]. Available: https://www.catl.com/en/news/665.html 14

[44] N. Nitta, F. Wu, J. T. Lee, and G. Yushin, "Li-ion battery materials: present and future," *Materials Today*, vol. 18, no. 5, pp. 252–264, 2015. [Online]. Available: https://www.sciencedirect.com/science/article/pii/S1369702114004118 15

[45] Lithium bateries. Date accessed: 22 February 2023. [Online]. Available: https://www.doitpoms.ac.uk/tlplib/batteries/batteries_lithium.php 15

[46] W. Cao, J. Zhang, and H. Li, “Batteries with high theoretical energy densities,” *Energy Storage Materials*, vol. 26, pp. 46–55, 2020. [Online]. Available: https://www.sciencedirect.com/science/article/pii/S240582971931102X 15

[47] R. B. Kaunda, “Potential environmental impacts of lithium mining,” *Journal of Energy & Natural Resources Law*, vol. 38, no. 3, pp. 237–244, 2020. [Online]. Available: https://doi.org/10.1080/02646811.2020.1754596 15

[48] W. Liu, D. B. Agusdinata, and S. W. Myint, “Spatiotemporal patterns of lithium mining and environmental degradation in the atacama salt flat, chile,” *International Journal of Applied Earth Observation and Geoinformation*, vol. 80, pp. 145–156, 2019. [Online]. Available: https://www.sciencedirect.com/science/article/pii/S0303243419300996 15

[49] M. Armstrong and F. Richter. (2022, Nov) Infographic: The great lithium boom. Date accessed: 12 February 2023. [Online]. Available: https://www.statista.com/chart/28037/lithium-carbonate-price-timeline 16

[50] L. Wang, Z. Wu, J. Zou, P. Gao, X. Niu, H. Li, and L. Chen, “Li-free cathode materials for high energy density lithium batteries,” *Joule*, vol. 3, no. 9, pp. 2086–2102, 2019. [Online]. Available: https://www.sciencedirect.com/science/article/pii/S2542435119303551 17

[51] Y. Li, J. G. Shapter, H. Cheng, G. Xu, and G. Gao, “Recent progress in sulfur cathodes for application to lithium–sulfur batteries,” *Particuology*, vol. 58, pp. 1–15, 2021. [Online]. Available: https://www.sciencedirect.com/science/article/pii/S1674200121000407 17

[52] E. Cha, M. D. Patel, J. Park, J. Hwang, V. Prasad, K. Cho, and W. Choi, “2d mos2 as an efficient protective layer for lithium metal anodes in high-performance li–s batteries,” *Nature Nanotechnology*, vol. 13, no. 4, pp. 337–344, Apr 2018. [Online]. Available: https://doi.org/10.1038/s41565-018-0061-y 17

[53] X. Fan, E. Hu, X. Ji, Y. Zhu, F. Han, S. Hwang, J. Liu, S. Bak, Z. Ma, T. Gao, S.-C. Liou, J. Bai, X.-Q. Yang, Y. Mo, K. Xu, and C. Su, Dongand Wang, “High energy-density and reversibility of iron fluoride cathode enabled via an intercalation-extrusion reaction,” *Nature Communications*, vol. 9, no. 1, p. 2324, Jun 2018. [Online]. Available: https://doi.org/10.1038/s41467-018-04476-2 17

[54] S. Matsuda, M. Ono, S. Yamaguchi, and K. Uosaki, “Criteria for evaluating lithium–air batteries in academia to correctly predict their practical performance in industry,” *Mater. Horiz.*, vol. 9, pp. 856–863, 2022. [Online]. Available: http://dx.doi.org/10.1039/D1MH01546J 17

[55] J. Xia, Z. Wang, N. D. Rodrig, B. Nan, J. Zhang, W. Zhang, B. L. Lucht, C. Yang, and C. Wang, “Super-reversible cuf2 cathodes enabled by cu2+-coordinated alginate,”

Advanced Materials, vol. 34, no. 43, p. 2205229, 2022. [Online]. Available: https://onlinelibrary.wiley.com/doi/abs/10.1002/adma.202205229 17

[56] Aluminum2023 data - 1989-2022 historical - 2024 forecast - price - quote - chart. Date accessed: 28 February 2023. [Online]. Available: https://tradingeconomics.com/commodity/aluminum 17

[57] T. Leisegang, F. Meutzner, M. Zschornak, W. Münchgesang, R. Schmid, T. Nestler, R. A. Eremin, A. A. Kabanov, V. A. Blatov, and D. C. Meyer, "The aluminum-ion battery: A sustainable and seminal concept?" *Frontiers in Chemistry*, vol. 7, 2019. [Online]. Available: https://www.frontiersin.org/articles/10.3389/fchem.2019.00268 17, 19

[58] G. A. Elia, K. Marquardt, K. Hoeppner, S. Fantini, R. Lin, E. Knipping, W. Peters, J.-F. Drillet, S. Passerini, and R. Hahn, "An overview and future perspectives of aluminum batteries," *Advanced Materials*, vol. 28, no. 35, pp. 7564–7579, 2016. [Online]. Available: https://onlinelibrary.wiley.com/doi/abs/10.1002/adma.201601357 18

[59] W. C. Tan, L. H. Saw, M. C. Yew, D. Sun, Z. Cai, W. T. Chong, and P.-Y. Kuo, "Analysis of the polypropylene-based aluminium-air battery," *Frontiers in Energy Research*, vol. 9, 2021. [Online]. Available: https://www.frontiersin.org/articles/10.3389/fenrg.2021.599846 18

[60] L.-L. Shen, G.-R. Zhang, M. Biesalski, and B. J. M. Etzold, "Paper-based microfluidic aluminum–air batteries: toward next-generation miniaturized power supply," *Lab Chip*, vol. 19, pp. 3438–3447, 2019. [Online]. Available: http://dx.doi.org/10.1039/C9LC00574A 18

[61] W. C. Tan, L. H. Saw, M. C. Yew, D. Sun, and W.-H. Chen, "High performance aluminum-air battery for sustainable power generation," *International Journal of Hydrogen Energy*, 2022. [Online]. Available: https://www.sciencedirect.com/science/article/pii/S0360319922055653 18, 19

[62] W.-W. Tian, J.-T. Ren, and Z.-Y. Yuan, "In-situ cobalt-nickel alloy catalyzed nitrogen-doped carbon nanotube arrays as superior freestanding air electrodes for flexible zinc-air and aluminum-air batteries," *Applied Catalysis B: Environmental*, vol. 317, p. 121764, 2022. [Online]. Available: https://www.sciencedirect.com/science/article/pii/S0926337322007056 18

[63] T. H. Pham, W.-H. Lee, J.-H. Byun, and J.-G. Kim, "Improving the performance of primary aluminum-air batteries through suppressing water activity by hydrogen bond-rich glycerol solvent additive," *Energy Storage Materials*, vol. 55, pp. 406–416, 2023. [Online]. Available: https://www.sciencedirect.com/science/article/pii/S2405829722006699 18

[64] S.-R. Choi, K.-M. Kim, and J.-G. Kim, "Organic corrosion inhibitor without discharge retardation of aluminum-air batteries," *Journal of Molecular Liquids*, vol. 365, p. 120104, 2022. [Online]. Available: https://www.sciencedirect.com/science/article/pii/S0167732222016439 18

[65] L. Fan and H. Lu, "The effect of grain size on aluminum anodes for al–air batteries in alkaline electrolytes," *Journal of Power Sources*, vol. 284, pp. 409–415, 2015. [Online]. Available: https://www.sciencedirect.com/science/article/pii/S0378775315004796 18

[66] R. Mori, "All solid state rechargeable aluminum–air battery with deep eutectic solvent based electrolyte and suppression of byproducts formation," *RSC Adv.*, vol. 9, pp. 22 220–22 226, 2019. [Online]. Available: http://dx.doi.org/10.1039/C9RA04567H 19

[67] R. Revel, T. Audichon, and S. Gonzalez, "Non-aqueous aluminium–air battery based on ionic liquid electrolyte," *Journal of Power Sources*, vol. 272, pp. 415–421, 2014. [Online]. Available: https://www.sciencedirect.com/science/article/pii/S0378775314013111 19

[68] R. Mckerracher, A. Holland, A. Cruden, and R. Wills, "Comparison of carbon materials as cathodes for the aluminium-ion battery," *Carbon*, vol. 144, pp. 333–341, 2019. [Online]. Available: https://www.sciencedirect.com/science/article/pii/S0008622318311527 19, 73

[69] C. Li, X. Zhang, and W. He, "Design and modification of cathode materials for high energy density aluminum-ion batteries: a review," *Journal of Materials Science: Materials in Electronics*, vol. 29, no. 16, pp. 14 353–14 370, Aug 2018. [Online]. Available: https://doi.org/10.1007/s10854-018-9478-1 19

[70] J. Smajic, S. Wee, F. R. F. Simoes, M. N. Hedhili, N. Wehbe, E. Abou-Hamad, and P. M. F. J. Costa, "Capacity retention analysis in aluminum-sulfur batteries," *ACS Applied Energy Materials*, vol. 3, no. 7, pp. 6805–6814, 2020. [Online]. Available: https://doi.org/10.1021/acsaem.0c00921 19

[71] A. Cruden., "Advanced materials for aluminium-ion battery," *Materials*, 2020. [Online]. Available: https://www.mdpi.com/journal/materials/special_issues/aluminium_ion_batteries 19

[72] S. K. Das, S. Mahapatra, and H. Lahan, "Aluminium-ion batteries: developments and challenges," *J. Mater. Chem. A*, vol. 5, pp. 6347–6367, 2017. [Online]. Available: http://dx.doi.org/10.1039/C7TA00228A 19

[73] G. H. Ruffo. (2021, May) New graphene aluminum-ion cell may ditch cooling systems. Date accessed: 20 February 2023. [Online]. Available: https://insideevs.com/news/508179/gmg-graphene-aluminum-ion-cell/ 19

[74] S. Xue, K. Li, Z. Lin, K. Zhang, J. Zheng, M. Zhang, and Z. Shen, "Rechargeable aluminum-ion battery based on interface energy storage in two-dimensional layered graphene/tio2 electrode," *Materials Today Sustainability*, vol. 20, p. 100213, 2022. [Online]. Available: https://www.sciencedirect.com/science/article/pii/S2589234722001051 20

[75] R. Li, C. Xu, X. Wu, J. Zhang, X. Yuan, F. Wang, Q. Yao, M. Sadeeq (Jie Tang) Balogun, Z. Lu, and J. Deng, "Aluminum-ion storage reversibility in a novel spinel al2/3li1/3mn2o4 cathode for aqueous rechargeable aluminum batteries," *Energy Storage Materials*, vol. 53, pp. 514–522, 2022. [Online]. Available: https://www.sciencedirect.com/science/article/pii/S2405829722005219 20

[76] A. S. Childress, P. Parajuli, J. Zhu, R. Podila, and A. M. Rao, "A raman spectroscopic study of graphene cathodes in high-performance aluminum ion batteries," *Nano Energy*, vol. 39, pp. 69–76, 2017. [Online]. Available: https://www.sciencedirect.com/science/article/pii/S2211285517303920 20

[77] K. Wang, K. Liu, C. Yang, Z. Chen, H. Zhang, Y. Wu, Y. Long, Y. Jin, X. He, M. Li, and H. Wu, "A high-performance intermediate-temperature aluminum-ion battery based on molten salt electrolyte," *Energy Storage Materials*, vol. 48, pp. 356–365, 2022. [Online]. Available: https://www.sciencedirect.com/science/article/pii/S2405829722001672 20

[78] Y. Hu, B. Luo, D. Ye, X. Zhu, M. Lyu, and L. Wang, "An innovative freeze-dried reduced graphene oxide supported sns2 cathode active material for aluminum-ion batteries," *Advanced Materials*, vol. 29, no. 48, p. 1606132, 2017. [Online]. Available: https://onlinelibrary.wiley.com/doi/abs/10.1002/adma.201606132 20

[79] "Gmg's battery update: Significant battery performance, cell and graphene production improvements: Graphene manufacturing group: Gmg," 2022, Date accessed: 25 January 2023. [Online]. Available: https://graphenemg.com/gmg-battery-performance-graphene-production/ 20

[80] Bu-808: How to prolong lithium-based batteries. Date accessed: 26 February 2023. [Online]. Available: https://batteryuniversity.com/article/bu-808-how-to-prolong-lithium-based-batteries 20

[81] M. S. Koroma, D. Costa, M. Philippot, G. Cardellini, M. S. Hosen, T. Coosemans, and M. Messagie, "Life cycle assessment of battery electric vehicles: Implications of future electricity mix and different battery end-of-life management," *Science of The Total Environment*, vol. 831, p. 154859, 2022. [Online]. Available: https://www.sciencedirect.com/science/article/pii/S0048969722019520 20

[82] H. Chen, H. Xu, S. Wang, T. Huang, J. Xi, S. Cai, F. Guo, Z. Xu, W. Gao, and C. Gao, "Ultrafast all-climate aluminum-graphene battery with quarter-million

cycle life," *Science Advances*, vol. 3, no. 12, p. eaao7233, 2017. [Online]. Available: https://www.science.org/doi/abs/10.1126/sciadv.aao7233 20

[83] N. Li, Y. Yao, T. Lv, Z. Chen, Y. Yang, S. Cao, and T. Chen, "High-performance wire-shaped aluminum ion batteries based on continuous graphene fiber cathodes," *Journal of Power Sources*, vol. 488, p. 229460, 2021. [Online]. Available: https://www.sciencedirect.com/science/article/pii/S0378775321000124 20

[84] M.-C. Lin, M. Gong, B. Lu, Y. Wu, D.-Y. Wang, M. Guan, M. Angell, C. Chen, J. Yang, B.-J. Hwang, and H. Dai, "An ultrafast rechargeable aluminium-ion battery," *Nature*, vol. 520, no. 7547, pp. 324–328, Apr 2015. [Online]. Available: https://doi.org/10.1038/nature14340 20

[85] K. Karuppasamy, J. Theerthagiri, D. Vikraman, C.-J. Yim, S. Hussain, R. Sharma, T. Maiyalagan, J. Qin, and H.-S. Kim, "Ionic liquid-based electrolytes for energy storage devices: A brief review on their limits and applications," *Polymers*, vol. 12, no. 4, 2020. [Online]. Available: https://www.mdpi.com/2073-4360/12/4/918 20

[86] E. Jónsson, "Ionic liquids as electrolytes for energy storage applications – a modelling perspective," *Energy Storage Materials*, vol. 25, pp. 827–835, 2020. [Online]. Available: https://www.sciencedirect.com/science/article/pii/S2405829719309511 20, 21

[87] J. Peters, D. Buchholz, S. Passerini, and M. Weil, "Life cycle assessment of sodium-ion batteries," *Energy Environ. Sci.*, vol. 9, pp. 1744–1751, 2016. [Online]. Available: http://dx.doi.org/10.1039/C6EE00640J 22

[88] C. Delmas, "Sodium and sodium-ion batteries: 50 years of research," *Advanced Energy Materials*, vol. 8, no. 17, p. 1703137, 2018. [Online]. Available: https://onlinelibrary.wiley.com/doi/abs/10.1002/aenm.201703137 22

[89] J.-Y. Hwang, S.-T. Myung, and Y.-K. Sun, "Sodium-ion batteries: present and future," *Chem. Soc. Rev.*, vol. 46, pp. 3529–3614, 2017. [Online]. Available: http://dx.doi.org/10.1039/C6CS00776G 22

[90] M. Bianchini, P. Xiao, Y. Wang, and G. Ceder, "Additional sodium insertion into polyanionic cathodes for higher-energy na-ion batteries," *Advanced Energy Materials*, vol. 7, no. 18, p. 1700514, 2017. [Online]. Available: https://onlinelibrary.wiley.com/doi/abs/10.1002/aenm.201700514 22

[91] C. Fang, Y. Huang, W. Zhang, J. Han, Z. Deng, Y. Cao, and H. Yang, "Routes to high energy cathodes of sodium-ion batteries," *Advanced Energy Materials*, vol. 6, no. 5, p. 1501727, 2016. [Online]. Available: https://onlinelibrary.wiley.com/doi/abs/10.1002/aenm.201501727 22

[92] F. Klein, B. Jache, A. Bhide, and P. Adelhelm, “Conversion reactions for sodium-ion batteries,” *Phys. Chem. Chem. Phys.*, vol. 15, pp. 15 876–15 887, 2013. [Online]. Available: http://dx.doi.org/10.1039/C3CP52125G 22

[93] M. Kumar, A. K. Padhan, D. Mandal, and T. C. Nagaiah, “An elemental sulfur/cos2-ionic liquid based anode for high-performance aqueous sodium-ion batteries,” *Energy Storage Materials*, vol. 45, pp. 1052–1061, 2022. [Online]. Available: https://www.sciencedirect.com/science/article/pii/S2405829721005043 23

[94] M. Kumar and T. C. Nagaiah, “High energy density aqueous rechargeable sodium-ion/sulfur batteries in ‘water in salt” electrolyte,” *Energy Storage Materials*, vol. 49, pp. 390–400, 2022. [Online]. Available: https://www.sciencedirect.com/science/article/pii/S2405829722001994 23

[95] B. Wang, X. Miao, H. Dong, X. Ma, J. Wu, Y. Cheng, H. Geng, and C. C. Li, “In situconstruction of active interfaces towards improved high-rate performance of cose2,” *Journal of Materials Chemistry A*, vol. 9, no. 25, p. 14582 – 14592, 2021. [Online]. Available: https://www.scopus.com/inward/record.uri?eid=2-s2.0-85108882866&doi=10.1039%2fd1ta03280a&partnerID=40&md5=10a8c7187a22292c34dc3ca335593759 23

[96] X. Wei, H. Yuan, H. Wang, R. Jiang, J. Lan, Y. Yu, and X. Yang, “The metal–organic framework mediated synthesis of bell string-like hollow zns–c nanofibers to enhance sodium storage performance,” *Mater. Chem. Front.*, vol. 5, pp. 4712–4724, 2021. [Online]. Available: http://dx.doi.org/10.1039/D1QM00423A 23

[97] C. C. Li, B. Wang, D. Chen, L.-Y. Gan, Y. Feng, Y. Zhang, Y. Yang, H. Geng, X. Rui, and Y. Yu, “Topotactic transformation synthesis of 2d ultrathin ges2 nanosheets toward high-rate and high-energy-density sodium-ion half/full batteries,” *ACS Nano*, vol. 14, no. 1, pp. 531–540, 2020, pMID: 31846288. [Online]. Available: https://doi.org/10.1021/acsnano.9b06855 23

[98] C. Wang, L. Sheng, M. Jiang, X. Lin, Q. Wang, M. Guo, G. Wang, X. Zhou, X. Zhang, J. Shi, and L. Jiang, “Flexible snse2/n-doped porous carbon-fiber film as anode for high-energy-density and stable sodium-ion batteries,” *Journal of Power Sources*, vol. 555, p. 232405, 2023. [Online]. Available: https://www.sciencedirect.com/science/article/pii/S0378775322013829 23

[99] L. E. Asp and E. S. Greenhalgh, “Chapter 20 - multifunctional structural battery and supercapacitor composites,” in *Multifunctionality of Polymer Composites*, K. Friedrich and U. Breuer, Eds. Oxford: William Andrew Publishing, 2015, pp. 619–661. [Online]. Available: https://www.sciencedirect.com/science/article/pii/B9780323264341000209 24

[100] P. Ladpli, R. Nardari, F. Kopsaftopoulos, and F.-K. Chang, "Multifunctional energy storage composite structures with embedded lithium-ion batteries," *Journal of Power Sources*, vol. 414, pp. 517–529, 2019. [Online]. Available: https://www.sciencedirect.com/science/article/pii/S0378775318314022 xxiii, 25, 58, 59, 60, 61, 66

[101] Y. Fu, Y. Chen, X. Yu, and L. Zhou, "Fiber metal laminated structural batteries with multifunctional solid polymer electrolytes," *Composites Science and Technology*, vol. 230, 11 2022. 25, 53, 54, 55, 66

[102] J. Galos, A. A. Khatibi, and A. P. Mouritz, "Vibration and acoustic properties of composites with embedded lithium-ion polymer batteries," *Composite Structures*, vol. 220, pp. 677–686, 2019. [Online]. Available: https://www.sciencedirect.com/science/article/pii/S0263822319305173 25

[103] J. Galos, A. Best, and A. Mouritz, "Multifunctional sandwich composites containing embedded lithium-ion polymer batteries under bending loads," *Materials & Design*, vol. 185, p. 108228, 2020. [Online]. Available: https://www.sciencedirect.com/science/article/pii/S0264127519306665 25, 56, 57, 58, 66

[104] J. P. Thomas and M. A. Qidwai, "Mechanical design and performance of composite multifunctional materials," *Acta Materialia*, vol. 52, no. 8, pp. 2155–2164, 2004. [Online]. Available: https://www.sciencedirect.com/science/article/pii/S1359645404000205 xxiii, 25, 55, 56, 66

[105] Y. Zhang, J. Ma, A. K. Singh, L. Cao, J. Seo, C. D. Rahn, C. E. Bakis, and M. A. Hickner, "Multifunctional structural lithium-ion battery for electric vehicles," *Journal of Intelligent Material Systems and Structures*, vol. 28, no. 12, pp. 1603–1613, 2017. [Online]. Available: https://doi.org/10.1177/1045389X16679021 25, 61, 62, 63, 66

[106] A. S. Hollinger, D. R. McAnallen, M. T. Brockett, S. C. DeLaney, J. Ma, and C. D. Rahn, "Cylindrical lithium-ion structural batteries for drones," *International Journal of Energy Research*, vol. 44, no. 1, pp. 560–566, 2020. [Online]. Available: https://onlinelibrary.wiley.com/doi/abs/10.1002/er.4937 xxiii, 25, 63, 64, 66

[107] X. Liu, H. Li, J. Wang, Q. Han, and C. Liu, "Achieving mechanically sturdy properties and high energy density for zn-ion structural batteries based on carbon-fiber-reinforced composites," *Composites Science and Technology*, vol. 218, 2 2022. 25, 42, 43, 44, 65, 66

[108] K. Moyer, C. Meng, B. Marshall, O. Assal, J. Eaves, D. Perez, R. Karkkainen, L. Roberson, and C. L. Pint, "Carbon fiber reinforced structural lithium-ion bat-

tery composite: Multifunctional power integration for cubesats," *Energy Storage Materials*, vol. 24, pp. 676–681, 1 2020. 25, 33, 35, 36, 66

[109] L. E. Asp, K. Bouton, D. Carlstedt, S. Duan, R. Harnden, W. Johannisson, M. Johansen, M. K. G. Johansson, G. Lindbergh, F. Liu, K. Peuvot, L. M. Schneider, J. Xu, and D. Zenkert, "A structural battery and its multifunctional performance," *Advanced Energy and Sustainability Research*, vol. 2, p. 2000093, 3 2021. 25, 35, 37, 38, 66

[110] K. Moyer, N. A. Boucherbil, M. Zohair, J. Eaves-Rathert, and C. L. Pint, "Polymer reinforced carbon fiber interfaces for high energy density structural lithium-ion batteries," *Sustainable Energy and Fuels*, vol. 4, pp. 2661–2668, 6 2020. 25, 34, 36, 66

[111] P. Liu, E. Sherman, and A. Jacobsen, "Design and fabrication of multifunctional structural batteries," *Journal of Power Sources*, vol. 189, no. 1, pp. 646–650, 2009, selected Papers presented at the 14th INTERNATIONAL MEETING ON LITHIUM BATTERIES (IMLB-2008). [Online]. Available: https://www.sciencedirect.com/science/article/pii/S0378775308018405 25, 39, 66

[112] E. L. Wong, D. M. Baechle, K. Xu, R. H. Carter, J. F. Snyder, and E. D. Wetzel, "Design and processing of structural composite batteries a reprint from the proceedings of society for the advancement of materiel and process engineering (sampe) 2007 symposium and exhibition," 2007. 25, 32, 66

[113] T. Carlson, *Multifunctional composite materials : design, manufacture and experimental characterisation*. Luleå University of Technology, 2013. 25, 40, 66

[114] F. Danzi, P. P. Camanho, and M. H. Braga, "An all-solid-state coaxial structural battery using sodium-based electrolyte," *Molecules*, vol. 26, no. 17, 2021. [Online]. Available: https://www.mdpi.com/1420-3049/26/17/5226 25, 51, 52, 66

[115] W. Huang, P. Wang, X. Liao, Y. Chen, J. Borovilas, T. Jin, A. Li, Q. Cheng, Y. Zhang, H. Zhai, A. Chitu, Z. Shan, and Y. Yang, "Mechanically-robust structural lithium-sulfur battery with high energy density," *Energy Storage Materials*, vol. 33, pp. 416–422, 2020. [Online]. Available: https://www.sciencedirect.com/science/article/pii/S2405829720303123 25, 40, 41, 42, 66, 83

[116] A. Chen, X. Guo, S. Yang, G. Liang, Q. Li, Z. Chen, Z. Huang, Q. Yang, C. Han, and C. Zhi, "Human joint-inspired structural design for a bendable/foldable/stretchable/twistable battery: achieving multiple deformabilities," *Energy Environ. Sci.*, vol. 14, pp. 3599–3608, 2021. [Online]. Available: http://dx.doi.org/10.1039/D1EE00480H 25, 45, 46, 66

[117] T. Jin, Y. Ma, Z. Xiong, X. Fan, Y. Luo, Z. Hui, X. Chen, and Y. Yang, "Bioinspired, tree-root-like interfacial designs for structural batteries with

enhanced mechanical properties," *Advanced Energy Materials*, vol. 11, no. 25, p. 2100997, 2021. [Online]. Available: https://onlinelibrary.wiley.com/doi/abs/10.1002/aenm.202100997 25, 45, 47, 66

[118] M. Wang, A. Emre, S. Tung, A. Gerber, D. Wang, Y. Huang, V. Cecen, and N. A. Kotov, "Biomimetic solid-state zn2+ electrolyte for corrugated structural batteries," *ACS Nano*, vol. 13, no. 2, pp. 1107–1115, 2019. [Online]. Available: https://doi.org/10.1021/acsnano.8b05068 25, 48, 49, 66

[119] C. Meng, N. Muralidharan, E. Teblum, K. E. Moyer, G. D. Nessim, and C. L. Pint, "Multifunctional structural ultrabattery composite," *Nano Letters*, vol. 18, no. 12, pp. 7761–7768, 2018, pMID: 30422660. [Online]. Available: https://doi.org/10.1021/acs.nanolett.8b03510 25, 49, 50, 66

[120] B. J. Hopkins, J. W. Long, D. R. Rolison, and J. F. Parker, "High-performance structural batteries," *Joule*, vol. 4, no. 11, pp. 2240–2243, 2020. [Online]. Available: https://www.sciencedirect.com/science/article/pii/S2542435120303457 26, 27

[121] M. H. Kjell, E. Jacques, D. Zenkert, M. Behm, and G. Lindbergh, "Pan-based carbon fiber negative electrodes for structural lithium-ion batteries," *Journal of The Electrochemical Society*, vol. 158, no. 12, p. A1455, nov 2011. [Online]. Available: https://dx.doi.org/10.1149/2.053112jes 26

[122] N. Ihrner, W. Johannisson, F. Sieland, D. Zenkert, and M. Johansson, "Structural lithium ion battery electrolytes via reaction induced phase-separation," *J. Mater. Chem. A*, vol. 5, pp. 25 652–25 659, 2017. [Online]. Available: http://dx.doi.org/10.1039/C7TA04684G 26

[123] R. Steinegger, "Fuel economy for aircraft operation as a function of weight and distance," ZHAW Zürcher Hochschule für Angewandte Wissenschaften, Winterthur, Tech. Rep., dec 2017. [Online]. Available: https://digitalcollection.zhaw.ch/handle/11475/1896 28

[124] J. P. Thomas and M. A. Qidwai, "The design and application of multifunctional structure-battery materials systems," *JOM*, vol. 57, no. 3, pp. 18–24, Mar 2005. [Online]. Available: https://doi.org/10.1007/s11837-005-0228-5 31, 32

[125] L. E. Asp and E. S. Greenhalgh, "Structural power composites," *Composites Science and Technology*, vol. 101, pp. 41–61, 2014. [Online]. Available: https://www.sciencedirect.com/science/article/pii/S0266353814002218 40, 45

[126] E. Jacques, M. H. Kjell, D. Zenkert, and G. Lindbergh, "The effect of lithium-intercalation on the mechanical properties of carbon fibres," *Carbon*, vol. 68, pp. 725–733, 2014. [Online]. Available: https://www.sciencedirect.com/science/article/pii/S0008622313011214 44

[127] J. Snyder, E. Gienger, and E. Wetzel, “Performance metrics for structural composites with electrochemical multifunctionality,” *Journal of Composite Materials*, vol. 49, no. 15, pp. 1835–1848, 2015. [Online]. Available: https://doi.org/10.1177/0021998314568167 44

[128] Seara.com. (2022) Inegi helps make reusing lithium for battery manufacturing easier. Date accessed: 16 August 2023. [Online]. Available: https://www.inegi.pt/en/news/inegi-helps-make-reusing-lithium-for-battery-manufacturing-easier/ 67

[129] J. Zhu, I. Mathews, D. Ren, W. Li, D. Cogswell, B. Xing, T. Sedlatschek, S. N. R. Kantareddy, M. Yi, T. Gao, Y. Xia, Q. Zhou, T. Wierzbicki, and M. Z. Bazant, “End-of-life or second-life options for retired electric vehicle batteries,” *Cell Reports Physical Science*, vol. 2, no. 8, p. 100537, 2021. [Online]. Available: https://www.sciencedirect.com/science/article/pii/S2666386421002484 67

[130] S. Ou, “Estimate long-term impact on battery degradation by considering electric vehicle real-world end-use factors,” *Journal of Power Sources*, vol. 573, p. 233133, 2023. [Online]. Available: https://www.sciencedirect.com/science/article/pii/S0378775323005086 67

[131] M. Zackrisson, C. Jönsson, W. Johannisson, K. Fransson, S. Posner, D. Zenkert, and G. Lindbergh, “Prospective life cycle assessment of a structural battery,” *Sustainability*, vol. 11, no. 20, 2019. [Online]. Available: https://www.mdpi.com/2071-1050/11/20/5679 68, 69

[132] D. L. Chandler, “Extending the life of low-cost, compact, lightweight batteries.” [Online]. Available: https://news.mit.edu/2018/metal-air-batteries-extending-life-1108 71

[133] K. L. Ng, M. Malik, E. Buch, T. Glossmann, A. Hintennach, and G. Azimi, “A low-cost rechargeable aluminum/natural graphite battery utilizing urea-based ionic liquid analog,” *Electrochimica Acta*, vol. 327, p. 135031, 2019. [Online]. Available: https://www.sciencedirect.com/science/article/pii/S0013468619319024 73

[134] F. Jach, M. Wassner, M. Bamberg, E. Brendler, G. Frisch, U. Wunderwald, and J. Friedrich, “A low-cost al-graphite battery with urea and acetamide-based electrolytes,” *ChemElectroChem*, vol. 8, no. 11, pp. 1988–1992, 2021. [Online]. Available: https://chemistry-europe.onlinelibrary.wiley.com/doi/abs/10.1002/celc.202100183 73

[135] M. Malik, K. L. Ng, and G. Azimi, “Physicochemical characterization of alcl3-urea ionic liquid analogs: Speciation, conductivity, and electrochemical stability,” *Electrochimica Acta*, vol. 354, p. 136708, 2020. [Online]. Available: https://www.sciencedirect.com/science/article/pii/S0013468620311014 73

[136] Z. Raheem, “Standard test methods for flexural properties of unreinforced and reinforced plastics and electrical insulating materials 1,” 01 2019. 80

[137] D. Gadakh, P. Dashora, and G. Wadhankar, “A review paper on graphene coated fibres,” *Graphene*, vol. 08, pp. 53–74, 2019. 83

[138] S. K. Das, “Graphene: A cathode material of choice for aluminum-ion batteries,” *Angewandte Chemie International Edition*, vol. 57, no. 51, pp. 16 606–16 617, 2018. [Online]. Available: https://onlinelibrary.wiley.com/doi/abs/10.1002/anie.201802595 87

[139] L. Su, L. Liu, B. Liu, J. Meng, and X. Yan, “Revealing the impact of oxygen dissolved in electrolytes on aqueous zinc-ion batteries,” *iScience*, vol. 23, no. 4, p. 100995, 2020. [Online]. Available: https://www.sciencedirect.com/science/article/pii/S2589004220301796 88

Appendix A

Appendix

A.1 Supplementary Figures

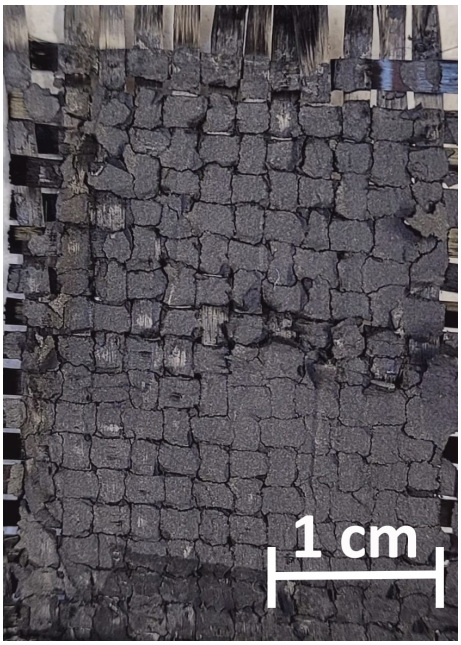

Figure A.1: Zoom out view of the graphene coated carbon fiber after the tensile test.

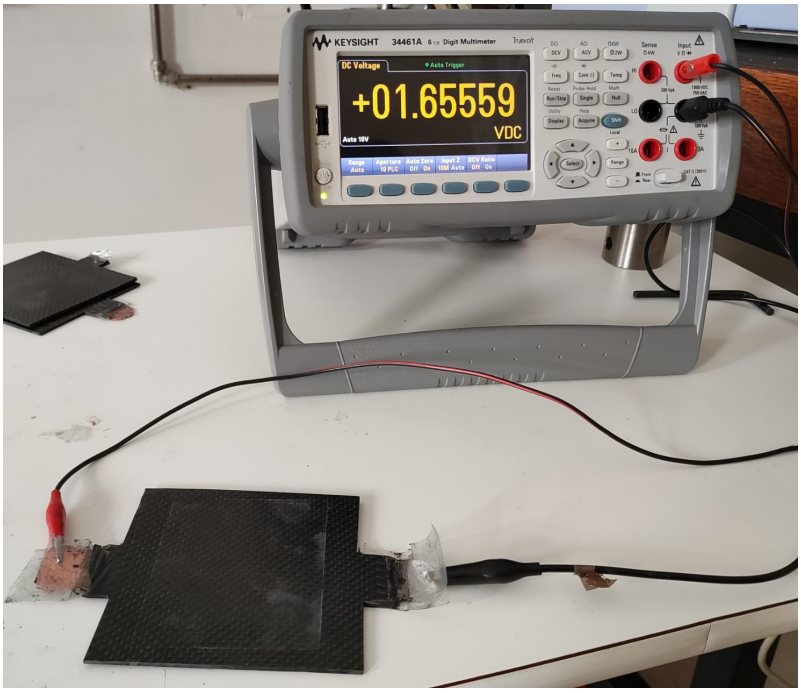

Figure A.2: Highest measured voltage on the aluminum-ion structural battery (1.66 V).